THESIS

Development of a 300-m Fabry-Perot cavity with automatic alignment

Kuniharu Tochikubo

May 1999

Contents

Chapter 1

Introduction

Gravitational wave was predicted by Einstein in 1916 [1]. The existence was proved by the observation of rotation period of the binary pulsar PSR1913+16 in 1989 [2]. However the proof of the existence is indirect. Therefore gravitational wave detectors have been developed aiming at direct detection.

Recently, large scale interferometers for the detection of the gravitational waves are being built by several projects; LIGO[3], VIRGO[4], GEO[5], and TAMA[6]. These interferometers are based on the Michelson interferometer to detect the difference in the Michelson arm lengths resulting from the effect of the gravitational waves. The mirrors of these interferometers are suspended by wires as pendulums for seismic isolation in the observation band of the detector (typically between several ten and several hundred Hz). In many cases, each of the Michelson arms consists of a long baseline Fabry-Perot (FP) cavity to obtain a large optical path length. Though the suspensions provide good vibration isolation above several ten Hz, the mirrors are driven by the seismic motion at the resonant frequency of the suspensions (typically 1 Hz or smaller) with an amplitude of a few μm, which is much larger than the width of the resonance of the cavities. Therefore the FP cavity has to be controlled to meet the exacting resonant condition stably over the operation period. Moreover, all of the mirrors have to be kept perpendicular to the laser beam to maintain the maximum sensitivity of the interferometer. The misalignment of the mirrors to the laser beam affects the sensitivity of the detector more seriously in the longer baseline interferometers[8]. For example, the misalignment angle of the mirrors to the input laser beam must be kept smaller than 5×10^{-7} rad in the TAMA300 detector[9]. However, there has been no experiments on the length and alignment control of a large scale suspended FP cavity with a baseline on the order of or larger than 100 m.

In pursuit of the construction of the TAMA300 gravitational wave detector, we have demonstrated the alignment and the length control of one of the arm cavities with a 300m baseline. With an automatic alignment control system, the cavity was kept locked to its resonance very stably over 5 days. Experimental results as well as some discussions will be

described in this thesis.

The TAMA300 detector[6] is a Fabry-Perot-Michelson (FPM) type interferometer with power-recycling, which is now under construction in the campus of National Astronomical Observatory (NAO), Mitaka, Tokyo. The detector aims to detect the wave with an amplitude as small as $3 \times 10^{-21} / \sqrt{\mathrm{Hz}}$ with its 300-m arms. As described above, the requirement for the alignment of the mirror angle is 5×10^{-7}rad.

Since the control systems for the length and the alignment should not introduce any additional noise into the interferometer, it is important to optimize the control systems to fit the environment of the site where the interferometer is located: The servo should be strong enough to compensate the large mirror motions in the low frequency range, while the bandwidth of the servo should be as narrow as possible to avoid making any excess noise in the measurement band. The seismic vibration, the temperature variation, the drift of the isolation stacks, and the drift of the ground itself can be thought as environmental parameters that are to be compensated. Thus, for a realistic design of the servo systems, it is essential to know these environmental parameters as accurate as possible. On the other hand, since these parameters have very small amplitudes in general, it is not easy to measure them, especially angular parameters, using independent sensors like accelerometers.

Therefore, at the first stage of the installation of the optics for TAMA300, one of the arm cavities was operated as a 300-m suspended Fabry-Perot cavity to measure the environmental inputs. Another objective of this one-arm experiment was to test the alignment sensing technique, to demonstrate the alignment control of such a long cavity, and to examine how the alignment control help the stable long-term operation of the interferometer.

About alignment control, several technique are proposed [10][11][12]. From them, Wave Front Sensing(WFS) technique which is proposed by H.Ward[13][14] is employed in the TAMA project. We review this technique in the chapter4. Then, the experimental set up and results are given in chapter5. In this chapter, we show our success of the length and alignment control of the 300m Fabry-Perot cavity. Since we obtained the stable operation of the cavity with alignment control, we could measure some properties of the cavity. The result is shown in Chapter6.

Chapter 2

Gravitational Waves

General relativity represents gravity as a curvature of space and time which is produced by mass. The theory predicts that accelerating mass can produce propagating waves of space-time curvature, known as gravitational waves. A wave solution can be deduced from the linearized Einstein's field equation, in analogous fashion to an electromagnetic wave solution deduced from electromagnetic field equation. In this chapter, at first, we review the derivation of the wave solution. Then we describe the effect of gravitational wave and how to detect them. Lastly, the sources of the gravitational waves are reviewed.

2.1 Gravitational Waves

According to the General Theory of Relativity, the metric tensor$g_{\mu\nu}$ satisfies Einstein's field equation [15] [16].

$$R_{\mu\nu} - \frac{1}{2}Rg_{\mu\nu} = \frac{8\pi G}{c^4}T_{\mu\nu}, \tag{2.1}$$

where G, c, and $T_{\mu\nu}$ are the gravitational constant, the speed of light, and the energy-momentum tensor, respectively and R(scalar tensor), $R_{\mu\nu}$(Ricci tensor) are defined using the following relations [1].

$$R \equiv g^{\mu\nu}R_{\mu\nu} \tag{2.2}$$

$$R_{\mu\nu} \equiv R^{\alpha}_{\mu\alpha\nu} \tag{2.3}$$

[1] In this chapter, superscripted or subscripted Greek symbols denote coordinate numbers from 0 to 3.

$$R^{\alpha}_{\beta\mu\nu} = \Gamma^{\alpha}_{\beta\nu,\mu} - \Gamma^{\alpha}_{\beta\mu,\nu} + \Gamma^{\alpha}_{\sigma\mu}\Gamma^{\sigma}_{\beta\nu} - \Gamma^{\alpha}_{\sigma\nu}\Gamma^{\sigma}_{\beta\mu} \quad \text{(Riemann tensor)} \tag{2.4}$$

$$\Gamma^{\gamma}_{\beta\mu} = \frac{1}{2}g^{\alpha\gamma}(g_{\alpha\beta,\mu} + g_{\alpha\mu,\beta} - g_{\beta\mu,\alpha}) \quad \text{(Christoffel symbol).} \tag{2.5}$$

In vacuum($T_{\mu\nu} = 0$), eq2.1 is

$$R_{\mu\nu} - \frac{1}{2}Rg_{\mu\nu} = 0. \tag{2.6}$$

As the general theory of relativity includes the special theory of relativity, metric in flat space

$$\eta_{\mu\nu} = \begin{pmatrix} -1 & & & 0 \\ & 1 & & \\ & & 1 & \\ 0 & & & 1 \end{pmatrix} \tag{2.7}$$

is one of the solution of Eq.2.1. Now we consider the case that the metric deviates by only the small amount $|h_{\mu\nu}| \ll 1$ from the flat metric $\eta_{\mu\nu}$. Treating $h_{\mu\nu}$ as deviation of the Minkowski space, this metric can be applied Ricci tensor. Taking the first order of $h_{\mu\nu}$, we obtain

$$\frac{\partial}{\partial x^{\nu}}\left(\frac{\partial g^{\rho}_{\mu}}{\partial x^{\rho}}\right) + \frac{\partial}{\partial x^{\mu}}\left(\frac{\partial g^{\rho}_{\nu}}{\partial x^{\rho}}\right) - \Box h_{\mu\nu} - \frac{\partial^2}{\partial x^{\mu}\partial x^{\nu}}h^{\rho}_{\rho} = 0. \tag{2.8}$$

For $h_{\mu\nu}$, applying the Lorentz gauge condition

$$\frac{\partial}{\partial x^{\nu}}h^{\nu}_{\mu} - \frac{1}{2}\frac{\partial}{\partial x^{\mu}}h^{\rho}_{\rho} = 0 \tag{2.9}$$

and using the coordinate transformation

$$\bar{h}_{\mu\nu} = h_{\mu\nu} - \frac{1}{2}\eta_{\mu\nu}h \tag{2.10}$$

then, we obtain from Eq.2.8

$$\Box\bar{h}_{\mu\nu} = 0. \tag{2.11}$$

This is called linialized Einstein's field equation in vacuum. This is the wave equation in the Minkovski space-time and it indicates the existence of the deviation $h_{\mu\nu}$ propagating at the speed of light, which are called gravitational waves.

One of the solutions for the equation

$$\bar{h}_{\mu\nu} = A_{\mu\nu} \exp[jk_\rho x^\rho] \tag{2.12}$$

is given. Though, in order to satisfy the Lorenz gauge condition and wave equation,

$$A_{\mu\nu}k^\nu = 0 \tag{2.13}$$

$$k_\mu k^\mu = 0 \tag{2.14}$$

are needed, the coordinate condition remains option. By the TT gauge [2] transformations,

$$\bar{h}_{\mu 0} = 0 \tag{2.15}$$

$$\bar{h}^\mu_\mu = 0. \tag{2.16}$$

Then, under the proper coordinate condition, we can obtain

$$h_{\mu\nu} = \begin{pmatrix} 0 & 0 & 0 & 0 \\ 0 & h_+ & h_\times & 0 \\ 0 & h_\times & -h_+ & 0 \\ 0 & 0 & 0 & 0 \end{pmatrix}, \tag{2.17}$$

where $h_+, h_\times$ represent polarizations of gravitational waves.

2.2 Effect of Gravitational Waves

In this section, the effect of gravitational waves will be described. We consider the situation in which a particle initially in a wave-free region of space-time encounters a gravitational wave. Choosing a background Lorenz frame in which the particle is initially at rest and the TT gauge refereed to this frame. A free particle obeys the geodesic equation.

$$\frac{\mathrm{d}^2 x^\alpha}{\mathrm{d}\tau^2} + \Gamma^\alpha_{\mu\nu} \frac{\mathrm{d}x^\mu}{\mathrm{d}\tau} \frac{\mathrm{d}x^\nu}{\mathrm{d}\tau} = 0. \tag{2.18}$$

As the particle is initially at rest, Eq.2.18 is

$$\frac{\mathrm{d}^2 x^\alpha}{\mathrm{d}\tau^2} + c^2 \Gamma^\alpha_{00} = 0. \tag{2.19}$$

[2]Transverse Traceless gauge:under this gauge condition, as mentioned below, though the coordinates of the free point masses don't change, the speed of light change.

By applying the first order approximation of $h_{\mu\nu}$ and from Eq.2.5

$$\Gamma^{\alpha}_{00} = \frac{1}{2}\eta^{\alpha\beta}(\mathrm{h}_{\beta 0,0} + \mathrm{h}_{0\beta,0} - \mathrm{h}_{00,\beta}) \simeq 0. \tag{2.20}$$

Then from Eq.2.17, we see

$$\frac{\mathrm{d}^2 x^{\alpha}}{\mathrm{d}\tau^2} = 0. \tag{2.21}$$

Therefore the acceleration vanishes initially. This means the particle will still be at rest a moment later. In other words, gravitational waves do not change the position of a mass.

Then to get a better measure of the effect of the wave, we consider the case for the proper distance Δl between two nearby particles, one at the origin and another at $x = \varepsilon, y = z = 0$, both beginning at rest.

$$\begin{aligned} \Delta l &\equiv \int |\mathrm{d}s^2|^{\frac{1}{2}} = \int |g_{\alpha\beta}\mathrm{d}x^{\alpha}\mathrm{d}x^{\beta}|^{\frac{1}{2}} \\ &= \int_0^{\varepsilon} |g_{xx}|^{\frac{1}{2}}\mathrm{d}x \simeq |g_{xx}(x=0)|^{\frac{1}{2}}\varepsilon \\ &\simeq \left[1 + \frac{1}{2}h_{xx}(x=0)\right]\varepsilon. \end{aligned} \tag{2.22}$$

Eq. 2.22 shows that gravitational waves change the proper distance. Therefore by the measuring the proper distance, gravitational waves can be detected.

This will be discussed more generally. We assume that the two particles are separated by the infinitesimal vector ε^{α}, having positions x^{α} and $x^{\alpha} + \varepsilon^{\alpha}$ respectively. Then the time dependence of ε^{α} is given by the following equation, derived from the geodesic equation 2.18

$$\frac{\mathrm{d}^2}{\mathrm{d}\tau^2}\varepsilon^{\alpha} = R^{\alpha}_{\mu\nu\beta}\frac{\mathrm{d}x^{\mu}}{\mathrm{d}\tau}\frac{\mathrm{d}x^{\nu}}{\mathrm{d}\tau}\varepsilon^{\beta}. \tag{2.23}$$

Applying the first order approximation about $h_{\mu\nu}$, we can obtain the change of the proper distance $\delta\varepsilon^{\alpha}$ with the incident waves expressed as Eq.2.17

$$\begin{pmatrix} \delta\varepsilon^x \\ \delta\varepsilon^y \\ \delta\varepsilon^z \end{pmatrix} = \frac{1}{2}\begin{pmatrix} h_+ & h_\times & 0 \\ h_\times & -h_+ & 0 \\ 0 & 0 & 0 \end{pmatrix}\begin{pmatrix} \varepsilon^x \\ \varepsilon^y \\ \varepsilon^z \end{pmatrix}\exp[jk(-ct+z)]. \tag{2.24}$$

From this equation, we can understand the meaning of the polarizations, $+-$mode and $\times-$mode. Fig.2.1 shows the displacement of the free particles for the h_+ and $h_\times$ polarization with the incident waves along z-axis.

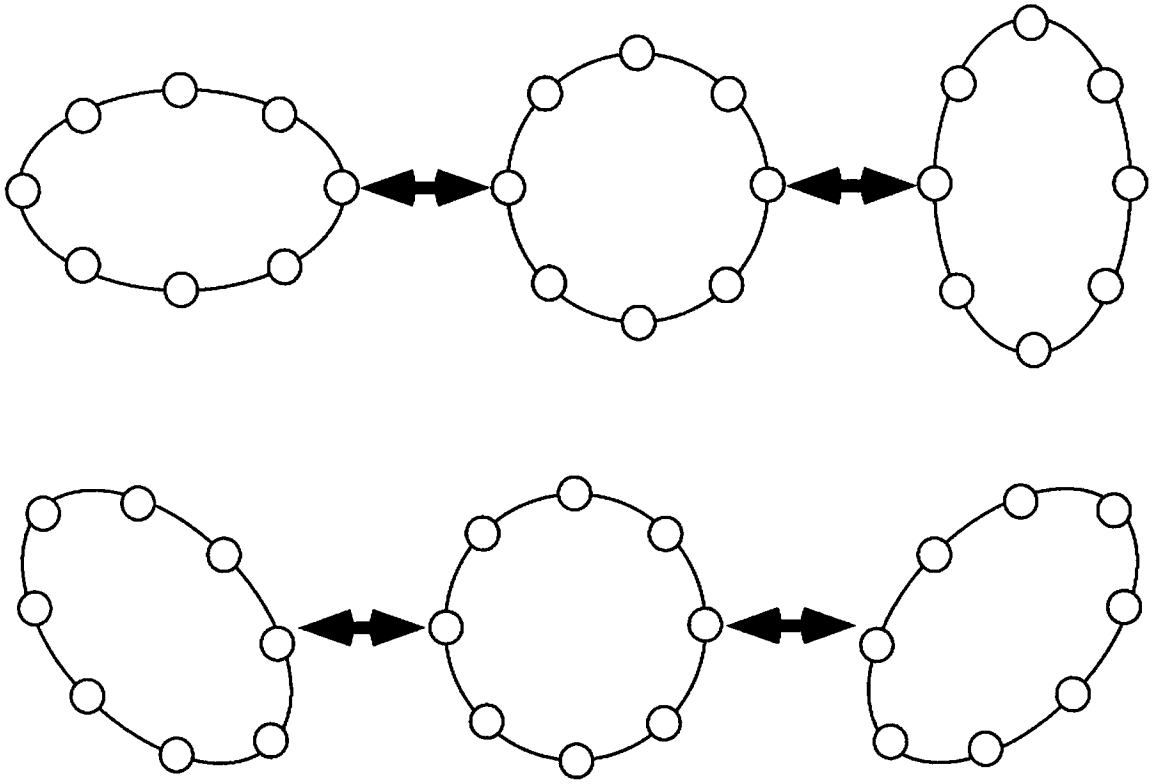

Figure 2.1: The effect of gravitational waves: displacement of the free particles for the h_+ and $h_\times$ polarization

2.3 Sources of Gravitational Waves

Gravitational wave was predicted by Einstein in 1916 [1]. The existence was proved by the observation of rotation period change of the binary pulsar PSR1913+16 in 1989 [2]. Because of the rotation of such massive binary star, gravitational waves are radiated and the binary star decrease their energy. The rotation period, which is influenced by the loss of the energy, is extended consequently. From the observation of the PSR1913+16, the influence of the gravitational wave is confirmed with an accuracy of less than 1%.

Now we aim at direct detection of gravitational waves. The sources of gravitational waves are pursued in astronomical phenomena of the massive stars since the effects of gravitational waves are feeble.

1. Supernovae

   In the case of supernova which bursts spherical symmetrically, the supernova cannot be detectable source of the gravitational wave because the phase information is cancelled out. However in the case that the core of the star is elliptical because of its rotation or in the situation that inside of the star is unstable physically, radiation of the gravitational wave with supernova is expected. Its maximum amplitude of the event in our galaxy(10kpc) is estimated $h \simeq 10^{-20}$. The event rate is also estimated once per one century in our galaxy, M31 and such large galaxies. Virgo cluster, which is 15Mpc away from our galaxy, is guessed, from its luminosity, that it corresponds to about a hundred large galaxies. Therefore in Virgo cluster, we expected the event rate is a few times per year.

   Waveform and amplitude of gravitational wave which generates with supernova depend on equation of state in the star and angular momentum. Measurements of such gravitational waves bring those information.

2. Coalescing Binary Neutronstars

   Up to the present, four binary neutronstars have been found. Coalescing such a binary neutronstar is expected to be a strong source of gravitational wave [3]. The maximum amplitude is estimated as

$$h \simeq 3.2 \times 10^{-22} \left(\frac{M_{charp}}{1.2M_{\odot}}\right)^{\frac{5}{6}} \left(\frac{f}{20\mathrm{Hz}}\right)^{-\frac{1}{6}} \left(\frac{r}{200\mathrm{Mpc}}\right)^{-1}, \tag{2.25}$$

   where M_{charp} is reduced mass of the binaries, which is called chirp mass. On the reasonable assumption, event rate is estimated a few event per year in the range of

[3] However the four binary neutronstars are thought that it takes 10^8 year to coalesce.

200Mpc [4]. At the time of coalescing, the gravitational wave is thought to show a waveform which is called chirp signal. From analysis of this signal, it is thought that the distance to the binary neutronstar can be estimated. This is the new measurement method of astronomical distance and it takes significance in the estimation of the Hubble constant.

3. Other sources

   (a) Pulsars

   The axial symmetric and stable system does not radiate the gravitational wave. However because of mountains or valleys on the pulsar, the pulsar is unaxial symmetric system and radiate the periodic gravitational wave. In such cases, the amplitude is estimated $h \simeq 10^{-25}$ for the pulsar in the Crab Nebula(2.3kpc).

   (b) Generation of Large Black Holes

   There are blackholes of which masses are $10^6 \sim 10^8 M_\odot$ in some galaxies. In a process of the formation, quasi characteristic vibration occur and it is thought to radiate gravitational wave. The amplitude is estimated as

$$h \simeq 10^{-15} \left(\frac{M}{10^8 M_\odot} \right) \left(\frac{r}{1\mathrm{Gpc}} \right)^{-1}. \tag{2.26}$$

   The frequency is thought to be mHz order. In such a low frequency region, it is hard to detect on the ground. Observations in space are expected in future.

2.4 Gravitational Wave Detectors

As discussed in the previous section, gravitational waves change the proper distance. By measuring the proper distance, gravitational waves are detected. However because of the very feeble change, the detectors require special instrument. The gravitational wave detectors are classified into two main groups. One group are called resonant gravitational wave detectors and the others are called interferometric gravitational wave detectors. In this section, we explain their principle of detection briefly and list the current status of them.

2.4.1 Current Status of Gravitational Wave Detectors

First, we mention about the resonant type. Though the shape of the detectors has variation, the detectors are utilized the vibration modes of the elastic body of the large mass.

[4] On the pessimistic assumption, event rate is estimated a few event per year in the range of 1Gpc. On the optimistic assumption, event rate is estimated a few event per year in the range of 20Mpc.

Group	Antenna	Transducer	Sensitivity (h)
CERN/Rome	Al 5056, 2.3ton, 2.6K	Capacitive+SQUID	7×10^{-19}
CERN	Al 5056, 2.3ton, 0.1K	Capacitive+SQUID	2×10^{-18}
LSU(USA)	Al 5056, 1.1ton, 4.2K	Inductive+SQUID	7×10^{-19}
Stanford(USA)	Al 6061, 4.8ton, 4.2K	Inductive+SQUID	10^{-18}
UWA(Australia)	Nb, 1.5ton, 5K	RF cavity	9×10^{-19}

Table 2.1: Resonant type gravitational wave detectors

Project	Baseline	Type	Observation from
TAMA(Japan)	300m	Fabry-Perot	1999
LIGO(USA)	4km(×2)	Fabry-Perot	2001
GEO(Germany & UK)	600m	Dual Recycling	2000
VIRGO(Italy & France)	3km	Fabry-Perot	2002

Table 2.2: Projects of the large scale interferometric gravitational wave detectors

The vibration mode is excited by the gravitational waves passed through the mass. Fig 2.2 shows the vibration mode of the bar type detector. As the detectors are manufactured with the high Q-values of the resonances, we can integrate continuing vibration of the bar even after the gravitational waves have passed away. The resonant detector is first reported by Weber in 1961[19]. After this, various experiments have been done. These are classified according to their shapes, transducers for signal detection, and the temperature. Table2.1 shows the current status of them.

The idea of interferometric gravitational wave detector is measuring the change of the proper distance between free masses, as Fig2.1 with interferometer. It is illustrated in Fig2.3. In Fig2.3, Michelson Interferometer is composed of mirrors by which is replaced free point masses on x and y axis, and beamsplitter which is arranged in the center of the circle. Encountering the gravitational waves of +-mode, The proper distances along x and y-axis change. The difference between the changes along the x-axis and y-axis is shown as the fringe at the anti-symmetric port. This is the brief explanation of the principle of gravitational wave detection with interferometer. However for detection, very long baseline interferometer and high power light source are required. Therefore several types of folded arms and recycling technique, which will be represent in the next chapter, have been proposed. Table2.2 shows the current status of large scale Interferometric gravitational wave detector.

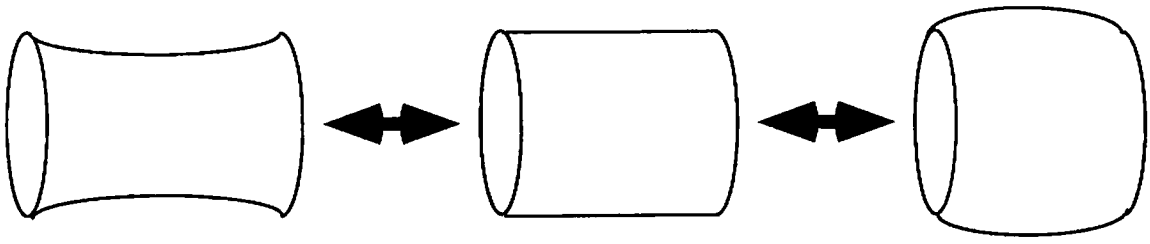

Figure 2.2: The vibration mode of the bar detector

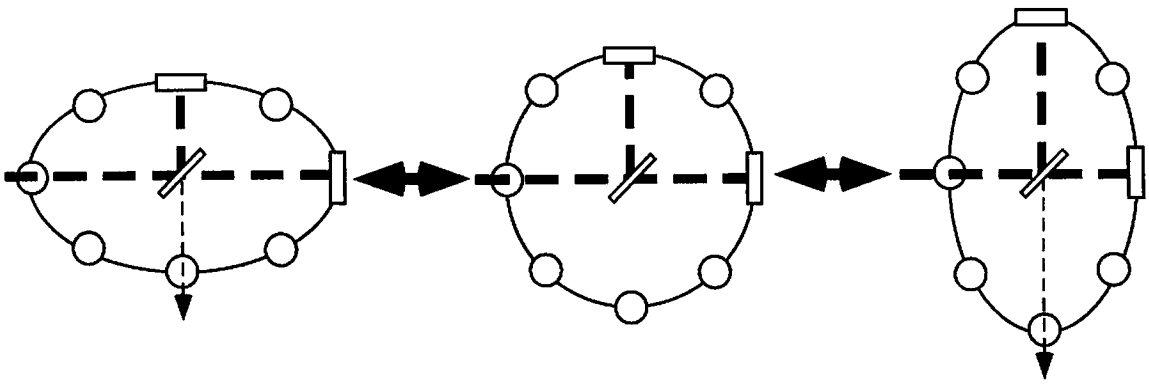

Figure 2.3: The idea of interferometric gravitational wave detector

Sensitivity	$h_{rms} = 3 \times 10^{-21}$ at 300Hz(Bandwidth 300Hz)
Type	Recycled Fabry-Perot-Michelson (RFPM)
Baseline	300m
Finesse of the arm cavities	520
Light source	Injection locked Nd:YAG laser
	Output power: 10W, Wave length:1064 nm
Power recycling	Gain: 10
	(Effective input power of the interferometer: 30W)
Vacuum duct	Diameter 40cm, Vacuum: 10^{-6} Pa

Table 2.3: The fundamental paramcter of TAMA interferometer

2.4.2 TAMA300

The 300-m arm-length interferometer is being built in the Mitaka campus of National Astronomical Observatory Japan[6]. Table2.3 shows the fundamental parameter of TAMA interferometer and Fig.2.4 shows the target sensitivity calculated from several noise sources. Power recycling technique is adopted in order to increase the light power illuminated to the 300-m Fabry-Perot cavity. Therefore main interferometer, which is called recycled Fabry-Perot-Michelson interferometer(RFPMI), is composed of five mirrors and a beamsplitter.

In Japan, the control schemes are developed with RFPMI prototype [21][26][27][28]. Applying these scheme, we are developing the control scheme of the 300-m RFPMI. This development has two main purposes. One is to start the operation before the other large scale interferometric gravitational wave detector project and to play a important role in a international network of the gravitational wave detection. The other is to develop the control technique for km-class interferometer in future.

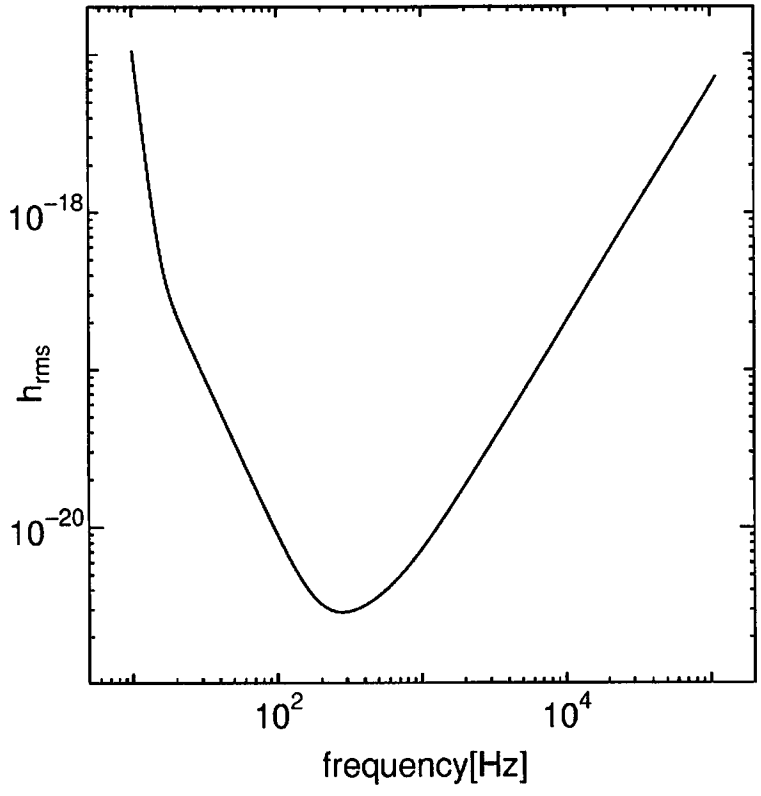

Figure 2.4: The target sensitivity of TAMA interferometer

Chapter 3

Interferometric Gravitational Wave Detectors

In this chapter, we discuss about the interferometric gravitational wave detector. At first, the effect of the gravitational wave to the Michelson interferometer is considered. Then, we explain the necessity of the folded arms from the length of the baseline for the best sensitivity. In the next section, we mention the properties of the Fabry-Perot cavity, one of the types of the folded arms.

3.1 Principle of Interferometric Gravitational Wave Detectors

We consider the principle of the gravitational wave detection with Michelson interferometer (Fig3.1). In this section, the gravitational wave introduced along z-axis is assumed. For simplicity, its components of polarization is assumed to be coincident with the optical axis of interferometer. We consider the case that the light is illuminated from origin to the mirror separated by l_1 and is reflected back the origin. The intervals Δt is derived. The propagation of the light obeys

$$\mathrm{d}s^2 = -c^2\mathrm{d}t^2 + \{1 + h(t)\}\mathrm{d}x^2 = 0. \tag{3.1}$$

From this equation,

$$\left\{1 - \frac{1}{2}h(t)\right\} c\mathrm{d}t \simeq \mathrm{d}x. \tag{3.2}$$

Integrating this equation, we obtain

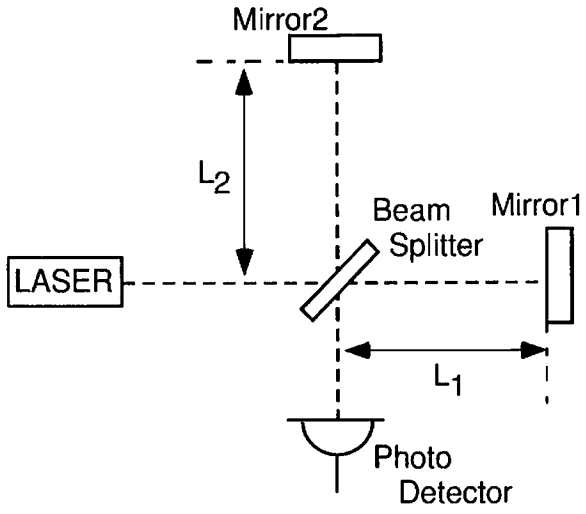

Figure 3.1: The Michelson Interferometer

$$\Delta t = \frac{2l_1}{c} + \frac{1}{2}\int_{t-\Delta t}^{t} h(t')\mathrm{d}t. \tag{3.3}$$

As the change of $h(t)$ is feeble enough, we can approximate as

$$\int_{t-\Delta t}^{t} h(t')\mathrm{d}t \simeq \int_{t-\frac{2l_1}{c}}^{t} h(t')\mathrm{d}t. \tag{3.4}$$

Then Eq.3.3 is

$$\Delta t = \frac{2l_1}{c} + \frac{1}{2}\int_{t-\frac{2l_1}{c}}^{t} h(t')\mathrm{d}t. \tag{3.5}$$

We put the angular frequency of light $\omega_0 = 2\pi c/\lambda$. Reflected light is propagated in phase by $\omega_0\Delta t$. In this phase propagation, effect of the gravitational wave is expressed as

$$\frac{\omega_0}{2}\int_{t-\frac{2l_1}{c}}^{t} h(t')\mathrm{d}t. \tag{3.6}$$

Up to here, we discuss the effect along x-axis. In the case of the effect along y-axis, we obtain the expression as

$$-\frac{\omega_0}{2}\int_{t-\frac{2l_2}{c}}^{t} h(t')\mathrm{d}t, \tag{3.7}$$

where l_2 is the arm length along y-axis. We put $l = l_1 \simeq l_2$. Then phase difference between the both arms is

$$\omega_0 \int_{t-\frac{2l}{c}}^{t} h(t')\mathrm{d}t'. \tag{3.8}$$

We can measure this phase difference as the fringes at the anti-symmetric port. This is the principle of the gravitational wave detection with the Michelson interferometer.

Then we carry out Fourier transform to $h(t)$

$$h(t) = \int_{-\infty}^{\infty} h(\omega)e^{j\omega t}\mathrm{d}\omega. \tag{3.9}$$

Therefore Eq.3.8 can be rewrited as

$$\omega_0 \int_{t-\frac{2l}{c}}^{t} \mathrm{d}t' \int_{-\infty}^{\infty} h(\omega)e^{j\omega t'}\mathrm{d}\omega. \tag{3.10}$$

From this equation, we can obtain

$$\int_{-\infty}^{\infty} \mathrm{d}\omega h(\omega)e^{j\omega t}\frac{\omega_0}{\omega}\sin\left(\frac{\omega l}{c}\right)e^{-j\frac{\omega l}{c}} \equiv \int_{-\infty}^{\infty} \mathrm{d}\omega h(\omega)e^{j\omega t}H_M(\omega). \tag{3.11}$$

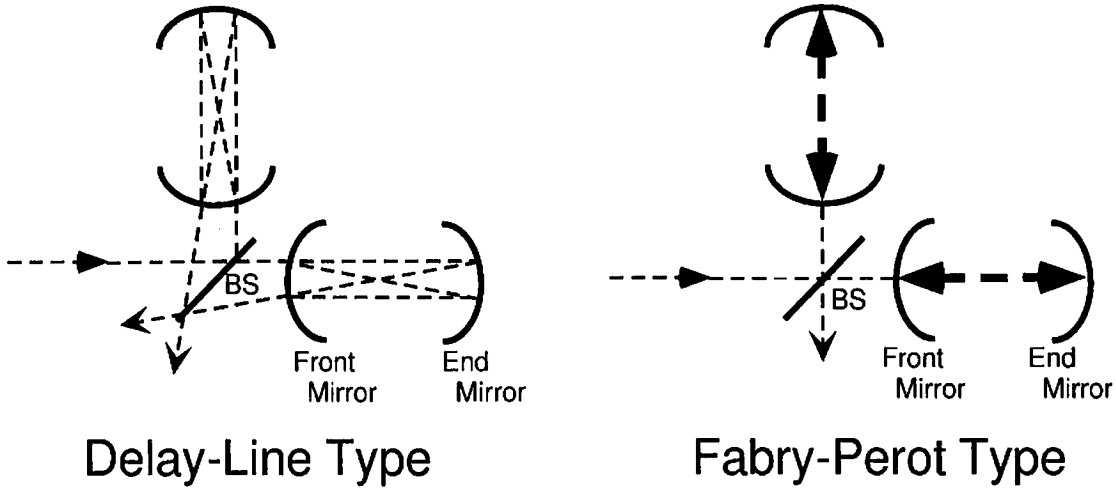

Figure 3.2: The delay line type and Fabry-Perot type interferometer

We can consider H_M as a response function of interferometer for gravitational wave. In the case that H_M is considered as a function of l, it reaches maximum value with $\omega l/c = \pi/2$. For example, the 75km baseline length is the best value for gravitational wave

at 1kHz. However the 75km baseline interferometer is unrealistic. Therefore folded arms are adopted. There are two types of folded arms. One is the delay line type and the other is Fabry-Perot type(Fig.3.2). In this thesis, we discuss about Fabry-Perot type.

3.2 Fabry-Perot cavity

In this section, we mention properties of Fabry-Perot cavity of which arms of TAMA interferometer are consisted.

3.2.1 Multiple Reflection

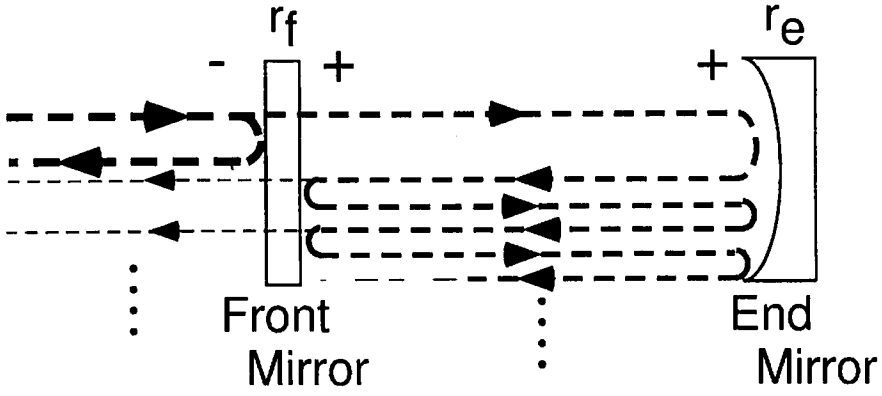

Figure 3.3: Fabry-Perot cavity

We consider two mirrors separated by l with amplitude reflectance r_f, r_e, transmittance t_f, t_e (Fig.3.3). The light at the frequency ω_0 is illuminated. Then input field is expressed as

$$E_{in} = E_0 e^{j\omega_0 t}. \tag{3.12}$$

While the fields of the reflected and transmitted light E_r and E_t are

$$E_r = E_{in} r_f + \sum_{n=0}^{\infty} E_{in}(-r_e) t_f^2 e^{-21\delta} (r_f r_e e^{-2j\delta})^n$$

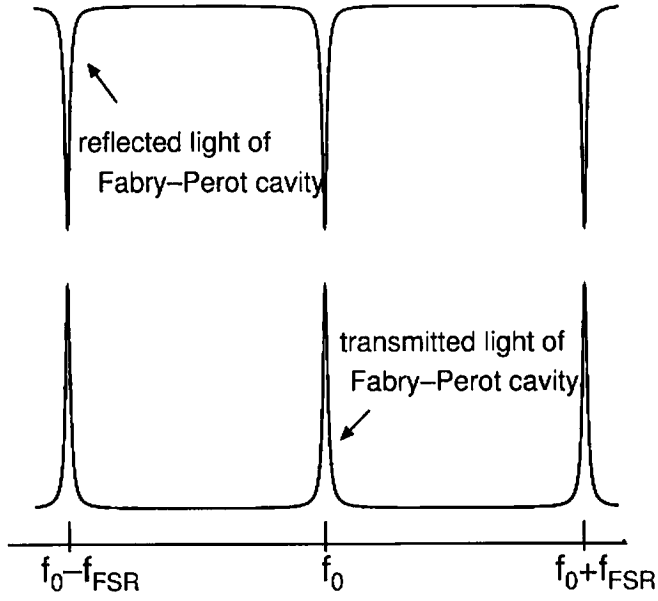

Figure 3.4: The reflectivity and transmittance of Fabry-Perot cavity

$$= \frac{r_f - r_e(1-p_f^2)e^{-2j\delta}}{1 - r_f r_e e^{-2j\delta}} E_{in} \tag{3.13}$$

$$E_t = \sum_{n=0}^{\infty} E_{in} t_f t_e e^{-j\delta} (r_f r_e e^{-2j\delta})^n$$

$$= \frac{t_f t_e e^{-j\delta}}{1 - r_f r_e e^{-2j\delta}} E_{in}, \tag{3.14}$$

where p_f is loss of the front mirror ($r_f^2 + t_f^2 + p_f^2 = 1$) and δ is phase difference while light propagates at a distance of the cavity length l and it is expressed as $\delta = \omega l/c$. We put the field intensity I_{in}, I_r, I_t corresponding to E_{in}, E_r, E_t. From Eq.3.12, 3.13 and 3.14

$$\frac{I_r}{I_i} = \left|\frac{E_r}{E_i}\right|^2$$

$$= \frac{(r_f - r_e(1-p_f^2))^2 + 4r_f r_e(1-p_f^2)\sin^2\delta}{(1 - r_f r_e)^2 + 4r_f r_e \sin^2\delta} \tag{3.15}$$

$$\frac{I_t}{I_i} = \frac{t_f^2 t_e^2}{(1 - r_f r_e)^2 + 4r_f r_e \sin^2\delta}. \tag{3.16}$$

We define finesse $\mathcal{F}$ as

$$\mathcal{F} \equiv \frac{\pi\sqrt{r_f r_e}}{1 - r_f r_e}. \tag{3.17}$$

Then we can rewrite Eq.3.16

$$\frac{I_t}{I_{in}} = \left(\frac{t_f t_e}{1 - r_f r_e}\right)^2 \frac{1}{1 + F\sin^2\delta}, \tag{3.18}$$

where F is defined as $F \equiv (2\mathcal{F}/\pi)^2$. when $r_f r_e \sim 1$, we can see from Eq.3.18 that it is periodic function, which has sharp peaks under the resonant condition, $\delta = \omega l/c = n\pi$. This fundamental period represented as

$$\nu_{\rm FSR} = \frac{\omega_{\rm FSR}}{2\pi} = \frac{c}{2l} \tag{3.19}$$

is called Free-Spectral-Range (FSR). Finesse $\mathcal{F}$ is also defined as the ratio of half width of the peak to FSR.

3.2.2 Response Function of Fabry-Perot Cavity

In this section, we represent the response function of Fabry-Perot cavity to gravitational wave and its property. We consider the situation that Fabry-Perot cavity shown in Fig.3.3 encounter with gravitational wave. We put that the input light is $e^{j\omega_0 t}$. Then the amplitude of the reflected light field, $E_{\rm r}$, is

$$\begin{aligned} E_{\rm r} &= r_f e^{j\omega_0 t} + t_f^2(-r_e)e^{j\omega_0 t_f} + t_f^2(-r_e)^2(-r_f)e^{j\omega_0 t_f} + \cdots \\ &= r_f e^{j\omega_0 t} + \frac{t_f^2}{-r_f}\sum_{n=1}^{\infty}(r_f r_e)^n e^{j\omega_0 t_n}, \end{aligned} \tag{3.20}$$

where t_n is expressed as

$$t_n = t - \frac{2nl}{c} - \frac{1}{2}\int_{t-\frac{2n}{c}l}^{t} h(t')dt'$$

from Eq.3.6. We assume that the effect of gravitational wave is very feeble. Therefore $e^{j\omega_0 t_n}$ is approximated as

$$e^{j\omega_0 t_n} \simeq e^{j\omega_0\left(t-\frac{2n}{c}l\right)}\left(1 - \frac{j\omega_0}{2}\int_{t-\frac{2n}{c}l}^{t} h(t')dt'\right)$$

Then E_r is

$$\simeq r_f e^{j\omega_0 t} - \frac{t_f^2}{r_f} e^{j\omega_0 t} \sum_{n=1}^{\infty} (r_f r_e)^n e^{-j\omega_0 \frac{2nl}{c}} + \frac{t_f^2}{r_f} e^{j\omega_0 t} \sum_{n=1}^{\infty} (r_f r_e)^n e^{-j\omega_0 \frac{2nl}{c}} \frac{j\omega_0}{2} \int_{t-\frac{2n}{c}l}^{t} h(t')dt', \quad (3.21)$$

Using Fourier transformation of $h(t)$

$$h(t) = \int_{-\infty}^{\infty} h(\omega) e^{j\omega t} d\omega$$

and

$$\begin{aligned} \Lambda(\omega_0) &= \frac{t_f^2}{r_f} \sum_{n=1}^{\infty} (r_f r_e)^n e^{-j\omega_0 \frac{2nl}{c}} \\ &= \frac{t_f^2 r_e e^{-j\omega_0 \frac{2l}{c}}}{1 - r_f r_e e^{-j\omega_0 \frac{2l}{c}}}. \end{aligned}$$

Then we can rewrite Eq.3.21 as

$$E_r = e^{j\omega_0 t} \left[r_f - \Lambda(\omega_0) + \frac{j\omega_0}{2} \int_{-\infty}^{\infty} d\omega \frac{h(\omega)}{j\omega} e^{j\omega t} \{\Lambda(\omega_0) - \Lambda(\omega_0 + \omega)\} \right]$$

. Under the resonant condition $e^{-j\omega_0 \frac{2l}{c}} = 1$

$$\begin{aligned} \Lambda(\omega_0) - \Lambda(\omega_0 + \omega) &= \frac{t_f^2 r_e}{1 - r_f r_e} - \frac{t_f^2 r_e e^{-j\omega \frac{2l}{c}}}{1 - r_f r_e e^{-j\omega \frac{2l}{c}}} \\ &= \frac{t_f^2 r_e}{(1 - r_f r_e)(1 - r_f r_e e^{-j\omega \frac{2l}{c}})} e^{-j\frac{\omega l}{c}} 2 \sin\left(\frac{\omega l}{c}\right). \end{aligned}$$

Therefore we obtain

$$\begin{aligned} E_r &= e^{j\omega_0 t} \left[\frac{r_f - r_e(r_f^2 + t_f^2)}{1 - r_f r_e} + j \int_{-\infty}^{\infty} d\omega \frac{\omega_0}{2\omega} h(\omega) e^{-j\omega t} \frac{t_f^2 r_e}{(1 - r_f r_e)(1 - r_f r_e e^{-j\omega \frac{2l}{c}})} e^{-j\frac{\omega l}{c}} 2 \sin\left(\frac{\omega l}{c}\right) \right] \\ &= e^{j\omega_0 t} \frac{r_f - r_e(r_f^2 + t_f^2)}{1 - r_f r_e} \left[1 + j \frac{t_f^2 r_e}{r_f - r_e(r_f^2 + t_f^2)} \int_{-\infty}^{\infty} d\omega h(\omega) e^{j\omega t} \frac{\omega_0}{\omega} \frac{1}{1 - r_f r_e e^{-j\frac{2\omega l}{c}}} \sin\left(\frac{\omega l}{c}\right) \right] \\ &= e^{j\omega_0 t} \frac{r_f - r_e(r_f^2 + t_f^2)}{1 - r_f r_e} [1 - j\Delta\Phi_{GR}], \end{aligned} \quad (3.22)$$

where $\Delta\Phi_{GR}$ is

$$\Delta\Phi_{GR} = \int_{-\infty}^{\infty} h(\omega) e^{j\omega t} H_{\rm FP}(\omega) d\omega$$

. $H_{\rm FP}(\omega)$ is called the response function of Fabry-Perot cavity and expressed as

$$\begin{aligned} H_{\rm FP}(\omega) &= \frac{t_f^2 r_e}{(t_f^2 + r_f^2) r_e - r_f} \frac{\omega_0}{\omega} e^{-j\frac{\omega l}{c}} \sin\left(\frac{\omega l}{c}\right) \frac{1}{1 - r_f r_e e^{-j\frac{2\omega l}{c}}} \\ &\equiv \alpha \frac{\omega_0}{\omega} e^{-j\frac{\omega l}{c}} \sin\left(\frac{\omega l}{c}\right) \frac{1}{1 - r_f r_e e^{-j\frac{2\omega l}{c}}}. \end{aligned} \tag{3.23}$$

Especially in the case that $\omega l/c \ll 1$, it is approximated as

$$|H_{\rm FP}(\omega)| \simeq \frac{\alpha}{2\sqrt{r_f r_e}} \frac{\omega_0}{\omega} \frac{\tau_s \omega}{\sqrt{1 + \tau_s^2 \omega^2}}, \tag{3.24}$$

where τ_s is called storage time and represented as

$$\tau_s \equiv \frac{2l\mathcal{F}}{\pi c}$$

.

From the expression of Eq.3.24, $H_{\rm FP}(\omega)$ behaves as Low Pass Filter and its cut-off frequency is

$$f_{\rm cut-off} = \frac{1}{2\pi\tau_s}. \tag{3.25}$$

Chapter 4

Wave Front Sensing Technique for Alignment Control

In this chapter, we explain the principle of the signal detection method for length control and alignment control of Fabry-Perot cavity. To begin with, we review that the field of Fabry-Perot cavity and laser light can be expanded in the terms of the Hermite Gaussian modes under proper approximation [17]. In the following section, Two types of the difference between the modes of the Fabry-Perot cavity and those of laser light, mismatching and misalignment, are expressed using Hermite Gaussian modes [10]. Next, we note the influence of the misalignment of the typical configuration of the Recycled Fabry-Perot-Michelson Interferometer.

In the next section, we explain the rf reflection locking technique. At first, Pound-Drever method [18], which is used for length control, is mentioned. Then we explained how Wave Front Sensing technique[13] can be detected misalignment signals.

4.1 Hermite Gaussian Modes

Though the properties of laser light propagating in free space is similar to plane waves, for example, the amplitude distribution of cross section is not uniform. We consider the expression of the field of laser light. It satisfies the wave equation for the scalar field $u(t, x, y, z)$

$$\nabla^2 u + k^2 u = 0, \tag{4.1}$$

where k is the wave number($k = 2\pi/\lambda$). This wave propagating along the z-axis is expressed as

$$u = \exp(j\omega_0 t)\psi(x, y, z)\exp(x, y, z), \tag{4.2}$$

where ψ is the function representing the difference from the plane wave. We assume that the field changes along the z-axis very slowly, therefore the terms of $\partial^2\psi/\partial z^2$ is neglected, which is called paraxial approximation. Then Eq 4.1 is rewrited.

$$\left[\left(\frac{\partial^2}{\partial x^2}+\frac{\partial^2}{\partial y^2}\right)-2jk\frac{\partial}{\partial z}\right]\psi=0. \tag{4.3}$$

Now the field, whose amplitude distribute in X-Y plane is Gaussian, is assumed the solution of this equation. We expressed the field as

$$\psi=\exp\left\{-j\left(P(z)+\frac{k}{2q(z)}(x^2+y^2)\right)\right\}. \tag{4.4}$$

This is applied to Eq.4.3, we obtain two differential equation,

$$\frac{d}{dz}P=-\frac{j}{q} \tag{4.5}$$

$$\frac{d}{dz}q=1. \tag{4.6}$$

Now we introduce the real parameter R, w instead of q.

$$\frac{1}{q}=\frac{1}{R}-j\frac{\lambda}{\pi w^2}. \tag{4.7}$$

Using these parameter, ψ is rewrited,

$$\psi=\exp\left\{-j\left(P(z)+\frac{k}{2R(z)}(x^2+y^2)\right)-\frac{x^2+y^2}{w^2}\right\}. \tag{4.8}$$

R indicates the curvature radius of phase front around the beam axis and w indicates the distance toward radius, which the amplitude drop $1/e^2$ compared to that on the z axis. Then we put that q_0 is q at $z=0$, q, which are separated by z, is

$$q=q_0+z. \tag{4.9}$$

We assumed that q is pure imaginary, the phase of ψ is constant, which is independent of x and y, in the plane at $z=0$. This means the phase front is plane ($R=\infty$). As the beamradius is minimum, we call this place beam waist. We put beam radius at the waist is w_0. Then q_0 is,

$$q=j\frac{\pi w_0^2}{\lambda}. \tag{4.10}$$

Using Eq.4.7, $w(z), R(z)$ can be expressed as

$$w^2(z) = w_0^2 \left[1 + \left(\frac{\lambda z}{\pi w_0^2}\right)^2\right] \tag{4.11}$$

$$R(z) = z \left[1 + \left(\frac{\pi w_0^2}{\lambda z}\right)^2\right]. \tag{4.12}$$

In the region of $z \gg \pi w_0^2/\lambda$,

$$w(z) \simeq \frac{\lambda z}{\pi w_0}. \tag{4.13}$$

We can see that $\lambda/\pi w_0$ indicates divergence angle of the beam at a far place and we put it α_0.

From Eq.4.5, we can obtain the expression of the $P(z)$.

$$P(z) = -j \ln \sqrt{1 + \left(\frac{\lambda z}{\pi w_0^2}\right)^2} - \arctan\left(\frac{\lambda z}{\pi w_0^2}\right). \tag{4.14}$$

We define

$$\eta(z) \equiv \arctan\left(\frac{\lambda z}{\pi w_0^2}\right) \tag{4.15}$$

and call Guoy Phase. It indicates that the phase difference between the Gaussian beam and the simple plane wave.

Up to here, the one of the solutions of paraxial approximated wave equation, fundamental Gaussian mode is discussed. Generally, we put

$$\psi = g\left(\frac{x}{w}\right) h\left(\frac{y}{w}\right) \exp\left\{-j\left(P(z) + \frac{k}{2q(z)}(x^2 + y^2)\right)\right\}. \tag{4.16}$$

Then the other modes (the higher order modes) with a rectangular geometry can be obtained. Applying this equation to the wave equation, we can see that $g \cdot h$ is expressed with Hermite polynomials H_m.

$$g \cdot h = H_m\left(\sqrt{2}\frac{x}{w}\right) H_l\left(\sqrt{2}\frac{y}{w}\right). \tag{4.17}$$

At this time, Guoy phase term become

$$(l + m + 1)\eta(z). \tag{4.18}$$

This means the existence of the phase difference between the different modes.

Finally, laser light propagating in free space along z-axis has the Hermite-Gaussian modes and the normalized expression is

$$U_{lm\rightarrow}(x,y,z) = U_l(x,z)U_m(y,z)\exp j\{-kz + (l+m+1)\eta(z)\} \tag{4.19}$$

$$U_l(x,z) \equiv \left(\frac{2}{\pi}\right)^{\frac{1}{4}} \left(\frac{1}{l!2^l}\right)^{\frac{1}{2}} H_l\left(\sqrt{2}\frac{x}{w(z)}\right) \exp\left[-\left(\frac{x}{w(z)}\right)^2 - j\frac{k}{2R(z)}x^2\right], \tag{4.20}$$

where

$$w(z) = w_0\sqrt{1+\left(\frac{z}{z_0}\right)^2} : \text{beam redius} \tag{4.21}$$

$$R(z) = \frac{z^2+z_0^2}{z} : \text{curvature radius of the wave front} \tag{4.22}$$

$$z_0 = \frac{kw_0^2}{2} : \left(k = \frac{2\pi}{\lambda}\right) \tag{4.23}$$

$$\eta(z) = \arctan\left(\frac{z}{z_0}\right) : \text{Guoy phase} \tag{4.24}$$

$$\alpha_0 = \frac{2}{kw_0} : \text{divergence angle of the beam} \tag{4.25}$$

$$H_l : \text{Hermite polynomials.} \tag{4.26}$$

We note the case of the beam propagating in the inverse direction along z-axis.

$$\begin{aligned} U_{lm\leftarrow}(x,y,z) &= U_{lm\rightarrow}(x,y,-z) \\ &= U_l(x,-z)U_m(y,-z)\exp j\{-k(-z) + (l+m+1)\eta(-z)\} \\ &= U^*_{lm\rightarrow}(x,y,z). \end{aligned} \tag{4.27}$$

4.2 Expression of Misalignment

The eigenmodes of a Fabry-Perot cavity is also approximated by the Gaussian modes. When the laser light introduce to the Fabry-Perot cavity, the mode of the input beam is made to match TEM_{00} mode of the Fabry-Perot cavity with lenses. In fact, it does not match completely. There are two kinds of parameters which represent the difference

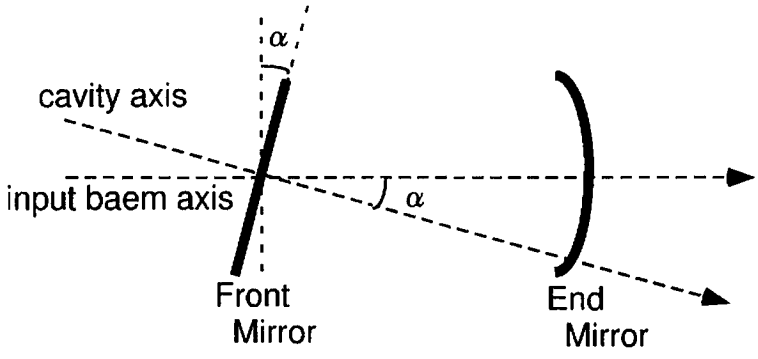

Figure 4.1: The misalignment of tilt

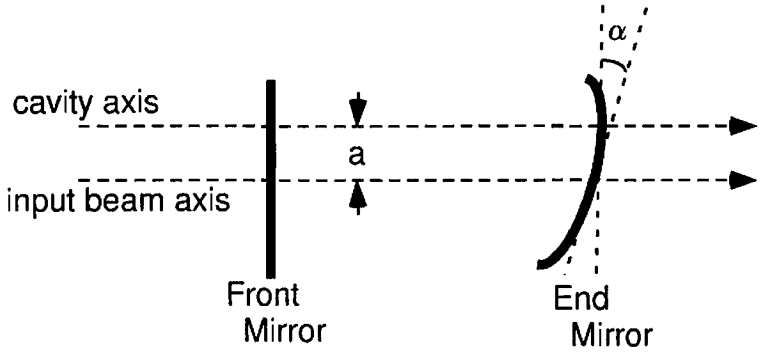

Figure 4.2: The misalignment of lateral shift

between the two modes: one is the difference of the waist position or size, i.e., the mismatching; the other is the difference in the axes of the two modes, i.e., the misalignment. In this chapter, we assume that the mismatching is negligible.

There are two types of the misalignment. One is the tilt of the axis(Fig. 4.1). The other is the lateral shift of the axis(Fig. 4.2). At first, when the input beam axis tilt against the cavity axis, we consider how the TEM_{00} mode of the laser is represented with modes of the cavity. In this case, the coordinate transformation is

$$\begin{pmatrix} x \\ z \end{pmatrix} = \begin{pmatrix} \cos(-\alpha) & -\sin(-\alpha) \\ \sin(-\alpha) & \cos(-\alpha) \end{pmatrix} \begin{pmatrix} x' \\ z' \end{pmatrix}. \tag{4.28}$$

When the relative tilt α is assumed that $\alpha/\alpha_0 \ll 1$, $U_{00}(x,y,z)$, the TEM_{00} mode of the input beam, can be expanded with the modes of the cavity at the $z' = 0$ [20].

$$\begin{aligned} U_{00}|_{z'=0} &= U_0(x'\cos\alpha, -x'\sin\alpha)U_0(y', -x'\sin\alpha)\exp j\{kx'\sin\alpha + \eta(-x'\sin\alpha)\} \\ &\simeq U_{00}(x',y',0) + j\alpha\left(\frac{1}{\alpha_0}U_{10}(x',y',0) + \frac{\sqrt{6}}{8}\alpha_0 U_{30}(x',y',0) + \frac{\sqrt{2}}{8}\alpha_0 U_{12}(x',y',0)\right). \end{aligned} \tag{4.29}$$

Usually $\alpha_0 \ll 1$, therefore

$$U_{00}|_{z'=0} \simeq U_{00}(x',y',0) + j\frac{\alpha}{\alpha_0}U_{10}(x',y',0). \tag{4.30}$$

In the case of the lateral shift of the axis, the coordinate transformation is

$$x = x' - a. \tag{4.31}$$

When the lateral shift is assumed that $a/w_0 \ll 1$, $U_{00}|_{z'=0}$ can be expanded in the same way of the tilt case.

$$\begin{aligned} U_{00}|_{z'=0} &= U_0(x'-a,0)U_0(y',0) \\ &\simeq U_{00}(x',y',0) + \frac{a}{w_0}U_{10}(x',y',0). \end{aligned} \tag{4.32}$$

Therefore we obtain the approximation of the field of the input beam as the superposition of the eigenmodes of the Fabry-Perot cavity. Though ,up to here, we discuss about $U_{00}|_{z'=0}$, Eq.4.30 and Eq.4.32 are guaranteed adequateness in the case that $z' \ll z_0$ [21].

4.3 Influence of the Misalignment

Influences of misalignments for TAMA type interferometer are mainly classified into those of three physical values as contrast, recycling gain and CMRR.

1. Contrast

   In TAMA interferometer, we employ the scheme which detect the signal of differential motion of the arms corresponding to the gravitational wave at the anti-symmetric port. Ultimately, the target sensitivity in the observation band is limited by shot noise. Shot noise is caused by the fluctuation of photon counting with photo detector and expressed as

   $$i_{shot} = \sqrt{2eI_D}, \tag{4.33}$$

   where e is an elementary charge and the units are $\mathrm{A}/\sqrt{\mathrm{Hz}}$. Considering the signal-to-noise ratio, we operate this interferometer to be dark at this port. The contrast C is one of parameters which show to what extent the deconstructive interference is realized and represents the performance of the interferometer.

   $$C = \frac{I_{max} - I_{min}}{I_{max} + I_{min}}, \tag{4.34}$$

   where $I_{max}(I_{min})$ is maximum(minimum) of the power at anti-symmetric port. Misalignments introduce asymmetry to both arms and increase light leaking out to anti-symmetric port. Assuming that we must keep the contrast larger than 99% for Fabry-Perot-Michelson with TAMA spec., the requirement of misalignment angle is[20]

   $$\alpha \sim 5 \times 10^{-7}[\mathrm{rad}]$$

2. Recycling Gain

   As mentioned above, power recycling technique is employed in TAMA project. It is realized by arranging a recycling mirror at symmetric port shown in Fig.4.3. Reflected light from the Fabry-Perot-Michelson interferometer is hit back with this mirror to the interferometer. In other words, regarding the Fabry-Perot-Michelson interferometer as a compound mirror, Fabry-Perot cavity, which is called recycling cavity, is consisted of the recycling mirror and the compound mirror (Fig.4.3). The ratio of the stored

energy in the recycling cavity to the input power represent the increase ratio of the power introduced to the Fabry-Perot-Michelson interferometer. We call this ratio recycling gain.

As mentioned above, the misalignment causes TEM_{00} of the input beam to couple to TEM_{10} of the cavity. Therefore it causes the loss of TEM_{00} of the cavity which affect the gravitational wave signal. Calculating the loss and assuming that we must keep the recycling gain larger than 90% of the best value, the requirement of misalignment angle is[20]

$$\alpha \sim 5 \times 10^{-7}[\text{rad}]$$

.

3. CMRR

As noises attributed to the light source, such as frequency noises and intensity noises, introduce in common with the both arms, its influence is reduced by the deconstructive interference. If the interferometer is symmetric completely, its contribution to signal is made to be zero. In fact, it is hard to realize such a situation. It is thought that the common mode reduction ratio (CMRR) is $10^{-2} \sim 10^{-3}$ with Fabry-Perot-Michelson interferometer[21]. As misalignments introduce asymmetry to both arms, the CMRR is affected. Comparing the attained frequency stability of laser source and the target sensitivity, we obtain required CMRR and the required misalignment is derived from it. We estimate that it is $\sim 10^{-7}$rad at the present time.

4.4 RF Reflection Locking Technique

In this experiment, as mentioned in the previous section, the two types of the feedback systems are employed. One is the length control system, which holds the resonant condition of the cavity. The other is the alignment control system, which adjust for misalignment. In the both cases, the signal detection schemes are needed and the RF(radio frequency) reflection locking techniques are adopted. Introducing the RF phase modulated light to the Fabry-Perot cavity, the signals are obtained in the reflected light from the cavity.

The amplitude of phase modulated light E_{in} is expressed as

$$\begin{aligned} E_{in} &= E_0 \exp\{j(\omega_0 t + m \sin \omega_m t)\} \\ &= E_0 \exp(j\omega_0 t) \sum_{n=-\infty}^{\infty} J_n(m) \exp(jn\omega_m t), \end{aligned} \tag{4.35}$$

where ω_0 is frequency of light, ω_m is frequency of modulation, J_n is the Bessel function and m is modulation depth. Now we assume $m << 1$, the expression is approximated

$$E_{in} \simeq E_0\{J_0(m)e^{j\omega_0 t} + J_1(e^{j(\omega_0+\omega_m)t} - e^{j(\omega_0-\omega_m)t})\} \quad (4.36)$$
$$= E_0\{J_0(m) + 2jJ_1(m)\sin\omega_m t\}e^{j\omega_0 t}. \quad (4.37)$$

From Eq.4.36, we can see that it consists of two kinds of terms. One is called carrier, which has the frequency of light. The other is called sideband whose frequency is shifted by the modulation frequency. As the modulation frequency is selected under the condition that the sidebands are anti-resonance when the carrier is resonance [1]. The phase changes at reflection are quite different between carrier and sidebands. Therefore, from the beat of them, we can obtain the information of the cavity resonance. By the Pound-Drever method, the information of the deviation of the cavity length or frequency from the resonance is obtained. By the wave front sensing, that of the mialignment is obtained. We explain these method concretely in sequence.

4.4.1 Pound-Drever Method

We consider the case that the misalignment is negligible. Therefore only TEM_{00} mode is considered. The reflected light from the cavity E_r is

$$E_r = E_0\{r_{c0}J_0(m)e^{j\omega_0 t} + J_1(m)(r_{c0+s}e^{j(\omega_0+\omega_m)t} - r_{c0-s}e^{j(\omega_0-\omega_m)t}\}U_{00}, \quad (4.38)$$

where r_{c0} is the reflectance for carrier and $r_{c0+s}(r_{c0-s})$ is that for upper(lower) sideband. As the modulation frequency is selected adequately, $r_{c0+s}(r_{c0-s}) \simeq 1$. r_{c0} is expressed as the Eq.3.13.

$$r_{c0} = \frac{r_f - r_e(1-p_f^2)e^{-2j\delta}}{1 - r_f r_e e^{-2j\delta}}. \quad (4.39)$$

If we assumed the deviation $\delta \ll 1$, r_{c0} is approximated as

$$\simeq \frac{r_f - r_e(1-p_f^2)}{1 - r_f r_e} + 2j\frac{r_e t_f^2}{(1 - r_f r_e)^2}\delta, \quad (4.40)$$

Therefore the reflected light is

$$E_r \simeq E_0\left\{\left(\frac{r_f - r_e(1-p_f^2)}{1 - r_f r_e} + 2j\frac{r_e t_f^2}{(1 - r_f r_e)^2}\delta\right)J_0(m)e^{j\omega_0 t} + 2jJ_1(m)e^{j\omega_0 t}\sin\omega_m t\right\}U_{00}. \quad (4.41)$$

[1] In other words, it is selected larger than the width of the resonance.

In the intensity of the reflected light $I_r(=\int |E_r|^2 ds)$, the term of the $\sin\omega_m t$ is

$$8J_0(m)J_1(m)\frac{r_e t_f^2}{(1-r_f r_e)^2}\delta \sin\omega_m t. \tag{4.42}$$

Therefore the demodulated signal, which can be obtained by multiplying $\sin\omega_m t$, is proportional to the deviation from the resonance δ. This is the principle of the signal detection by the use of the Pound Drever method.

We note that the deviation δ is the variable of the deviation of the cavity length Δl and that of the laser frequency $\Delta\omega$. That is,

$$\delta = \frac{\Delta\omega l_0 + \omega_0 \Delta l}{c}. \tag{4.43}$$

Δl and $\Delta\omega$ cannot be distinguished.

4.4.2 Wave Front Sensing Technique

In this section, we discuss about the signal detection of misalignment. Here, we consider the case that the optic axis of the cavity is tilted or shifted relative to the input beam because of the misalignment of the mirror (Fig 4.5).

The input beam is assumed to comprise pure TEM_{00} mode U_{00} along the beam axis. (Because of necessary to distinguish between the modes of input light and reflected light, we represent the modes of the input light $U_{00\rightarrow}$; one of the reflect light $U_{00\leftarrow}$.) In order to detect the signal for the alignment control, the input beam is also modulated in phase. Therefore the amplitude field E_{in} is expressed as Eq.4.37. The cavity is also assumed to has a set of the eigenmodes U'_{lm} along the cavity axis. For the waist size of the beam w_0 and the divergence angle of the beam α_0, the relative tilt α and the relative lateral shift a are assumed that $\alpha/\alpha_0 \ll 1$, $a/w_0 \ll 1$. As mentioned in the section 4.2, under this assumption, we obtain the approximation of the field of the input beam as the superposition of the eigenmodes of the FP cavity.

$$U_{00\rightarrow} \simeq U'_{00\rightarrow} + \left(-\frac{a}{w_0} + j\frac{\alpha}{\alpha_0}\right) U'_{10\rightarrow}. \tag{4.44}$$

The expression of the reflected light from the misaligned FP cavity is a product of the reflectance of the FP cavity on the lm mode r_{lm}. For the carrier component, it is

$$J_0(m)\left[r_{00}U'_{00\leftarrow} + r_{10}\left(-\frac{a}{w_0} + j\frac{\alpha}{\alpha_0}\right) U'_{10\leftarrow}\right] E_0 e^{j\omega_0 t}. \tag{4.45}$$

In consideration of the phase propagation to the photodetector, the approximation of the reflected light is obtained as the superposition of the modes along the input beam axis.

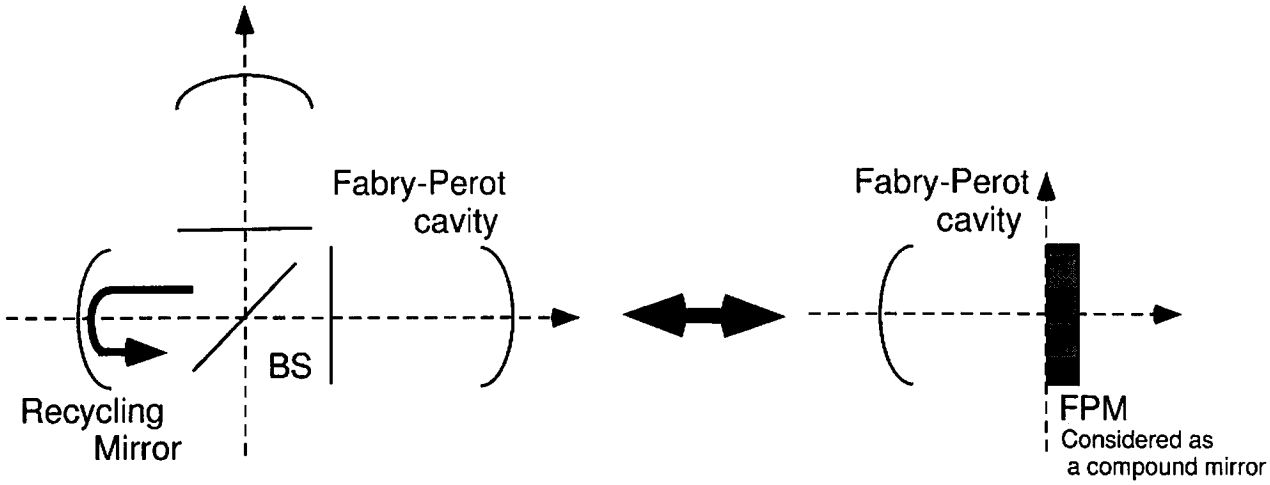

Figure 4.3: The power recycling configuration

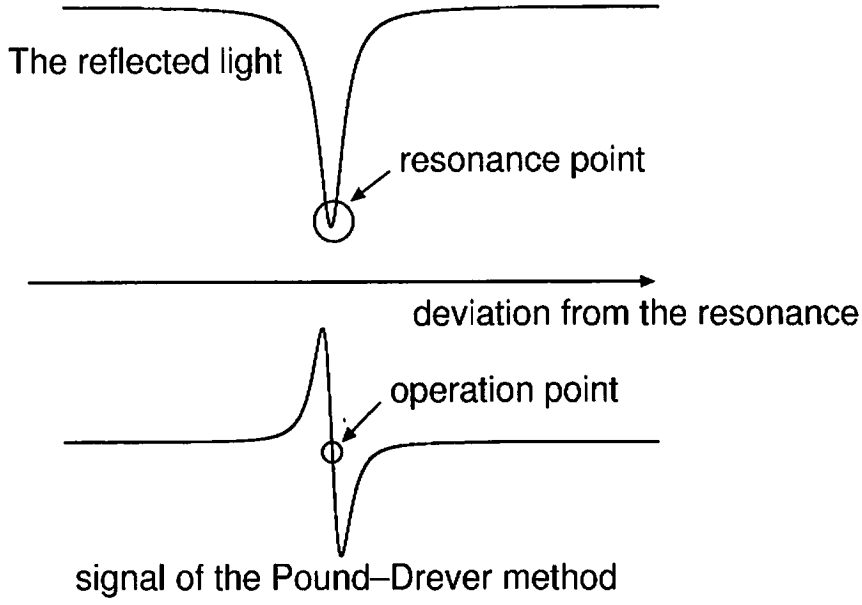

Figure 4.4: The typical signal of the Pound Drever method and the shape of the reflected light

$$\simeq J_0(m)\left[r_{00}U_{00\leftarrow}+\left\{(r_{00}-r_{10})\frac{a}{w_0}+j(r_{00}+r_{10})\frac{\alpha}{\alpha_0}\right\}e^{j\eta_l}U_{10\leftarrow}\right]E_0e^{j(\omega_0 t-k_0 l+\eta_l)}, \quad (4.46)$$

where k is the wave number of the light, l is the distance between the mode waist to the photo detector and η_l is the Guoy phase shift corresponding to the distance l.

Next, we consider the case for the sidebands. Usually, the FP cavity is anti-resonance for the sidebands when the carrier locking is realized by using the Pound-Drever method. Therefore the reflectance of the FP cavity for the sidebands take the same value r_s. The expression of the reflected light for the sideband components are

$$J_1(m)\left[r_sU_{00\leftarrow}+2jr_s\frac{\alpha}{\alpha_0}e^{j\eta_l}U_{10\leftarrow}\right]E_0e^{j\{(\omega_0\pm\omega_m)t-(k_0\pm k_m)l+\eta_l\}}, \quad (4.47)$$

where ω_m is the modulation frequency, k_m is the wave number of the modulation.

In the total reflecting field composed of the carrier and the sidebands, we can obtain the demodulated signal which is propotional to the misalignment as the multiplication of U_{00} and U_{10}. Because of the profile of $U_{00}U_{10}$, the segmented detector is required to detect this signal. Usually the quadrant photodetector is utilized since we can extract the horizontal tilt motion(yaw) and the vertical one (pitch). The extracted signal of misalignment information is proportional to

$$\propto J_0(m)J_1(m)E_0^2(r_{00}-r_{10})r_s\left\{\frac{a}{w_0}\sin\eta_l-\frac{\alpha}{\alpha_0}\cos\eta_l\right\}. \quad (4.48)$$

In the event that the FP cavity consists of the flat front mirror and the concave end mirror with the curvature radius R , the front mirror tilt α_F causes the lateral shift $(R-d)\alpha_F/w_0$ and the tilt α_F/α_0 where d is the cavity length as shown in Fig.4.6.

From the Eq. 4.48, the WFS signal corresponds to the front mirror tilt is

$$\propto\left(\frac{R-d}{w_0}\sin\eta_l-\frac{1}{\alpha_0}\cos\eta_l\right)\alpha_F. \quad (4.49)$$

The end mirror tilt α_E causes the lateral shift $R\alpha_E/w_0$. therefore the WFS signal is

$$\propto\left(\frac{R}{w_0}\sin\eta_l\right)\alpha_E. \quad (4.50)$$

Therefore we can separate the signal of the each mirror tilt from the other by adjusting the Guoy phase shift in the quadrant photodetector position. The relation between the signal of Wave Front Sensing and the Guoy phase in TAMA case is shown in Fig.4.7.

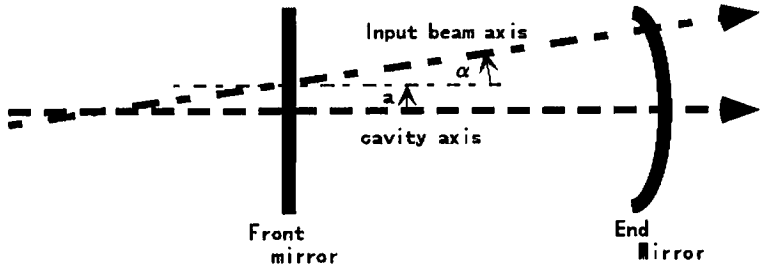

Figure 4.5: the misaligned cavity

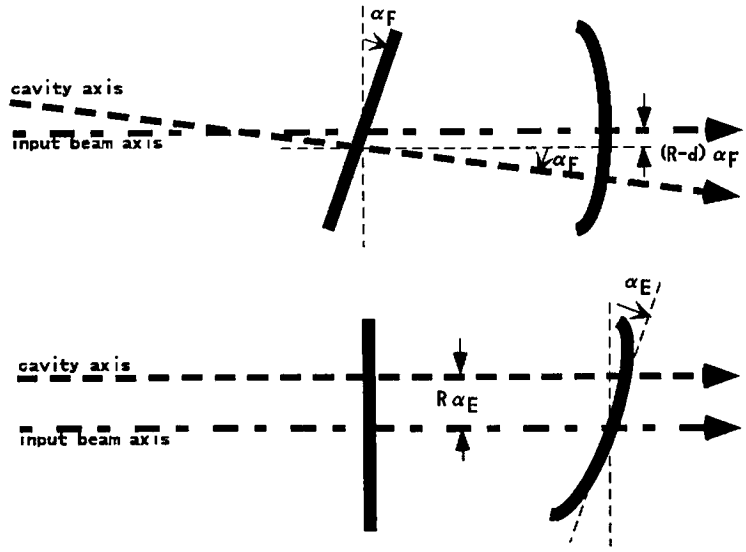

Figure 4.6: The actual misalignment corresponding to tilt of each mirror

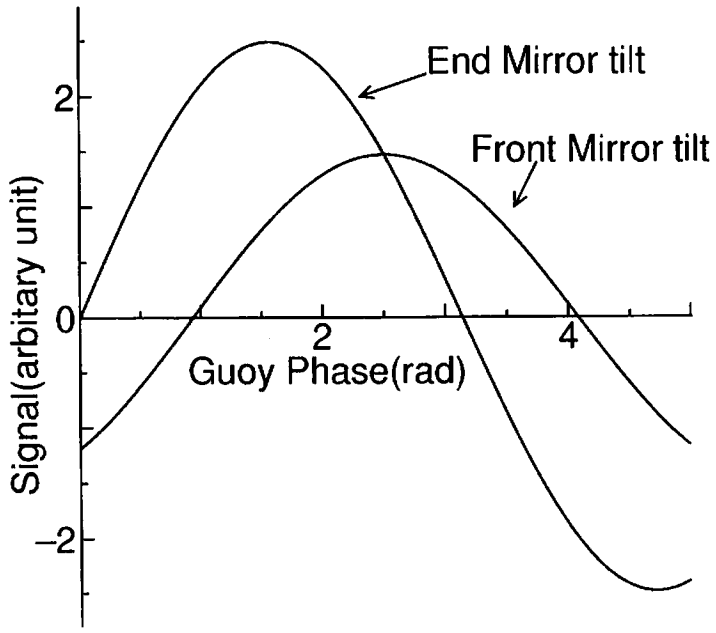

Figure 4.7: The relation between the signal of Wave Front Sensing and the Guoy phase

Chapter 5

Development of the TAMA300 interferometer

5.1 TAMA300

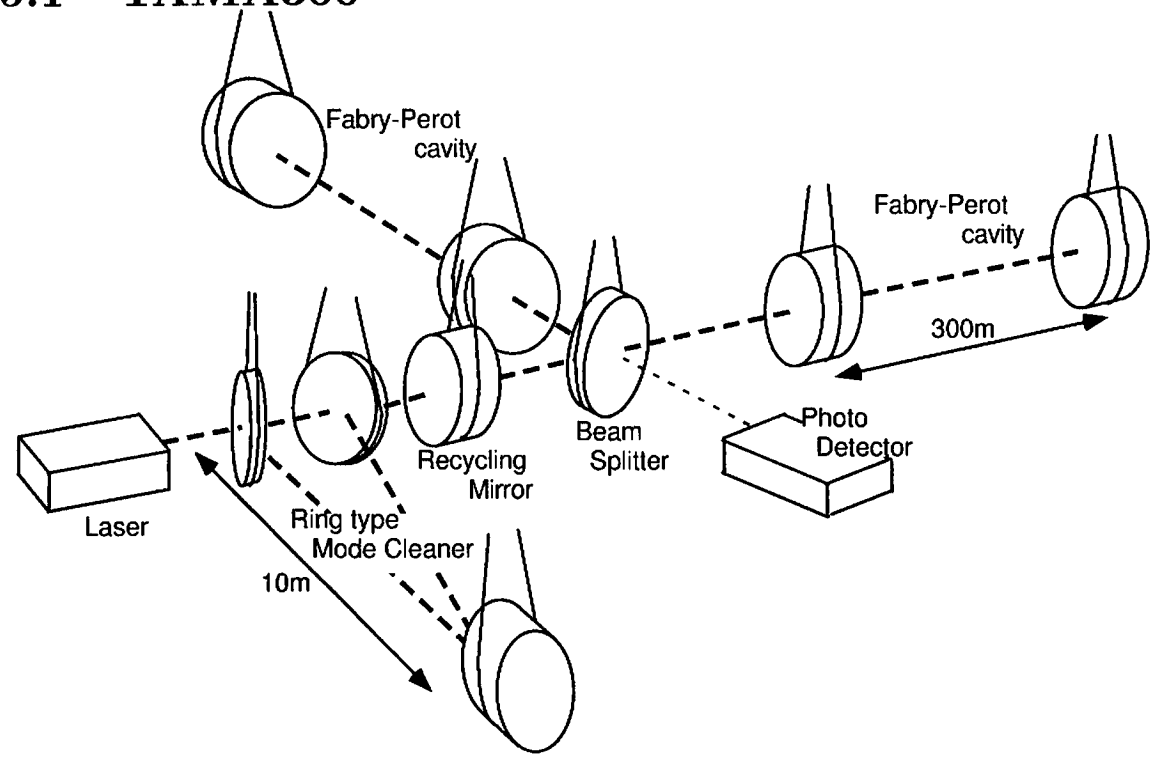

Figure 5.1: The conceptual and optical design of TAMA interferometer

The one arm experiment was executed as one of the phases of the TAMA project. It had

two main purpose. One is the development of the control scheme for the long baseline Fabry-Perot cavity. The other is the estimation of the performance of the optics, the vibration isolation systems and so on. In this section, we see the general view of the TAMA300. The conceptual and optical design of TAMA interferometer is shown in Fig.5.1. Light source is 10W high power laser developed by the SONY Co.[22][23]. Before illuminating to the main interferometer, the light is modulated in phase with EOM and is passed through the 10m ring cavity which is called mode cleaner. The mode cleaner decrease the deformation of the laser mode and beam jitter. As it behaves band-pass-filter, the modulation frequency must be adjusted in order to let sidebands pass through it [35][25]. We will discuss this technique for adjustment in detail in chapter6.

Power recycling technique is adopted in order to increase the light power illuminated to the 300-m Fabry-Perot cavity. Therefore main interferometer, which is called recycled Fabry-Perot-Michelson interferometer(RFPMI), is composed of five mirrors and a beam-splitter.

5.1.1 Infrastructure of TAMA300

The TAMA interferometer is being built in the Mitaka campus of National Astronomical Observatory Japan. The map of the campus is shown in Fig.5.2 The structure of TAMA300 consists of the center room, two end rooms and two corridors. The center room connects with each end room by corridors 1.5m in width and 2m in height. One corridor is extended 300-m long from the center room to the west (E-W arm), the other is to the south (N-S arm).

Fig.5.3 shows the arrangement in the center room at the time of this experiment. There are six chambers in this room . Each near mirror(NM) of both arms, the beam splitter(BS), mode cleaner(MC) cavity, the recycling mirror(RM) and their suspensions are housed in them. Though these chambers are connected by the ducts in the future, the optical table, on which input optics were arranged, was positioned between the BS chamber and the NM (E-W arm) in this experiment. From this table, incident light was illuminated to the NM chamber directly. The Racks for electrical circuits and the instruments were positioned in the room enclosed by the E-W arm and the N-S arm.

In the end room, the chamber for the end mirror, the rack and the optical bench, on which the photodetector monitoring the transmitted light of the cavity, are positioned.

5.1.2 Vacuum Chamber

The effects of acoustic noise and fluctuations in the refractive index of the air are one of the serious problem in operating the Fabry-Perot cavity. To avoid these effects, as mentioned above, the mirrors composing TAMA interferometer are housed in the chamber, optical path in the interferometer is covered by the duct. The chambers and the duct are evacuated

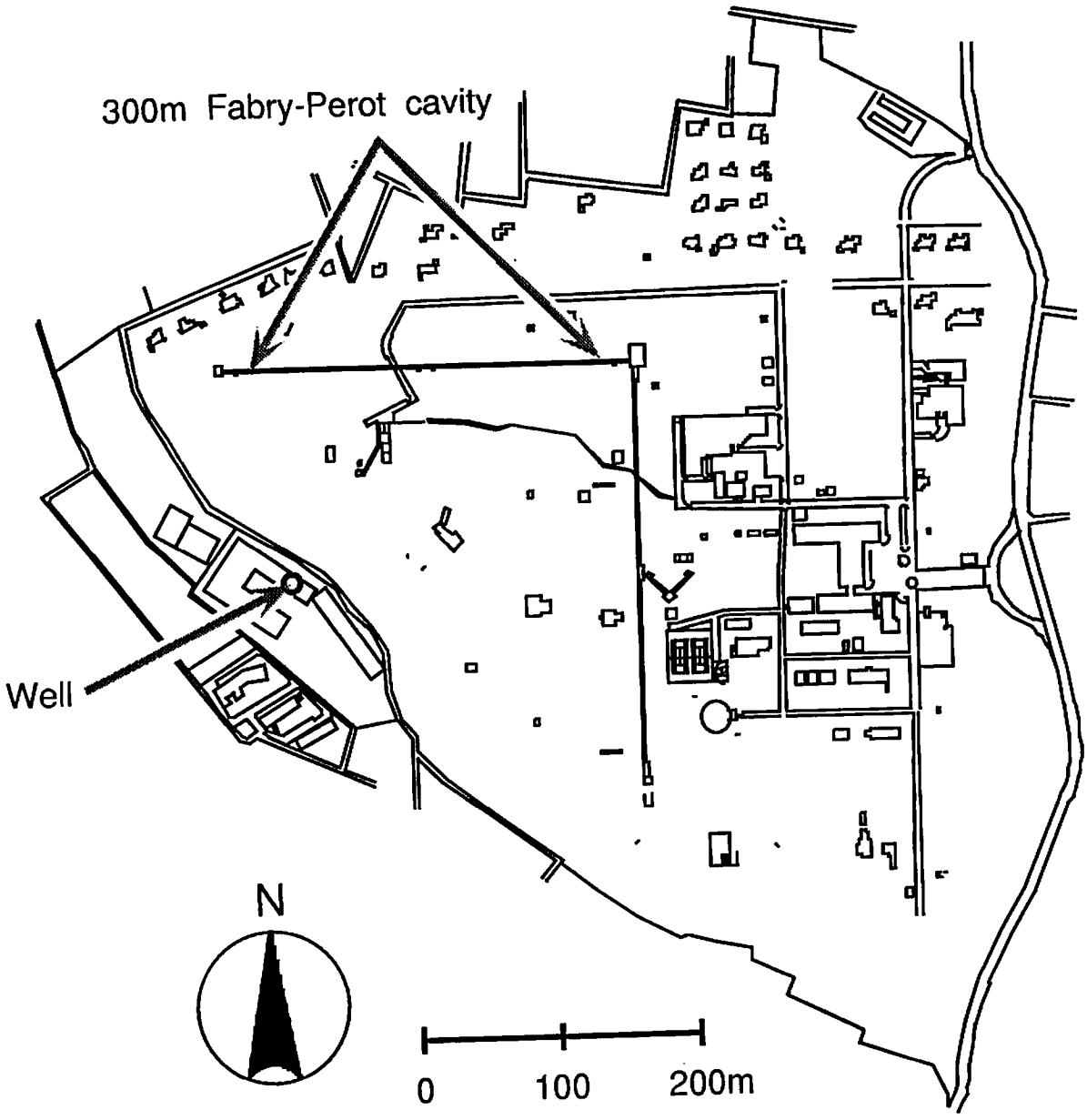

Figure 5.2: The map of the Mitaka campus of National Astronomical Observatory Japan

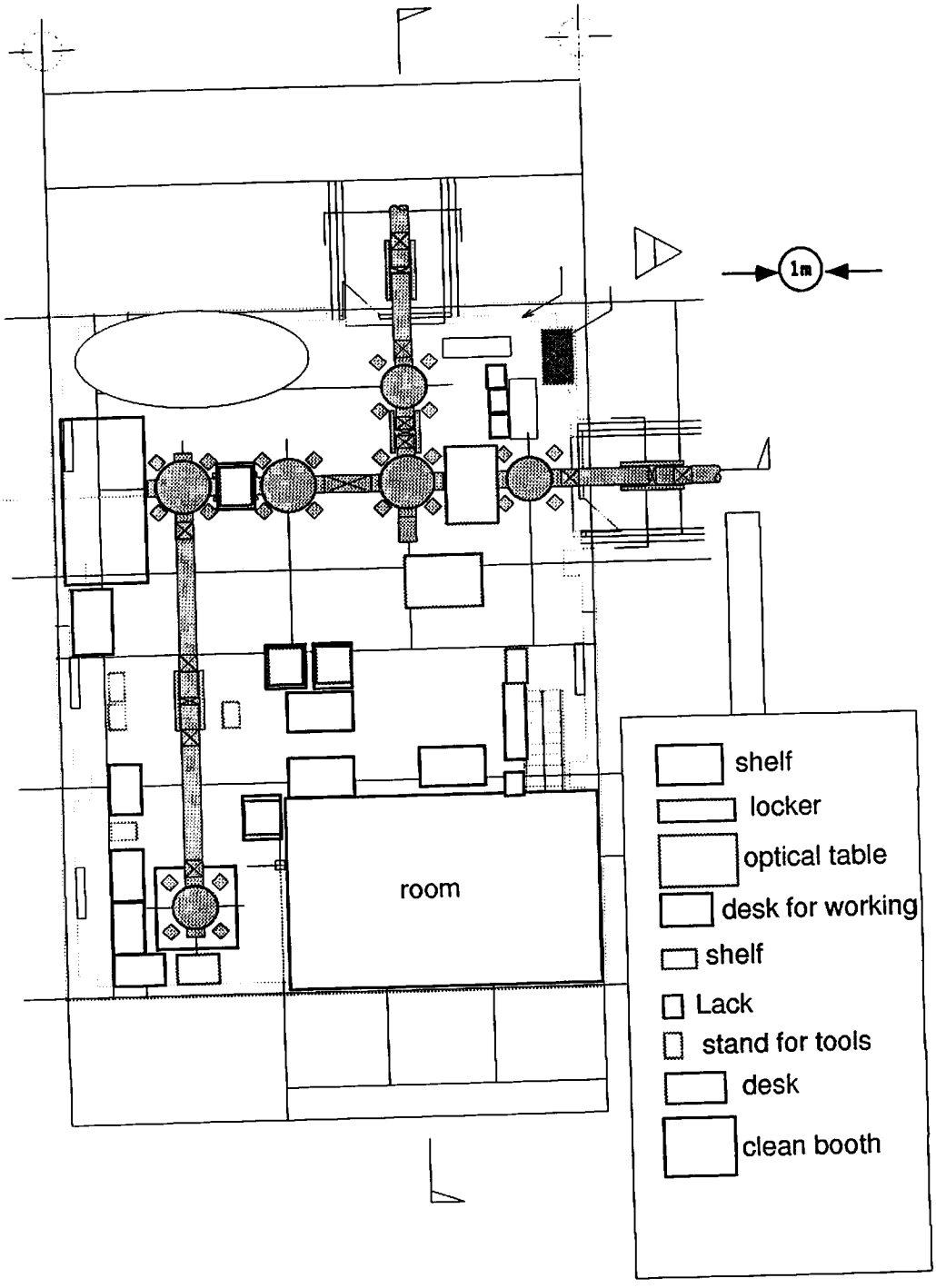

Figure 5.3: The center room of the TAMA300 at the time of this experiment

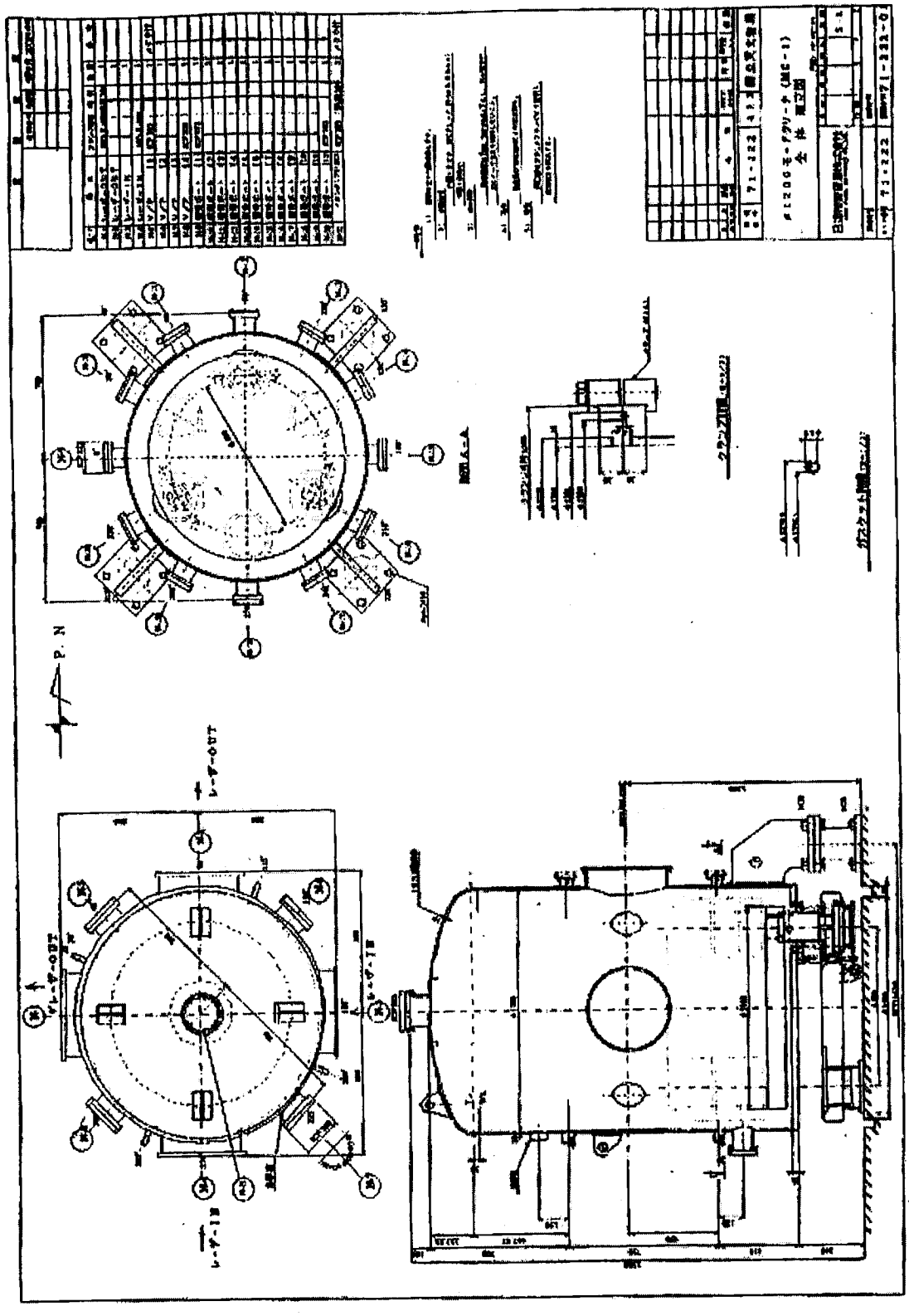

Figure 5.4: The vacuum chamber for the mirrors

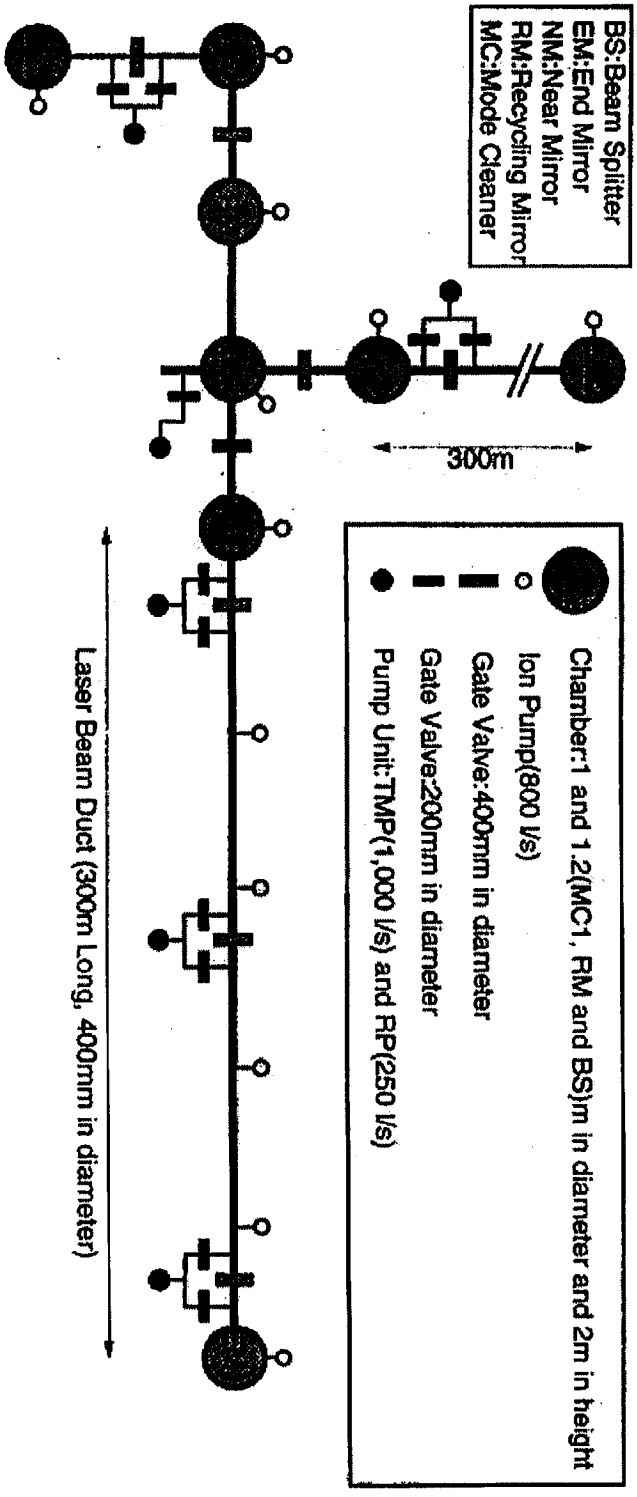

Figure 5.5: The vacuum system of TAMA300

in vacuum. Fig.5.4 shows the shapes of the vacuum chamber. The chamber has a diameter of 1m, a height of 2.3m and is made of SUS304L. The incident light illuminated the cavity through an anti-reflection coated optical window. The chambers are located 300m apart and are connected with the vacuum duct extended along the corridor. The duct has a diameter of 40cm and is made from SUS304. Inside of the duct is a surface treated with electro-chemical buffing(ECB) to achieve a 10^{-6}Pa vacuum level without baking. The chambers and the duct are evacuated with turbo molecular pumps and ion-sputtering pumps. The vacuum system of TAMA300 is shown in Fig.5.5. The system of the E-W arm were utilized in this experiment. This vacuum system attained 2×10^{-5}Pa before installation of the mirrors with the suspension(Near Mirror Chamber). After the installation, the vacuum level was attained 1×10^{-5}Pa. Though it doesn't attained 10^{-6}Pa at Near Mirror chamber, this is enough for our experiment.

5.2 Experimental Setup

The setup of the one-arm experiment is shown in Fig.5.6. The laser light is adjusted its mode to that of the cavity and modulated in frequency through input optics chain. Then it is illuminated to the 300-m Fabry-Perot cavity which is housed in vacuum. Reflected light from the Fabry-Perot cavity is picked up by optical circulator which consists of the $\lambda/4$ plate and PBS. It is splitted by the beamsplitters and go straight on the three paths. One path is reached to an one-segmented photodetector. The detected signal is used for the cavity length control according as Pound-Drever Method. This signal is demodulated and pass through some electrical filter and fed back to the magnet-coil actuator attached to the mirror and PZT actuator for laser frequency control. Another two paths reached to the four-segmented photodetector. The detected signal is used for the alignment control according as Wave Front Sensing technique. and fed back to the magnet-coil actuator attached to the mirror. Then we will explain the each parts.

5.2.1 Fabry-Perot Cavity

Mirror

The specifications of the mirrors are shown in table5.2. The near mirror is a flat and its reflectance is designed $R_N = 98.8\%$. The end mirror is the concave mirror with the curvature radius 450m and its reflectance is designed $R_E = 99.99\%$ These mirrors are all monolithic mirrors and shaped as Fig.5.7. Its diameter is 10cm and its thickness is 6cm. The substrate of the mirror is fused silica and its surface is superpolished by Research Electro-Optics(REO). They are dielectric multi-layer coating mirrors and coated with Ion

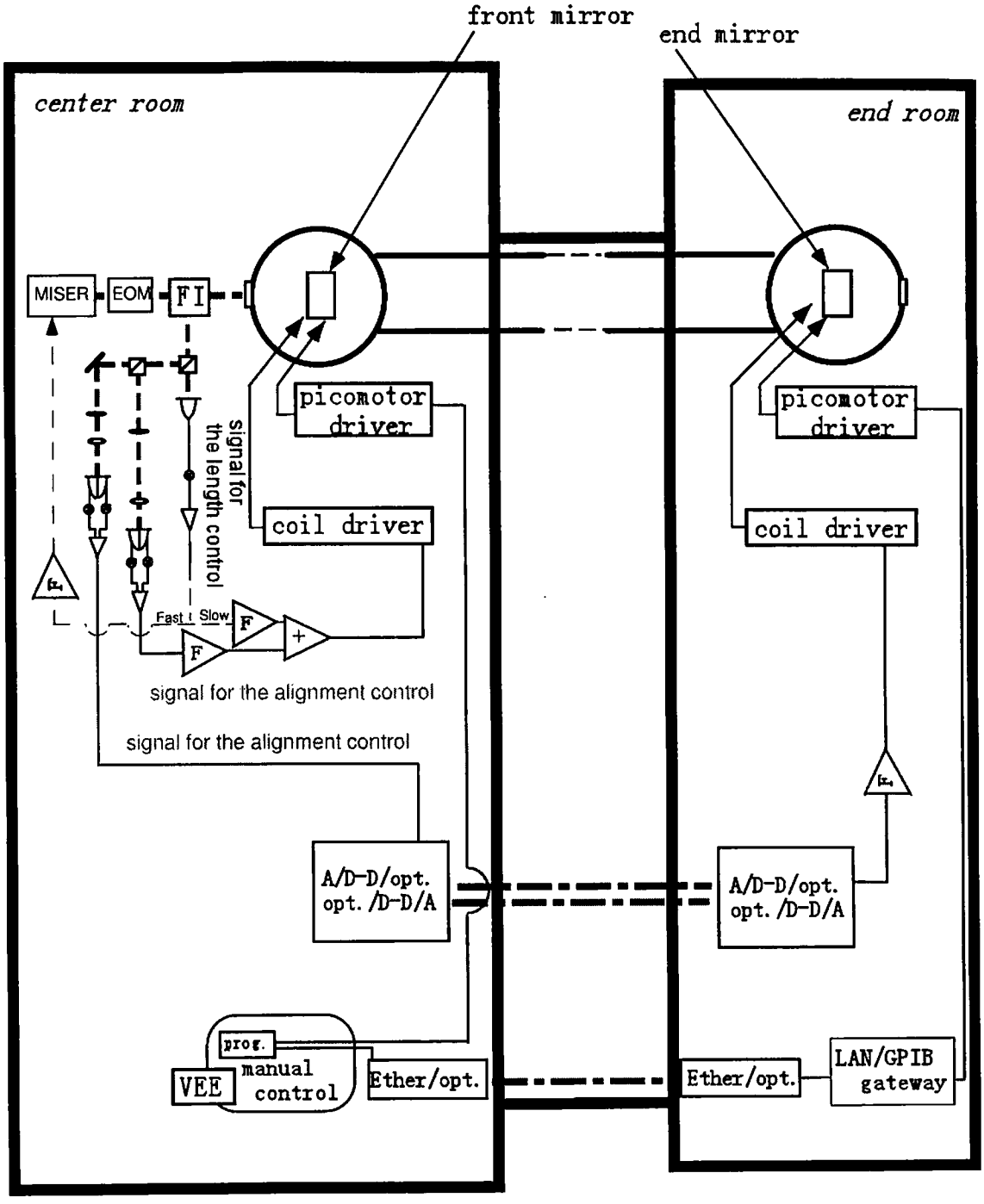

Figure 5.6: The setup of the one-arm experiment

Beam Spatter(IBS) by Japan Aviation Electronics(JAE). [1]

To estimate the mirror properties, we measured the transmittances of the mirrors with setup shown in Fig.5.8. Each mirror is illuminated with the light modulated in intensity by Acousto-Optic Modulator(AOM) The transmitted light power is detected with the photodetector and the component of the modulation frequency is obtained with the spectrum analyzer. Compared to the modulation frequency component of the illuminated light, the transmittance of the mirror is estimated. The result is shown in Table5.3 and approximately coincide with the design.

As mentioned below, all mirrors are suspended independently by wires as double pendulums. Four magnets are attached to the each mirror. The coils corresponding to the magnets are installed and we control the mirror position and orientation by adjusting the current to the coil. The signal of the cavity length control is fed back to the four actuators commonly and the one of the alignment control is fed back to a vertical/horizontal pair of the actuators differentially.

Cavity Specification

Since the mirrors designed the same reflectivities of the TAMA mirrors, the cavity has the same specification of the TAMA Interferometer. The design of the cavity specification is shown in Table 5.1. With the length and alignment control, as mentioned in the next section, we measured cavity transmittance T_{cav} and reflectivity R_{cav}. The results are $T_{cav} =$ 3.27% and $R_{cav} = 96.7\%$.

Next, we measured the cut-off frequency of the cavity. The modulated light in amplitude with AOM is illuminated to the cavity and the modulation frequency component of the transmitted light amplitude. The detail is shown in next chapter.

Cavity Length	L=300m
Finesse	516
Cavity Transmittance	3.27%
Cavity Reflectivity	96.7%
Free Spectral Range	500kHz
Cut-off FrEq.	484Hz
Beam Waist Radius	8.476×10^{-3}[m]
Divergence Angle	3.996×10^{-5}[rad]

Table 5.1: Cavity Specification of one-arm cavity

[1] These mirror are prepared for this experiment. Though the design specification of these mirrors are same with TAMA mirrors, the substrates are different

Near Mirror	reflectivity	98.8%
End Mirror	reflectivity	99.99%

Table 5.2: The specification of the mirrors for 300-m FP cavity

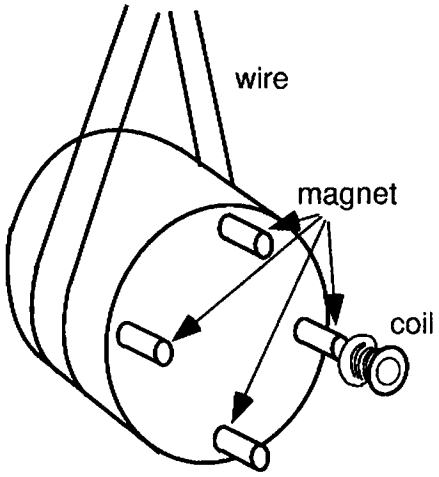

Figure 5.7: Configuration of the suspended mirror and its coil-magnet actuators

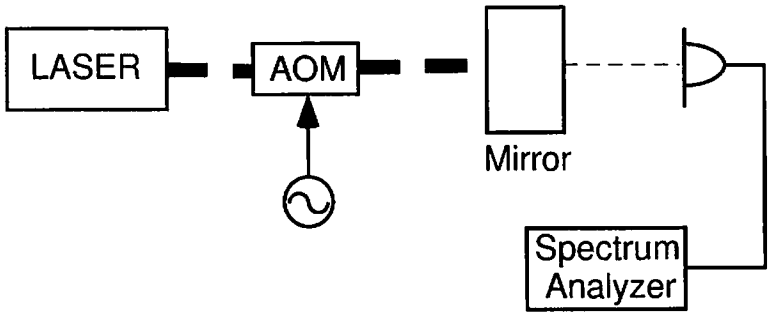

Figure 5.8: Setup to measure transmittance of the mirror

Near Mirror	transmittance	1.41%
End Mirror		0.0118%

Table 5.3: Measured transmittance of the mirror

5.2.2 Vibration Isolation System

Suspension System

Mirror is suspended by the wire. There is two reason. One is based on the principle of the gravitational wave detection. We want to detect a change of the distance between the free masses. So mirror must be considered free mass in the observation frequency range. Other is based on vibration isolation. Ground vibration level estimated at TAMA site is $\sim 10^{-12}\mathrm{m}/\sqrt{\mathrm{Hz}}$ at 300Hz. The designed detector sensitivity is $5 \times 10^{-20}\mathrm{m}/\sqrt{\mathrm{Hz}}$ at 300Hz. Consequently, large isolation ratio is required. By this request this vibration isolation system is developed by the TAMA suspension group, and basically this is used in this experiment. The system consists of the suspension system and stack.

The suspension system is shown in Fig.5.9. In order to obtain required isolation ratio, double pendulum scheme is adopted. In the case of the single pendulum, the isolation ratio of the mirror motion to ground vibration is expressed like this.

$$\text{Isolation ratio of single pendulum} = \frac{\omega_0^2}{\omega_0^2 - \omega^2}, \tag{5.1}$$

where $\omega_0 = \sqrt{g/l}$. In the case of the double pendulum,

$$\text{Isolation ratio of double pendulum} = \frac{2\omega_0'^2}{\omega^4 - 4\omega_0'^2\omega^2 + 2\omega_0'^4}, \tag{5.2}$$

where $\omega_0' = \sqrt{g/l'}$.

Using these expression, suspended mirror motion can be estimated(Fig.5.10). In the observation band, we can see that the double pendulum scheme is satisfied our requirement.

However if the Q-value of the suspension is large, the rms amplitude of the mirror motion is determined at the resonance frequency. Large the rms amplitude cause the degradation of the sensitivity. (For example, increasing leaking light at the anti-symmetric port. the sensitivity degrades by the shot noise.) Therefore, in order to make the Q-value decrease, some dumping system is required. Arranging the strong rare-earth element magnet around the secondary mass, we use eddy current dumping system. Analysis of this suspension system based on some model is done by Arai and Takamori[29][30]. The estimated isolation ratio satisfies our requirements.

As mirror is suspended, when it is controlled with coil-magnet actuator, the response of its motion to current has frequency dependence. We measured this frequency response with photosensor. The result is shown in Fig.5.11. We can see that the resonance frequency is around 1Hz and the Q-value of the resonance is about 3.

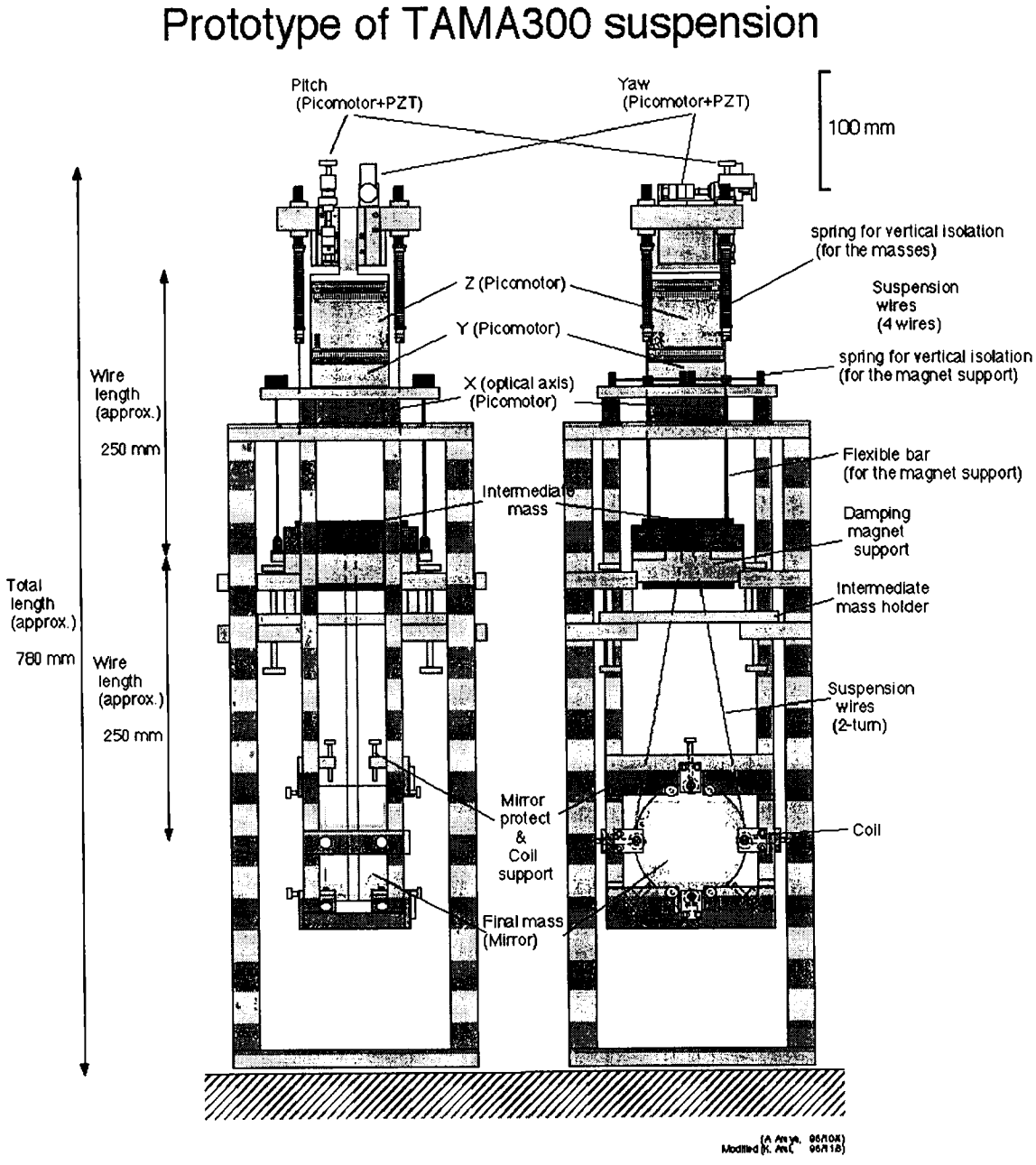

Figure 5.9: The suspension system for the one-arm experiment

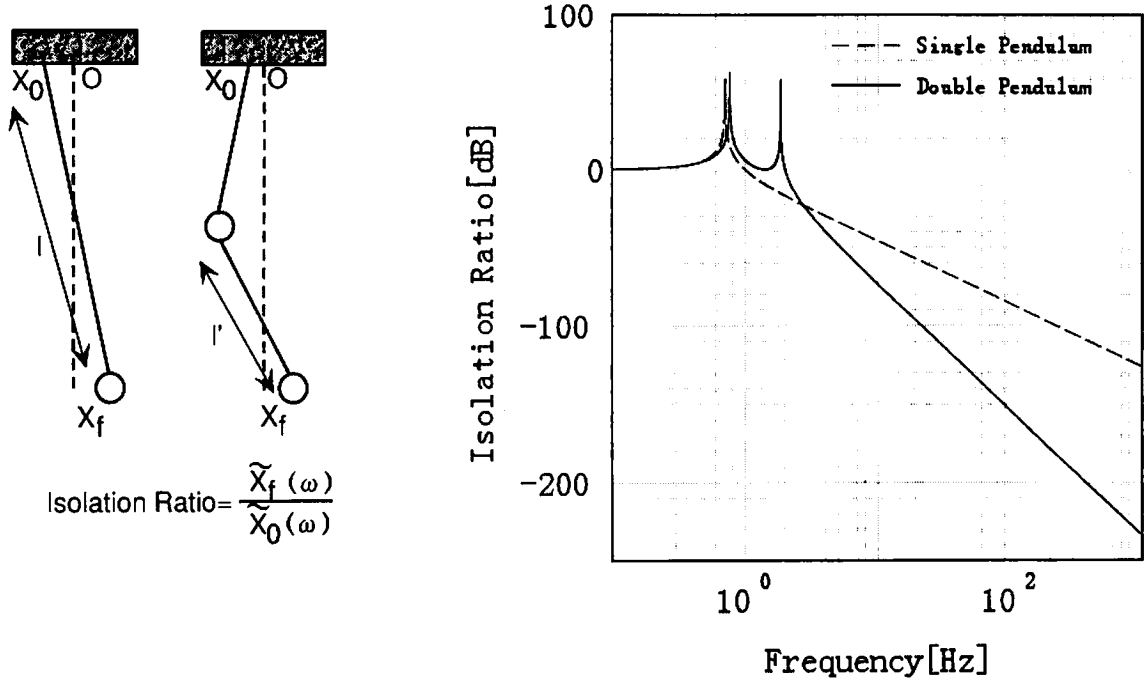

Figure 5.10: The isolation ratio of a single pendulum and a double pendulum

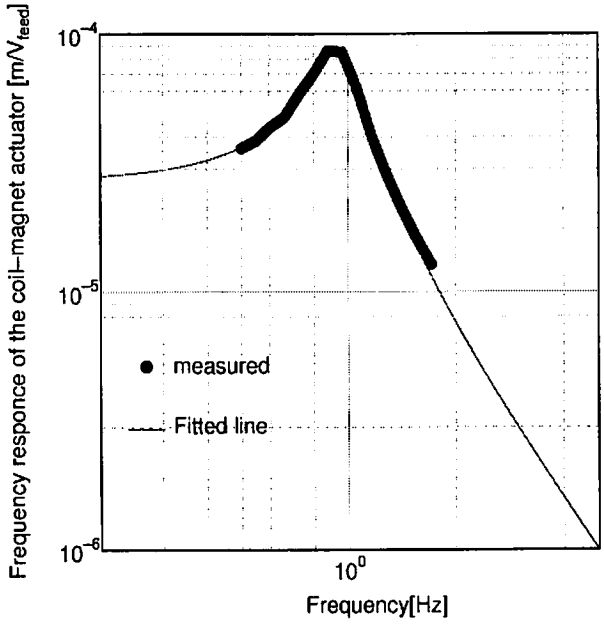

Figure 5.11: The frequency response of the mirror motion, which is measured with photo-sensor

Stack

The suspension is located on optical bench (breadboard). Above 10 Hz, the breadboard of aluminum is also isolated from the vibration by a stack[31][32]. It is loaded on three legs with three stages stack. The stack is composed of SUS block and bellows including rubber. SUS block with 64-67kg weight is used as the mass of stack. Surface processing by ECB(Electro-Chemical Buffing) is performed to this mass block in order to prevent outgas.

Bellows are characteristic of this stack. From vacuum compatibility, fluorocarbon is generally used as rubber material. However the out-gassing is no satisfied specification of ultra high vacuum even fluorocarbon. Complete vacuum compatibility is achieved by covering rubber using bellows. In this case, there is not restriction to the material of rubbers. The bellows have 32 fins. They are more softly designed than inner rubber on expansion and contraction. Since rubber is sealed tightly by bellows in air, bellows behave as air spring. Although the spring coefficient of air spring is smaller than that of rubbers, balance point of spring will deviate from initial one in vacuum. Since we will be able to adjust the height of the breadboard from the portside the vacuum chambers using Double Balanced Bellows mechanism, the deviation will be compensated instead of vacuum braking.

5.2.3 Input Optics Chain

Laser

The laser is model 126-164-700-F produced by Lightwave Electronics Corp. which can provided 700mW light power at 1064 nm. This consists of a monolithic non-planar ring resonator which is turnable in frequency using attached PZT.

Mode Matching Lenses

As explained previous section, the laser light has the modes expressed Hermite Gaussian and the Fabry-Perot cavity has them also. A difference between these mode cause problem about locking acquisition. If we succeed the cavity lock, the power in the cavity will lose partly. To avoid these problems, we must match the mode of the laser to that of the cavity with lenses. Generally, when laser light, which has a waist of mode w_1, pass through the lens, which has the focal length f and located l_1 apart from the waist, after the lens the light has the waist w_2 and the distance from the lens l_2 related next expression.

$$\begin{aligned} \frac{l_1 - f}{l_2 - f} &= \frac{w_1^2}{w_2^2} \\ (l_1 - f)(l_2 - f) &= f^2 - f_0^2, \end{aligned} \tag{5.3}$$

where $f_0 \equiv \pi w_1 w_2/\lambda$. Using this expression, we can decide adequate lenses and their position.

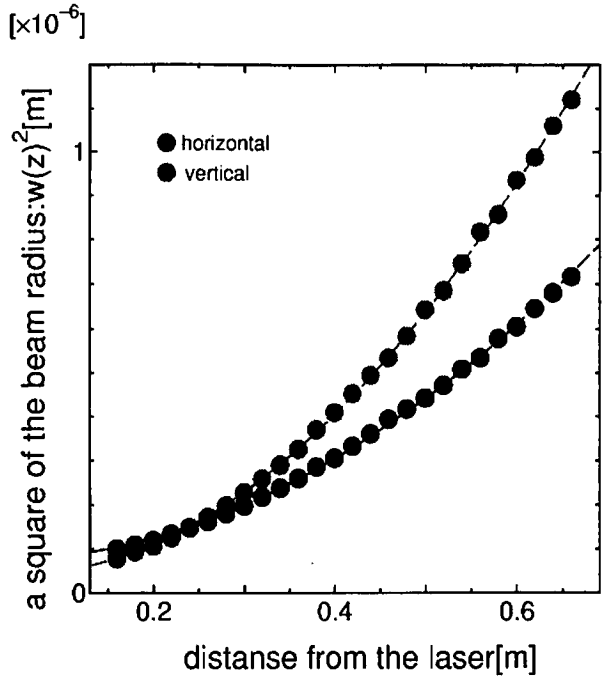

Figure 5.12: The beam profile of the MISER used in this experiment.

The beam profile of this MISER is measured with the beam profiler (BeamScan:Photon, Inc.) and shown in Fig.5.12. We can see the profile along the vertical axis isn't identical with that of horizontal axis. In order to adjust this difference, the cylindrical lenses are located in this chain [2].

EOM and Faraday Isolator

In this input optics chain, Faraday Isolator(FI) and Electro-Optic Modulator(EOM) are also placed. Faraday Isolator removes the light reflected back to the laser from the cavity and avoid the affected the behavior of MISER. We use IO-10-YAG (Optic For Research) as FI.

EOM is the electrical device to modulate light in phase. The sidebands, being proportional to drive voltage, is obtained. We measured modulation index. Modulated light,

[2]In the final stage of the TAMA project, the adjustments with these cylindrical lenses is not sufficient. This difference is considered the deformed wavefront and a ring cavity, called as a mode cleaner, is used to clean the wavefront[25].

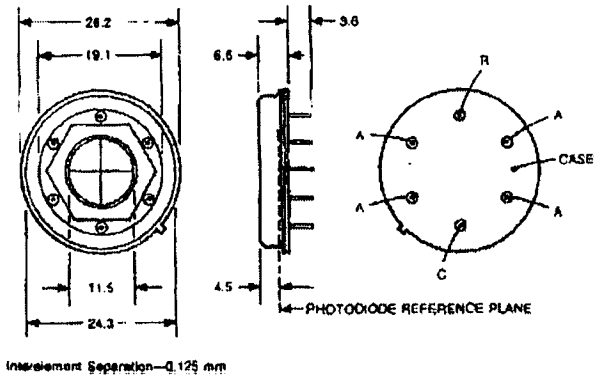

Figure 5.13: The outside appearance of the photodiode YAG-444A-4

which is passed adequate lenses, illuminated the super cavity(Optical Spectrum Analyzer:Newport Co.). As a mirror consisted the cavity is mounted on the PZT actuator, The length of the super cavity can be changed by driving voltage. Monitoring transmitted light, we can measure the power of a carrier and an sidebands. The result of this measurement is

$$\left(\frac{J_1(m)}{J_0(m)}\right)^2 \sim \frac{m^2}{4} = 1.06 \times 10^{-3}. \tag{5.4}$$

From this result, the modulation index is $m \sim 0.065$.

5.2.4 Photo Detector and Demodulator

In this experiment, as mentioned previous section, we adopted two types of the signal detection method for the control of the 300-m cavity. The signal is detected in the reflected light from the cavity by each method and photodetector which can detect signal in Radio Frequency(RF) band and demodulator are needed.

A photodiode used in the photodetector is YAG-444A-4. The outside appearance is shown in Fig.5.13. YAG-444A-4 is a quadrant photodiode and has a large detecting area and good sensitivity for the light of YAG laser, To elevate the Signal-to-Noise ratio at the modulation frequency, we adopted the tank circuit utilized the LC resonance(Fig.5.14),

The resonance curves were measured and the example of them is shown in Fig5.15 We can see Q-value of the resonance is around ten.

SBL-1LH(Mini circuit Co.) is used as double-balanced-mixer(DBM), which is core element of the demodulator. Though some circuits around signal input and output and the offset adjustment are needed, we can obtained the modulated signal with DBM basically.

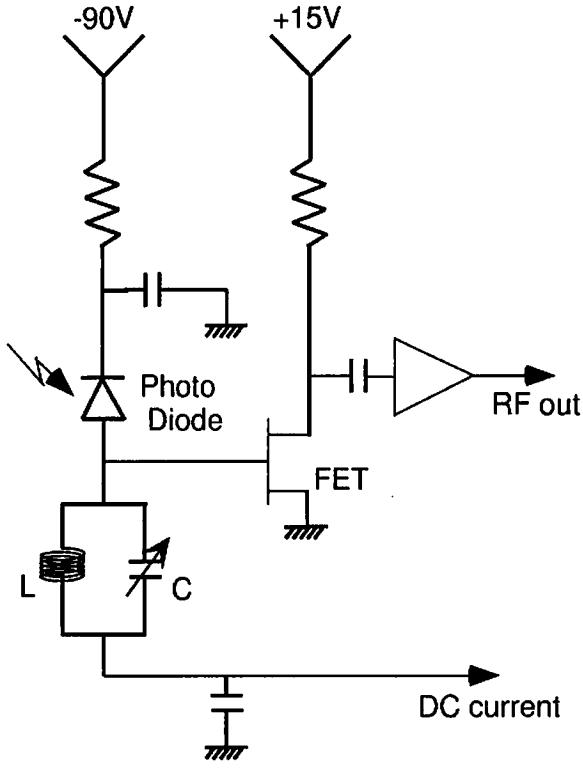

Figure 5.14: The basic design of the photodetector.

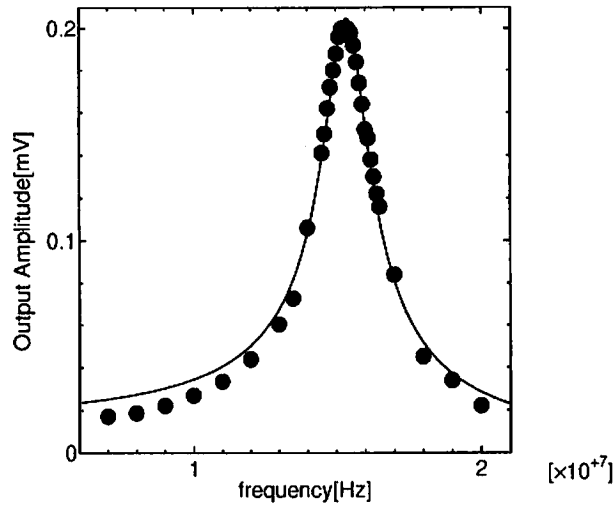

Figure 5.15: The example of the measured LC resonance curve.

We made a basic plan of the circuits for photodetector and demodulator. These circuits are developed, manufactured and tested with Nihon Tsushinki Co.. Though these products are manufactured for the wave front sensors, we used them for the signal detection by the Pound-Drever method.

5.2.5 Signal Transmission at the Interval of 300m

Since the signal of the alignment control is fed back to the both of near mirror and end mirror, the signal fed back to the end mirror must be transmitted at the interval of 300m. In such a case, transmission of the analog signal itself tends to mix of noises. Therefore we use analog-optical signal converter in this experiment. Actually, the analog signal is converted to the digital one and furthermore the digital signal is converted to the optical one. The optical signal is transmitted at the interval of 300m through the optical fiber. The transmitted signal is converted to the analog one again through digital one. The sampling frequency of the analog-digital converter f_s is 11.58kHz and this module has the property on the occasion of the transmission:

$$\text{Phase delay}: \quad \frac{\pi f}{f_s} + 89[\mu\text{sec}] \times 2\pi f[\text{deg}]$$

$$\text{Gain decrease}: \quad \frac{\sin \frac{\pi f}{f_s}}{\frac{\pi f}{f_s}}.$$

As mentioned below, since the control band of the alignment control is narrow, these influence is negligible. However the transmission of the high frequency signal requires the correction.

5.3 Cavity Length Control

With the setup explained in the previous section, we attempted the length control to hold the 300-m cavity exacting resonant condition. This procedures are described as follows.

At first, we let main beam passed through the duct adjusted mode matching lens positions finally. Then the end mirror and the front mirror were stationed. The mirrors were aligned roughly, then the cavity were gone through the resonance condition frequently. The transmitted light and the reflected light of the cavity at the moment of the resonance is appeared the influence of the Doppler effect. Then the electrical servo filter was manufactured. The frequency response of the 300-m Fabry-Perot cavity and the actuators are accounted for their design. Finally, the signal detected by the Pound-Drever method was fed back to the actuators through the servo filter and we succeeded the lock of the 300-m

Fabry-Perot cavity. The transmitted light and the reflected light of the cavity in the locking condition, they are fluctuated largely at 6 Hz. It is the resonance frequency of the pitch motion of this suspended mirror.

In this chapter, This procedure is explained in sequence.

5.3.1 Initial Alignment

At first, as mentioned above, we must let the light pass through the duct which has 300-m length. Moreover we must adjust the positions of lenses again, since the beamprofile in 300m apart tend to differ from what we require. In order to reduce the difference, the light was illuminated through the corridor outside the duct. Then we adjusted roughly mode matching lenses to obtain the adequate beamprofile in 300m apart and introduced the light to the duct by adjusting the steering mirror.

We have targets, which can take in and out in vacuum, in 10m apart from center of chambers. The light is introduced to the target in 10m apart then to the one in 290m apart. Though position of the target were fixed with accuracy from the beginning, we obtained the position and the input beam axis by trial and error.

Then we put the suspended mirror at the end chamber. The target was set slightly below the input beam axis. Reflected light from the end mirror was introduced to the targets and then lifted up slightly. In that manner, we fixed the reflected beam axis. Lastly, we put the suspended mirror at the front chamber and repeated the same procedure and then we fixed the cavity axis roughly. At this time, the cavity is passed through the resonance condition in motion of the mirror.

5.3.2 Behavior of Cavity Resonance without Length Control

After the procedure of the initial alignment, the cavity pass through the resonance condition. On that occasion, the behavior of reflected light (or transmitted light) is expected to be as shown in Fig.3.4.

Fig.5.16 shows intensity of the reflected light from the Fabry-Perot cavity. Fluctuation in the middle of the graph represents the behavior of the cavity resonance. It differs from Fig.3.4. This fluctuation is due to Doppler shift caused by the mirror motion.

For simplicity, we assume the situation that one of the mirror is moving at the velocity v. The field of reflected light is expressed as (see Appendix A)

$$E_r = E_0 \left[-r_f + t_f^2 r_e \sum_{n=0}^{\infty} (r_f r_e)^n \exp\left\{ -j \frac{(c+v)^n}{(c-v)^{n+1}} 2(n+1) L\omega_0 \right\} \right], \tag{5.5}$$

where L is the cavity length. From this equation, we can see that the phase change due to Doppler shift is significant under these condition: v is large, $r_e r_f$ is nearly equal to

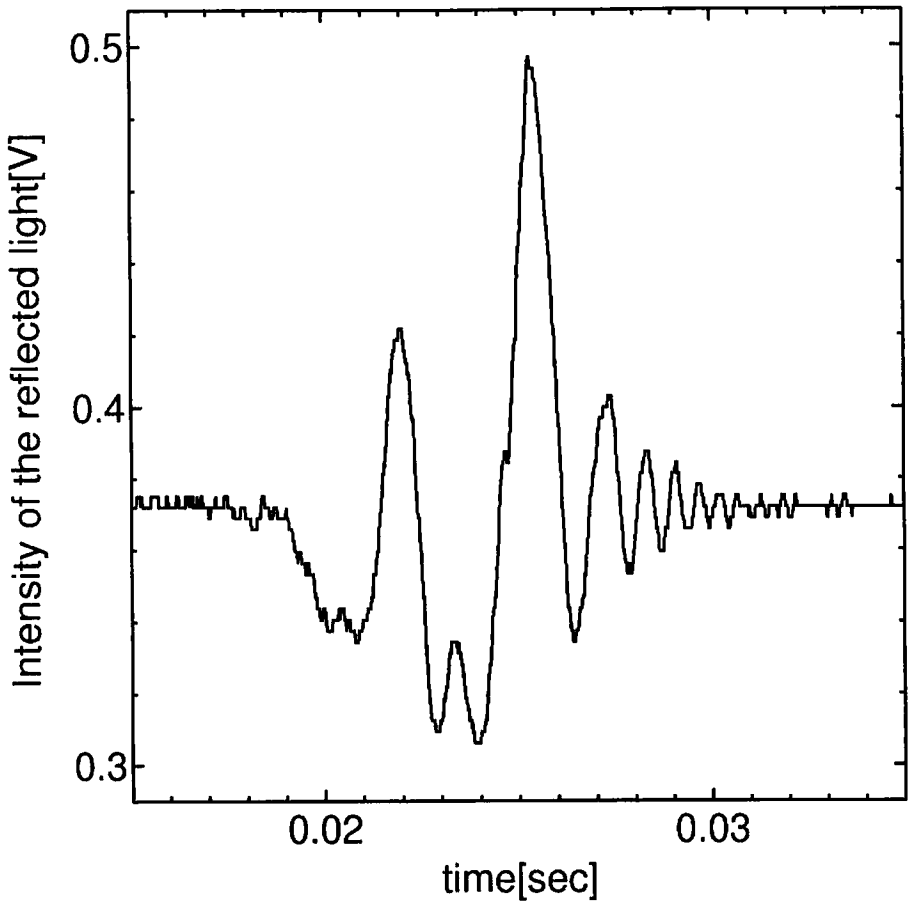

Figure 5.16: Behavior of Cavity Resonance without Length Control

unity and the cavity has a long baseline. Since we have never seen such effect with other suspended Fabry-Perot cavities whose parameters of mirrors are same with this cavity, this fluctuation is thought to be due to cavity length. While from the result of the simulation, roughly we can see that mirrors are fluctuated at about 1μm intervals (see Appendix A).

5.3.3 Setup of the Length Control

There are two ways to adjust the deviation from the cavity resonance, which is detected by the Pound-Drever method. One is the adjustment of laser frequency and another is the adjustment of the cavity length. In this experiment, we adjust both of them. Because the origins of the deviation are different according to the frequency range. In the low frequency region ($<\sim$ 10Hz), the origin is excitation due to ground vibration. In the high frequency region ($>$ 100Hz $\sim$), it is the frequency noise of the laser. Therefore we divide the frequency range with electrical filters and the signal is fed back to two actuators. The laser frequency is controlled with the PZT attached to a monolithic non-planar ring resonator. The cavity length is controlled with the coil-magnet actuator. The setup is shown in Fig.5.6

5.3.4 Behavior of Cavity Resonance with Length Control

We controlled the cavity length and the laser frequency with the setup shown in the previous section. (We call this control *length control.*) Fig.5.17 shows the behavior of the transmitted light with the length control. Though the transmitted light is fluctuated, it keeps high value while servo works. This fluctuation is caused by the mirror fluctuation mainly due to the resonance of double pendulum system. Though we attempted to align the mirrors manually, this fluctuation remained. The magnitude of the mirror fluctuation is discussed later.

The error signal goes to around zero with the length control. This means the servo mechanism works well.

5.3.5 Transfer Function of the Servo

Servo Design

Setup for the length control is shown in Fig.5.18. As mentioned above, the length control consists of two feed back loops. We call the cavity length control loop *mass loop* and the laser frequency control loop *PZT loop.* Since the suspended mirrors are fluctuated largely at around the resonance frequency of the double pendulum system, high gain is required in low frequency region ($\sim$ a few Hz). These mirrors, however, have an internal mode with very high Q-value at around 20 $\sim$ 30 kHz. Therefore the feedback signal to the mirrors is suppressed sufficiently in high frequency region (10kHz $\sim$). With foregoing in mind, the two-pole low pass filter of which the time constant is 300Hz is inserted in the mass loop.

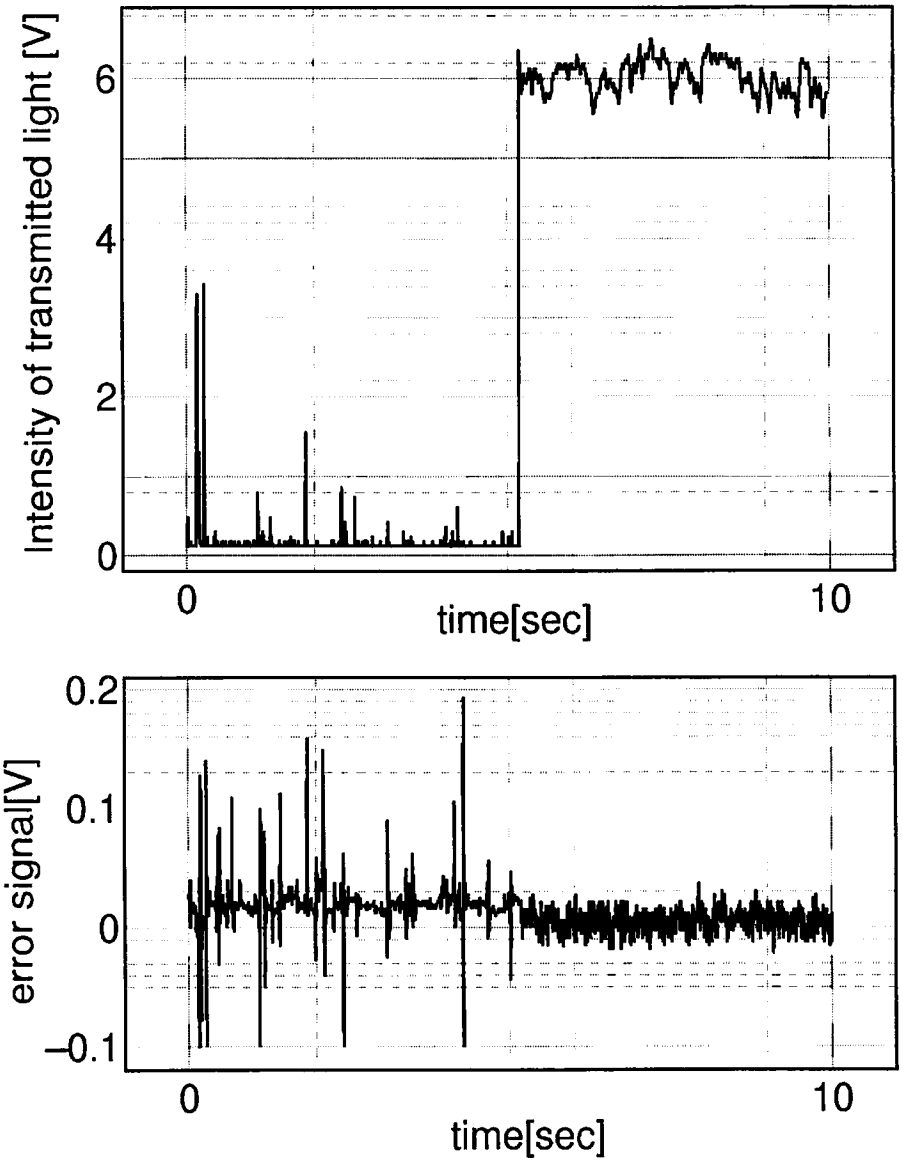

Figure 5.17: Behavior of Cavity Resonance with Length Control

While the control range of the PZT loop covers high frequency region ($\sim$ 20kHz) and determine the unity-gain-frequency (UGF) of this servo. In this experiment, we set UGF to be 10 $\sim$ 20kHz. To realize the stable operation of the servo, the sufficient phase margin at UGF is required. As the 300-m cavity behaves the one-pole low pass filter of which the cut off frequency is 500Hz, the PZT loop filter must advance the phase around UGF to obtain the sufficient phase margin. Therefore we design the filter shown in Fig.5.18 and insert it in the PZT loop.

Transfer Function of the Servo

In order to grasp the total openloop gain of the servo, we measure the cross frequency between the two loops at first. The setup for this measurement is shown in Fig.5.19. In this figure, $G_{PZT}(\omega)$ represents the transfer function from the electrical filter shown in previous section to the response of PZT actuators of the laser, $G_{mass}(\omega)$ represents the transfer function from the electrical filter to the response of coil magnet actuator and $H(\omega)$ represents the transfer function from the cavity response to the detecting system (photo detector and demodulator). We measured the transfer function V_O/V_I with spectrum analyzer(Dynamic Signal Analyzer 35670A:Hewlett Packard Co.). The measured quantity is expressed as

$$\frac{V_O}{V_I} = -\frac{1 + HG_{PZT}}{HG_{mass}}. \tag{5.6}$$

Under the approximation $HG_{PZT} \gg 1$

$$\frac{V_O}{V_I} \sim -\frac{HG_{PZT}}{HG_{mass}}. \tag{5.7}$$

Therefore PZT loop and mass loop cross each other at the frequency where this transfer function is unity. From Fig.5.19, we can find the cross frequency is 35Hz.

While the total openloop transfer function $H(G_{PZT} + G_{mass})$ can be measured with the setup shown in Fig.5.20. The result and fitting are also shown in the figure. In the fitting function, we assumed that the cut off frequency of the cavity is 1kHz. The total openloop transfer function was not measured successfully under a few kHz. The reason is thought that the loop gain is so high that the signal is saturated.

From the results shown in Fig5.19 and Fig.5.20, we can estimate the total openloop transfer function over a wide range. The result is shown in Fig.5.21.

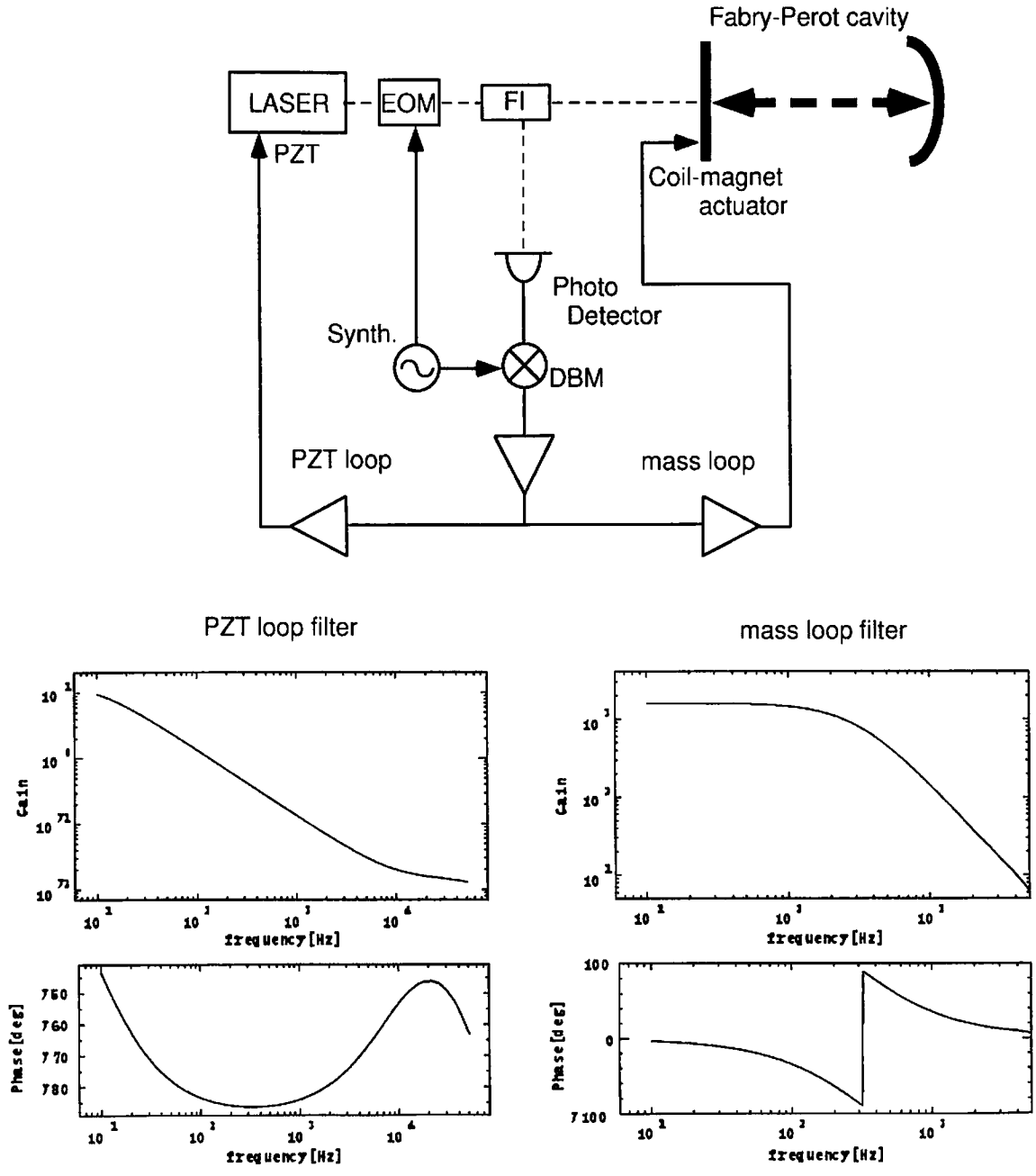

Figure 5.18: Setup for the length control and transfer functions of filters

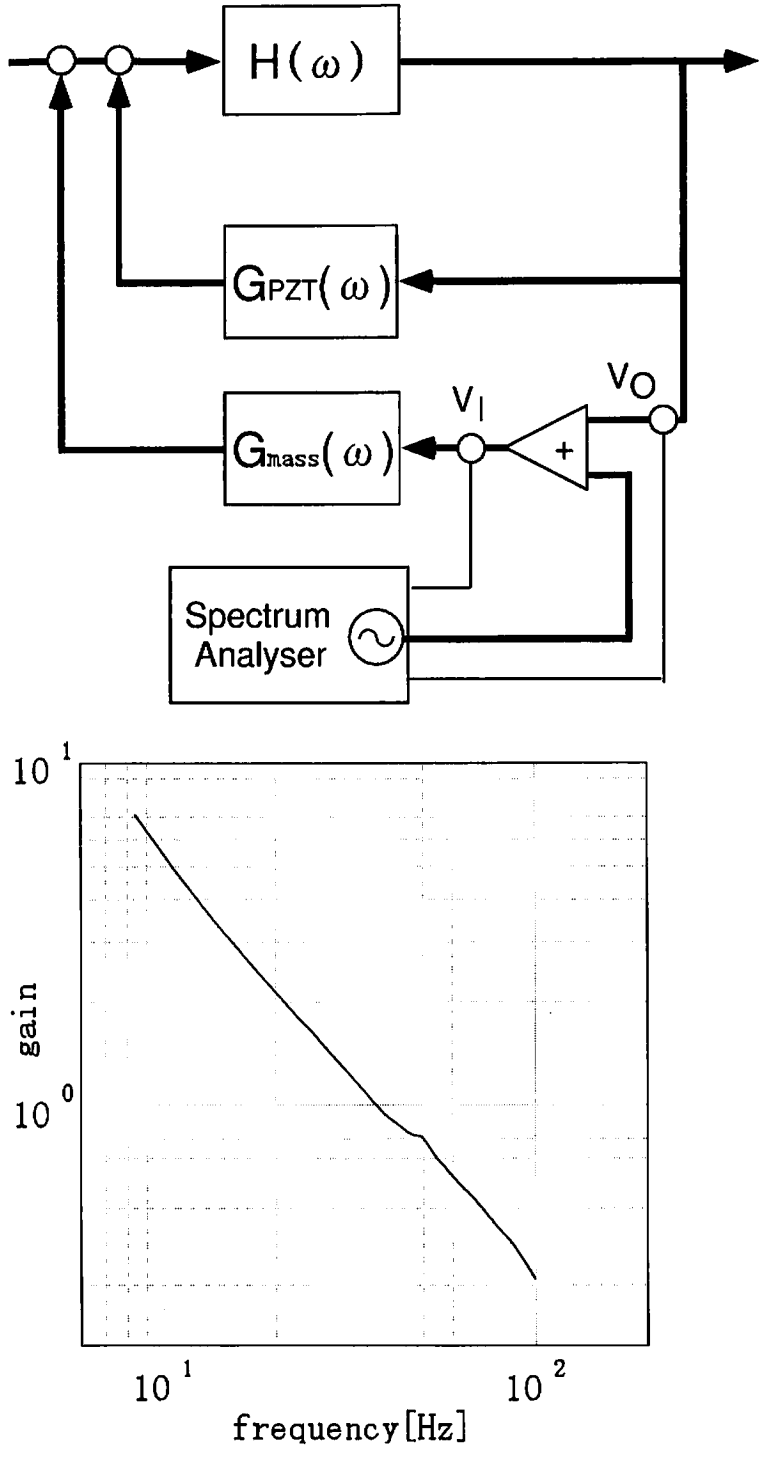

Figure 5.19: Setup for measuring cross frequency of the servo and the result

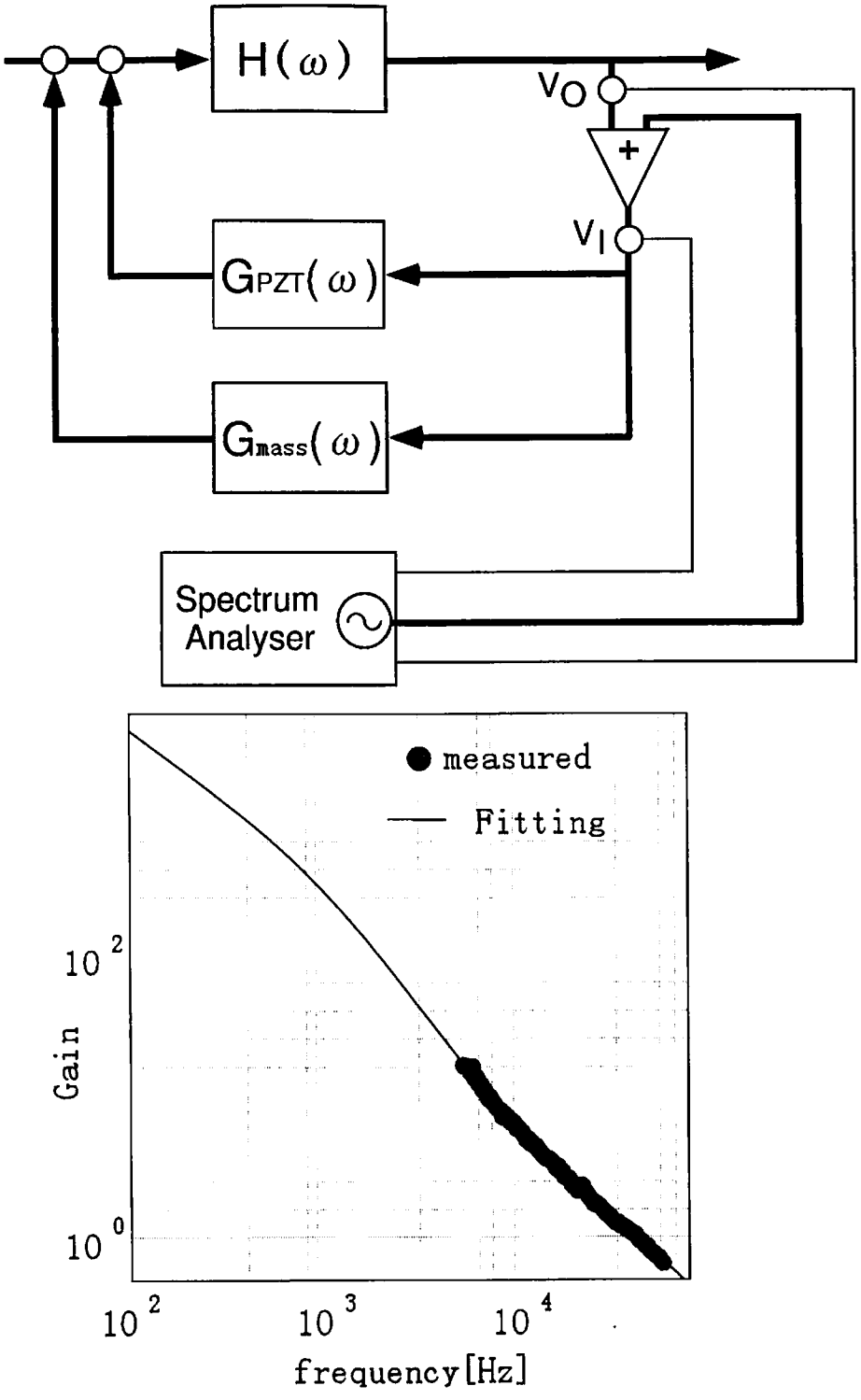

Figure 5.20: Setup for measuring openloop transfer function of the servo and the result

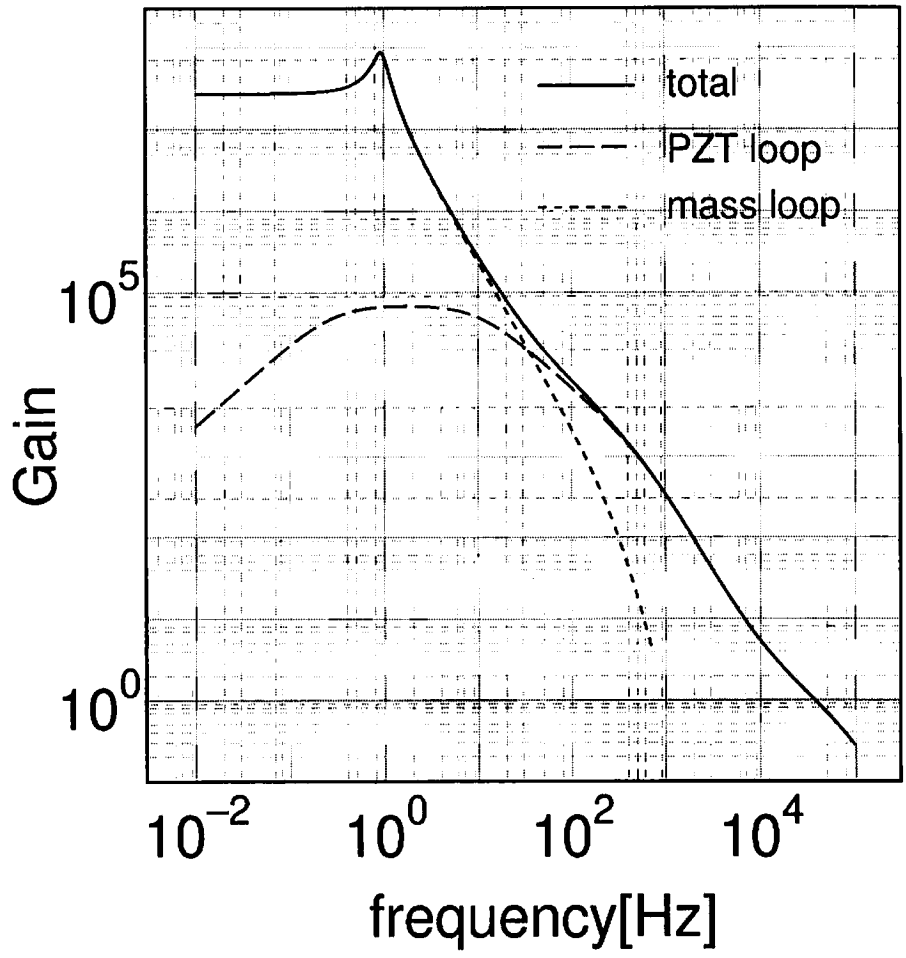

Figure 5.21: The estimated total openloop transfer function of the length control servo

5.3.6 Noise Spectrum of Length Control

Calibration with Michelson interferometer

Operating the cavity with the servo shown in previous section, we obtain the value to observe. We measure the error signal or the feedback signal and translate them into units to obtain, such as displacement or frequency. For that purpose, we calibrate the response of the actuator. In this experiment, we use Michelson interferometer for this calibration.

The setup is shown in Fig.5.22. Since the signal of the length control is only fed back to the front mirror, we calibrated the response of the coil-magnet actuator of it. As the front mirror is suspended, it is fluctuated larger than the wavelength of light ($\sim 1\mu$m). Therefore, as shown in Fig.5.22, interfered light blinked at the antisymmetric port. The interference fringe is expressed as

$$V_{\rm error} = \frac{V_{max} - V_{min}}{2} \sin 2\pi \left(\frac{\delta x}{\lambda/2} \right). \tag{5.8}$$

We detected it with photodetector and controlled it to remain at the point of $\frac{V_{max}-V_{min}}{2}$. Around this point, Eq.5.8 is approximated as

$$\delta V_{\rm error} = \frac{\pi(V_{max} - V_{min})}{\lambda} \delta x. \tag{5.9}$$

This expression is the response of the Michelson interferometer from the displacement δx to the detector $V_{\rm error}$. In this measurement, $V_{max} = 1.69$[V] and $V_{min} = 0.29$[V]. Then

$$H_{MI} \equiv \frac{\delta V_{\rm error}}{\delta x} = 1.66 \times 10^7 [\mathrm{V/m}]. \tag{5.10}$$

We measured the total openloop transfer function of this servo in the next place. The result is shown in Fig.5.23. Though it was not measured well, this is because the rigid mirror is shaken by the influence of the vacuum pump rotation.

Then we measured the transfer function of the electrical filter. From these information, we estimated the response of the actuator. Under the condition of $f \ll 1$Hz(resonance frequency of pendulum), the response is expressed as

$$A_m \equiv \frac{\delta x}{\delta V_{\rm feedback}} = \frac{1.85 \times 10^{-5}}{f^2} [\mathrm{m/V}]. \tag{5.11}$$

While we estimated the response of the Fabry-Perot cavity with the setup shown in Fig 5.24.

The measurement value V_O/V_I is expressed as

$$\frac{V_O}{V_I} = \frac{H_{FP} A_m}{1 + H_{FP} A_{PZT} G_{PZT}}. \tag{5.12}$$

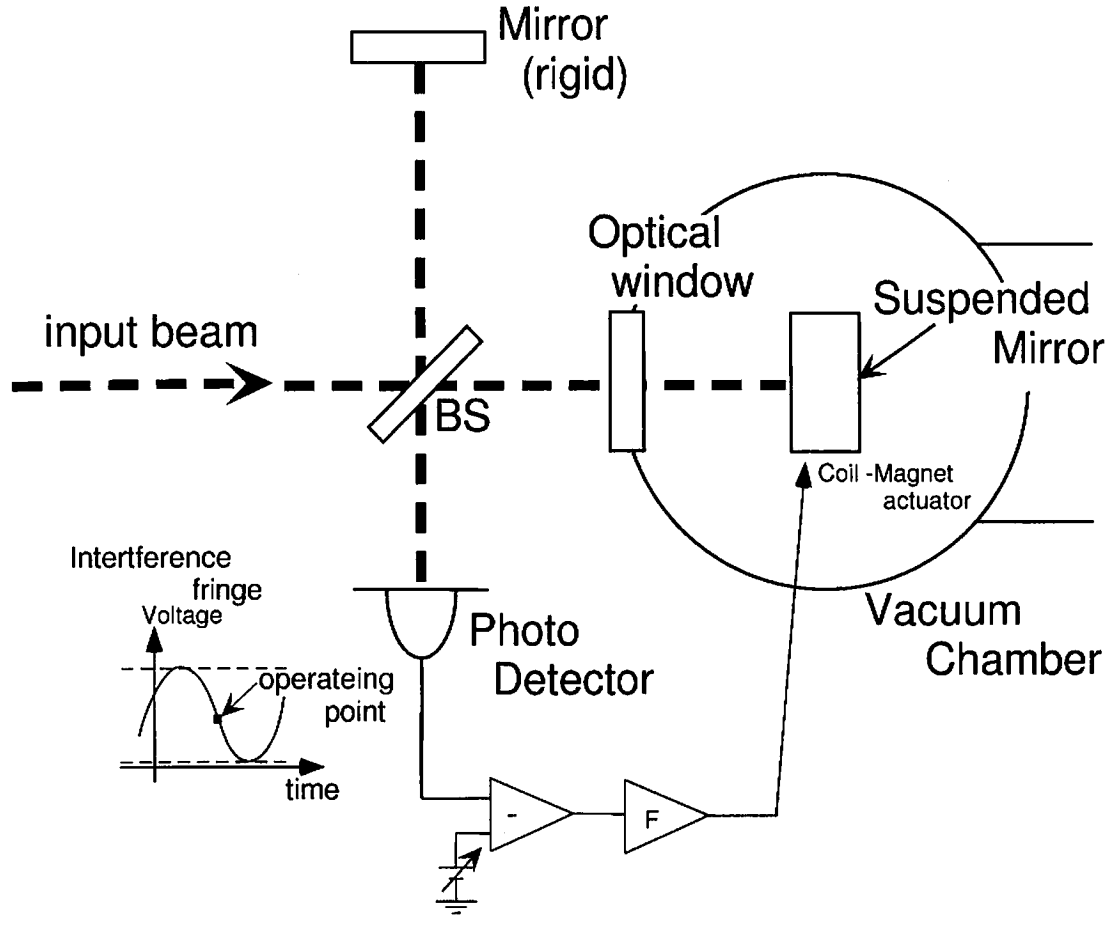

Figure 5.22: The setup for calibration with Michelson interferometer

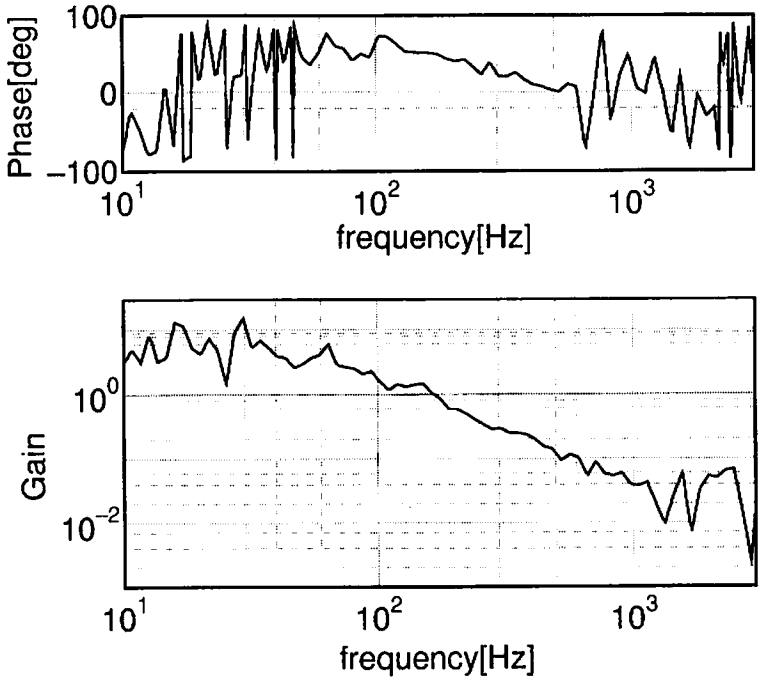

Figure 5.23: The openloop transfer function of the servo for Michelson Interferometer.

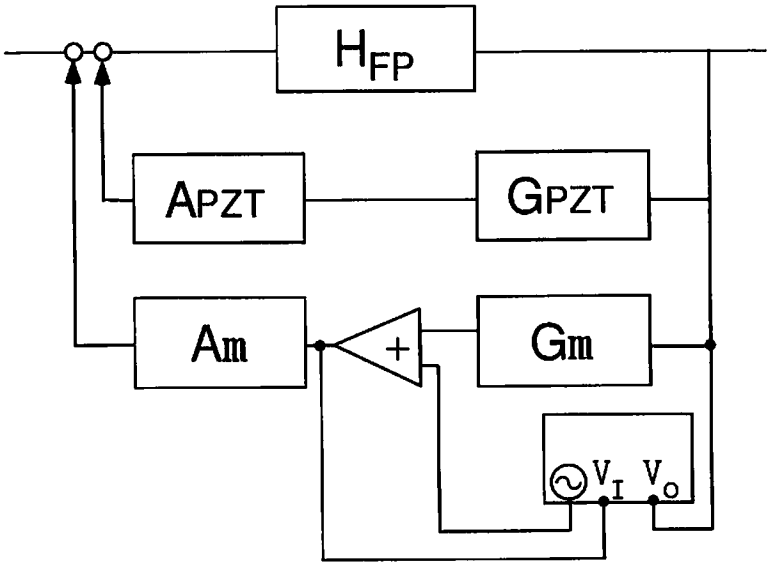

Figure 5.24: The setup of the measurement for the response of the Fabry-Perot cavity

where A_m and A_{PZT} are the response of the actuator, G_{PZT} is the transfer function of the electrical filter of the PZT loop and H_{FP} is the response of the Fabry-Perot cavity. From this equation, we can obtain the estimation of the response of the Fabry-Perot cavity. The result is

$$H_{FP}(DC) \sim 2.51 \times 10^2 H_{MI} \sim 4.16 \times 10^9 [\mathrm{V_{error}/m}]. \tag{5.13}$$

Noise Spectrum of Length Control

We measured the power spectrum of the error signal. The result is shown in Fig.5.25. Solid line shows the power spectrum corrected to the displacement sensitivity with the cavity response H_{FP}. Dotted line shows the power spectrum corrected with H_{FP} and the openloop gain. Two major noise sources contribute to the corrected line. One is the contribution from the ground vibration. The other is that from the frequency noise of the laser.

The contribution from the ground vibration is calculated as following. The behavior of the ground vibration is expressed as

$$\frac{10^{-7}}{f^2} [\mathrm{m}/\sqrt{\mathrm{Hz}}] \quad (f \geq 0.1\mathrm{Hz}). \tag{5.14}$$

Multiplying the approximated vibration isolation ratio of the stack and that of the double pendulum, we can obtain the calculated line of the contribution of the ground vibration (dashed line in Fig.5.25).

While the contribution of the laser frequency noise is estimated from the typical frequency noise level of the MISER of The Lightwave Corp, That is expressed as

$$10^2 \left(\frac{100\mathrm{Hz}}{f} \right) [\mathrm{Hz}/\sqrt{\mathrm{Hz}}]. \tag{5.15}$$

The calculation of the contribution of the laser frequency noise is dot-dashed line in Fig.5.25. We can see that these calculated line overlap the corrected line roughly.

5.4 Alignment Control

5.4.1 Setup

The alignment control scheme is shown in Fig.5.6. As mentioned in the previous section, we obtained the signal for the alignment control with Wave Front Sensing technique. Two quadrant photodetectors are utilized for the signal detection with the Wave Front Sensing technique. The signal separation between the front mirror and the end mirror is realized by adjusting the Guoy phase shift to the quad-PD. For the sake of this adjustment, the different lens sets are used. The signal is demodulated and took the difference between the

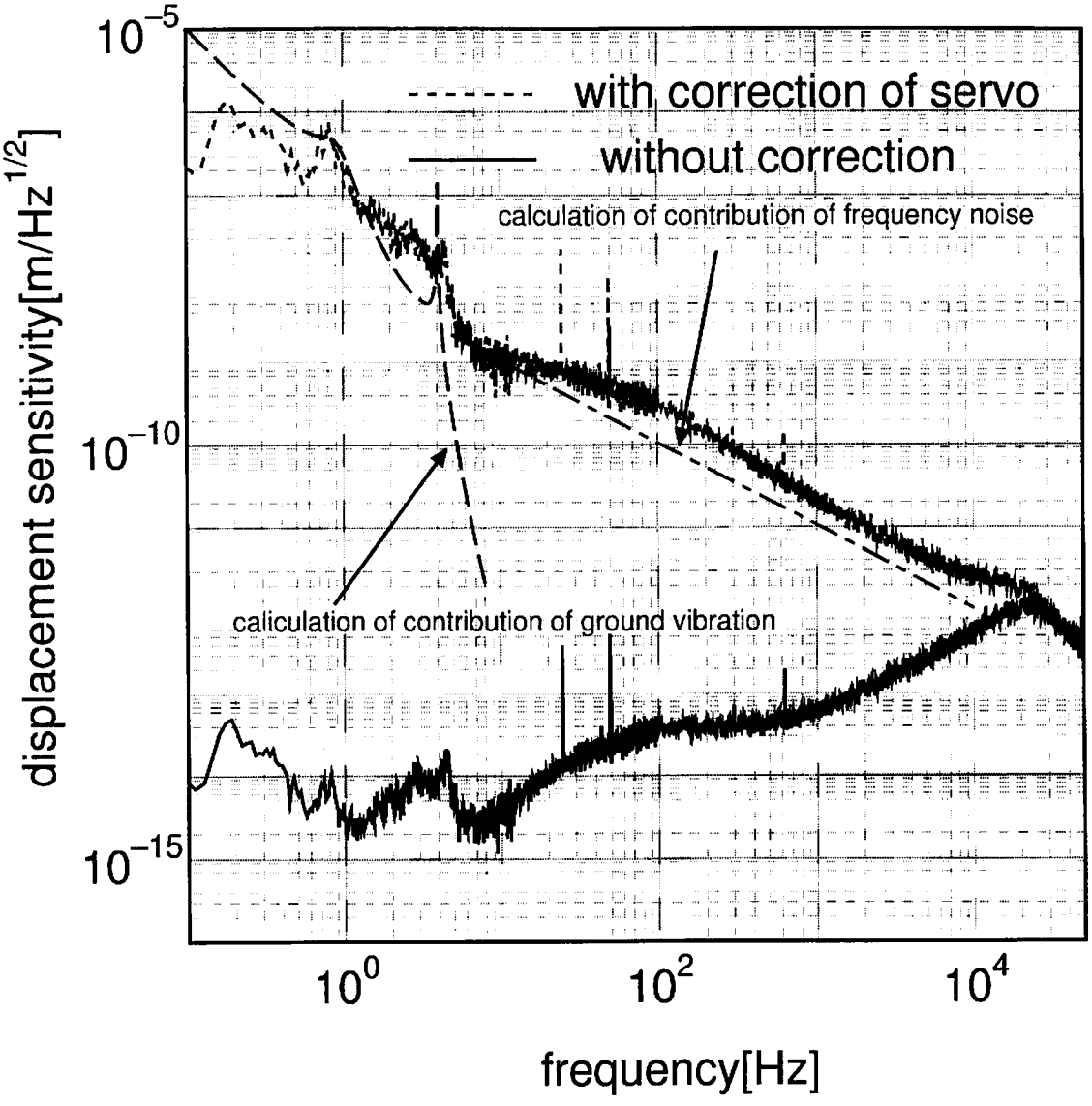

Figure 5.25: Noise spectrum of the error signal of the length control servo

a vertical/horizontal pair of the segments. Through the adequate servo filter, this signal is fed back to the coil-magnet actuator and the mirror orientation is controlled. To transfer the signal to the end mirror which is located 300m apart, we use fiber optic systems. Therefore we developed the module which convert the analog signal into the optical one through digital conversion. The transferred optical signal is restored to the analog one and applied to the coil-magnet actuator.

5.4.2 Behavior of Cavity Resonance with Alignment Control

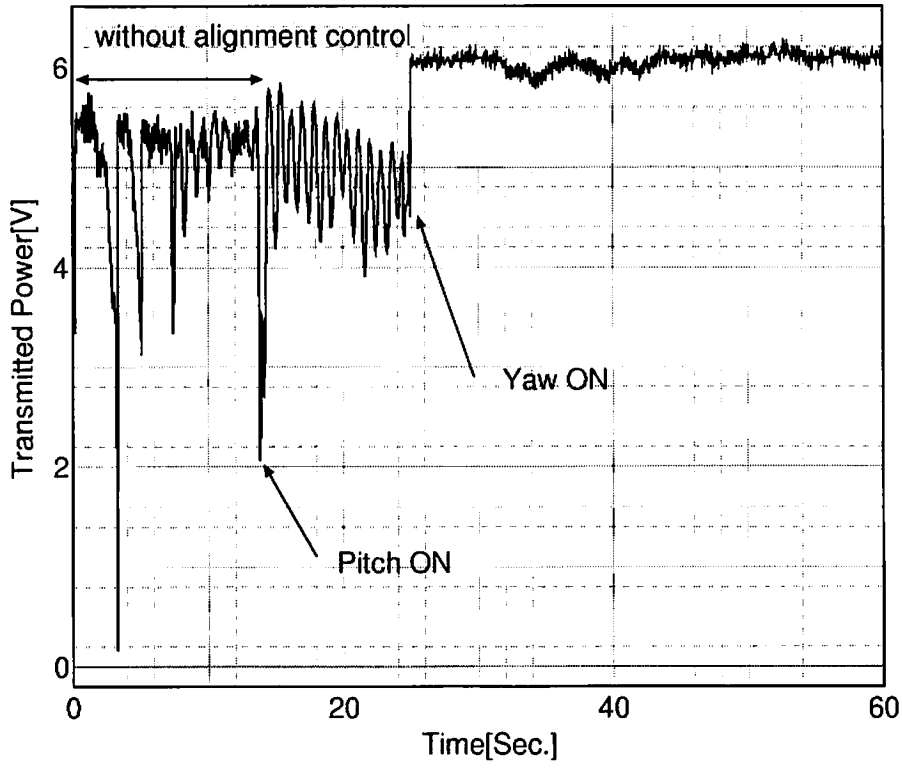

Figure 5.26: Transmitted light with alignment control

Because any misalignment of the cavity axis with respect to the input beam direction causes the decrease of the transmitted light power of Fabry-Perot cavity. The transmitted light power is the one of the quantities which shows the performance of the system. The

behavior of the transmitted light power for the interval in which the servos were switched on is shown in Fig.5.26. The Fabry-Perot cavity is still locked without the alignment control servo. However the transmitted light power is fluctuated largely. We set the unity gain frequency of the length control loop at about 10kHz and the gain at a few Hz was so high that the error related to the length control was well suppressed. The mirror suspended by the suspension system, however, has the resonance of the pitch (vertical) motion at about 5Hz and the one of yaw (horizontal) motion at about 1Hz. The fluctuation is caused by the misalignment resulting from these resonances. Therefore the fluctuation is reduced with the alignment control. With the pitch control loop, the fluctuation caused by the pitch motion at 5Hz is reduced. No large fluctuation, except for one caused by the yaw motion at 1 Hz, is remained. Then the yaw control loop is switched on, The fluctuation at 1Hz is also reduced and the power of the transmitted light increases. This result shows that the alignment control system works well.

5.4.3 Transfer Function of the Servo

Calibration

As the case of the length control, we need to transform the error signal of the alignment control servo into the information of the misalignment. Accordingly, we measured the response of the tilt of the mirror to the driving voltage of the coil-magnet actuator. The setup for this calibration is shown in Fig.5.27. We arranged the optical lever with cheap semiconductor laser and quadrant photodetector. As shown in this figure, we can obtain pitch and yaw motion of the mirror from the difference in between each sum of two segments. Applying the signal to the coil-magnet actuator, the response can be measured. The result of pitch motion is shown in Fig.5.28. Solid line is fitted line with the function as

$$\propto \frac{1}{\sqrt{(f^2 - f_0^2)^2 + \left(\frac{f f_0}{Q}\right)^2}}. \tag{5.16}$$

We can see that the response has the resonance around 5Hz and its Q-value is about 20. In the case of yaw motion, we obtained the result that the response has the resonance around 1Hz and its Q-value is about 5.

Servo Design and Openloop Transfer Function of the Servo

Alignment control has two main purpose. One is the suppression of the mirror tilt caused by the drift of stack attributed to the change of temperature. The other is suppression of the mirror fluctuation caused by the resonance of the pendulum. Though the change of temperature has a long term period, the resonance frequency of the pendulum is around a few Hz. Therefore we design that the unity frequency of this servo is around a few ten Hz.

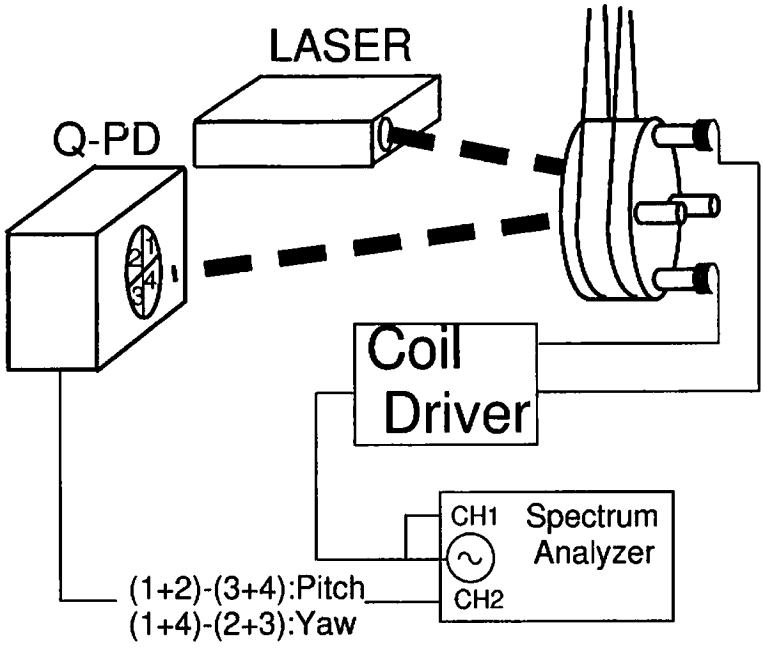

Figure 5.27: Setup for calibration with optical lever

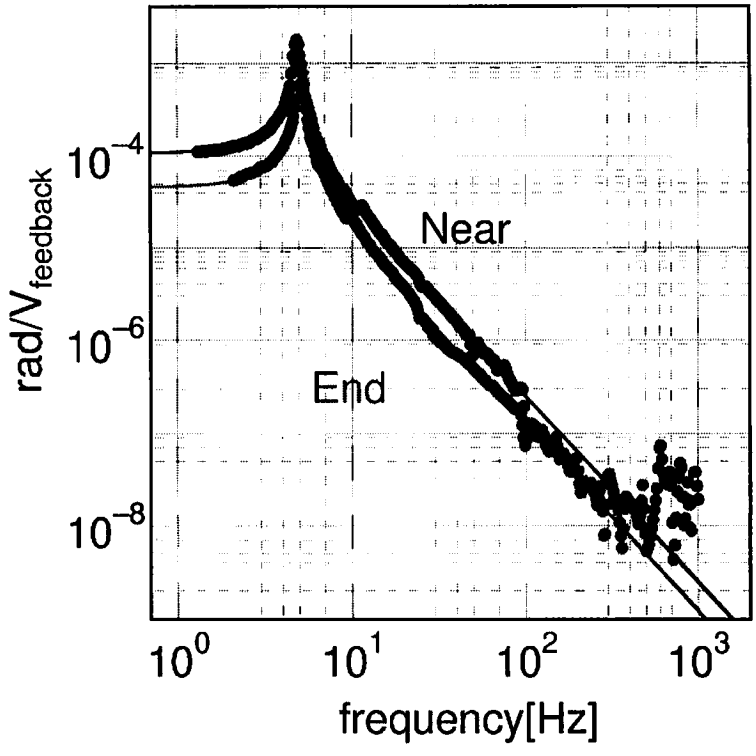

Figure 5.28: The results of calibration for the pitch motion of mirrors

To realize the stable operation of the servo, the sufficient phase margin at UGF is required. As the phase delays 180 degree in the higher frequency region than the resonance frequency of the pendulum, the electrical filter must advance the phase around UGF to obtain the sufficient phase margin. Therefore we design the filter shown in Fig.5.29 and insert it in the alignment control loop.

The openloop transfer function of the alignment control is measured as Fig.5.30. Solid line is fitted line with the calculated openloop transfer function. Though the unity gain frequencies vary, we can control them with adjustment of electrical filter gain. In addition, though the openloop gain around 1Hz differ between pitch and yaw, This is because the responses of the actuator are different between them. We can control them also with adjustment of electrical filter gain.

5.4.4 Noise Spectrum of Alignment Control

Suppression of the Fluctuation of the Mirror

Fig.5.31 shows the power spectrum of the error signal for pitch control loop of the front mirror. The value of the vertical axis is the angle of the fluctuation converted from the error signal. Without the alignment control, the spectrum has the sharp peak around 5Hz. In the region between 0.1Hz and 30Hz, the rms deviation of the fluctuation is determined by this peak and its value is 3.5×10^{-6}rad. With the control of which the unity gain frequency is set around 10Hz, we find that the peak is well suppressed. The rms deviation is 3.6×10^{-7}rad and satisfies the requirement.

The other fluctuations are similarly suppressed. The rms deviations of them also satisfy the requirement.

Effect of the Fluctuation of the Mirror

In order to detect the deviation between the input beam axis and the cavity axis, Wave Front Sensing is employed. The deviation is caused by two reasons. One is the fluctuation of the input beam axis (beam jitter). The other is the tilt of the mirror. In this section, The effect of the latter is considered. The calibrated power spectrum of the error signal with Wave Front Sensing is compared with that with the optical lever. The result for the pitch motion of the front mirror is shown in Fig.5.32. Though they are separated under 4Hz because of the coupling the WFS signal of yaw motion, we can see that both these spectrums overlap each other around the resonance frequency. The overlap of these spectrums means that these spectrum shows the fluctuation of the front mirror. We mention later about the separation above 20Hz.

Effect of Frequency Noise and Detector Noise

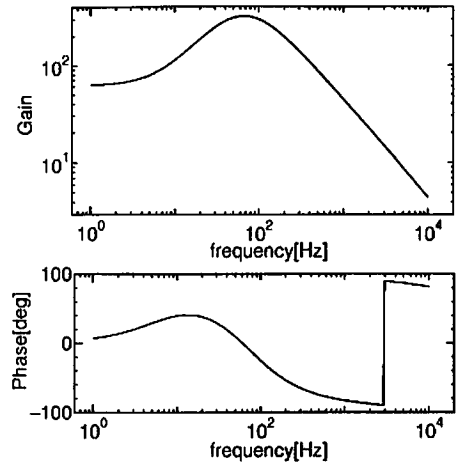

Figure 5.29: Transfer function of the electrical filter for the alignment control

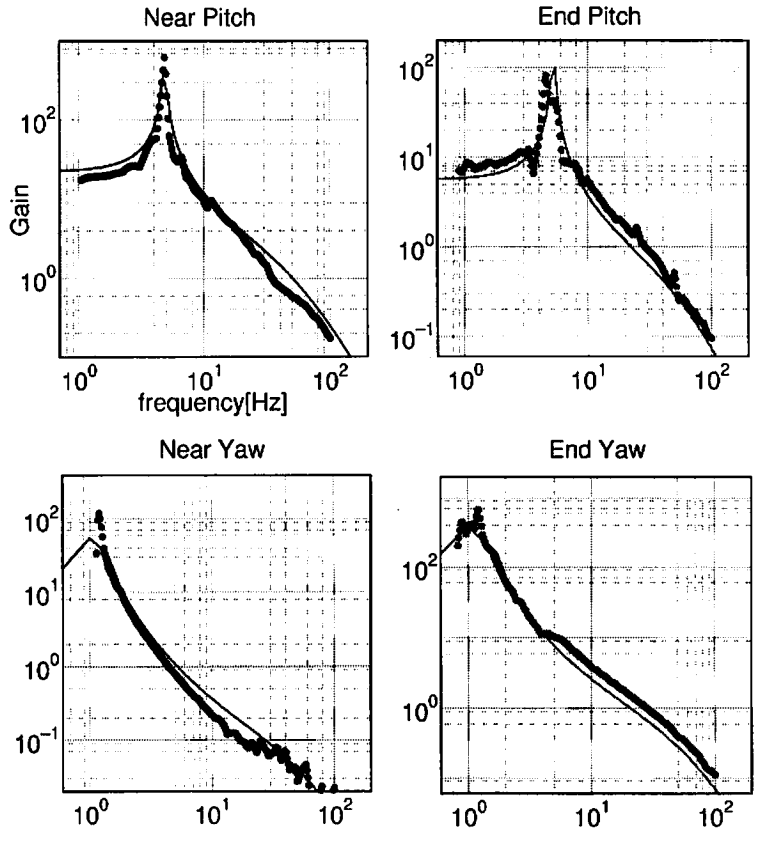

Figure 5.30: Openloop transfer function of the alignment control

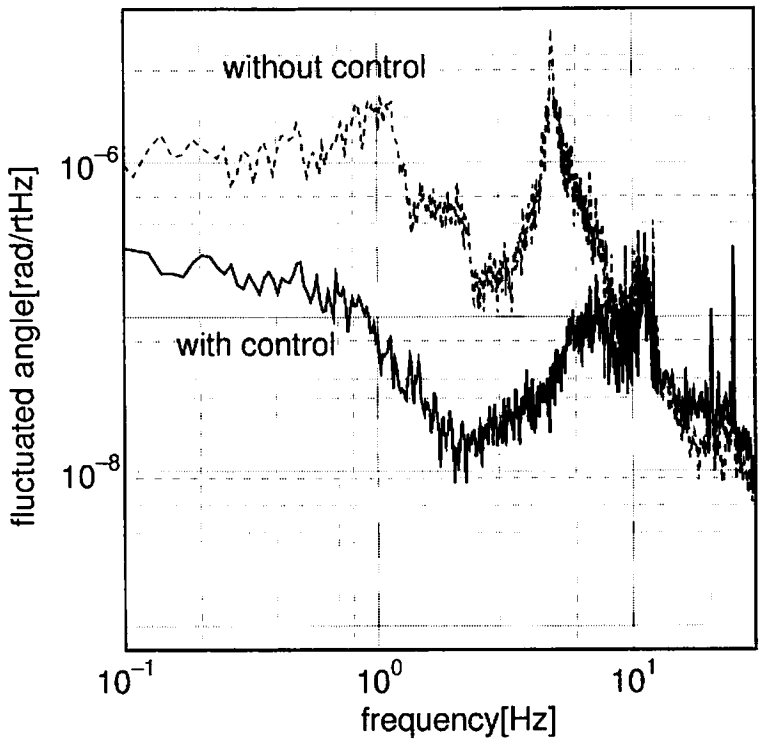

Figure 5.31: Estimated fluctuated angle of the mirror with/without alignment control

The reflected light from the cavity includes the information for the length control. The deviation from the resonance is suppressed by the gain of the length control servo. However a small amount of the deviation remains in the light. It becomes noise for the signal which is detected with Wave Front Sensing. Introducing the reflected light to the center of the quadrant photo detector, the contribution of this noise is equivalent to each segment of the photo detector. Therefore taking the difference between the signals of two segments, the effect of this noise reduces moreover. Applying the sine wave to the laser frequency control loop, we raised calibration peak in the spectrum and estimated the effect of this noise. The result is shown in Fig.5.33. We can see that the contribution of this noise dominate the spectrum of the error signal with Wave Front Sensing above 50Hz. [3] In the frequency region, the deviation from the resonance is caused by the laser frequency noise. Therefore the error signal of the Wave Front Sensing is limited by the laser frequency noise in this region. Since we will use the light source which is more stabilized in frequency in TAMA

[3]Though there is a small difference between the spectrums, it is caused by the deviation of the beam centering to the quadrant photo detector.

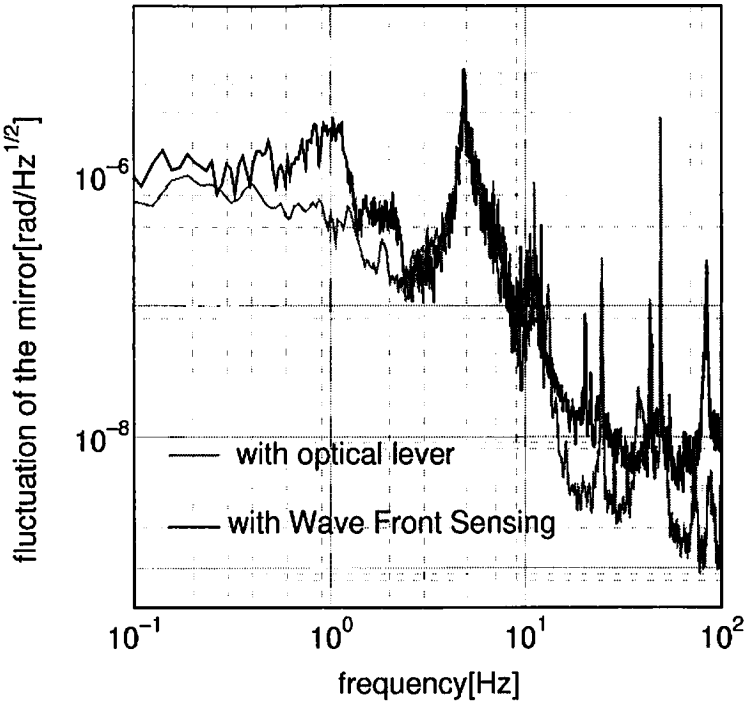

Figure 5.32: Effect of the fluctuation of the front mirror (pitch motion)

project[33], the effect of this noise level will reduce.

Next the effect of the detector itself is considered. In order to estimate it, we measured the power spectrum of the noise of the quadrant detector when the detector is covered. The calibrated result is also shown in Fig.5.33. We can see that the level of the detector noise contribution is almost just below that of the frequency noise contribution. In other words, using the laser source which is more stabilized in frequency, the contribution of the detector noise becomes the serious problem. In this case, we need to increase the signal of Wave Front Sensing. This is attained to some degree by an increase in light power and modulation index and so on. We will mention about this later.

Effect of Other Source

Now, we found that the cause which limit the power spectrum detected with the Wave Front Sensing as

- $\sim$ 20Hz: the fluctuation of the mirror

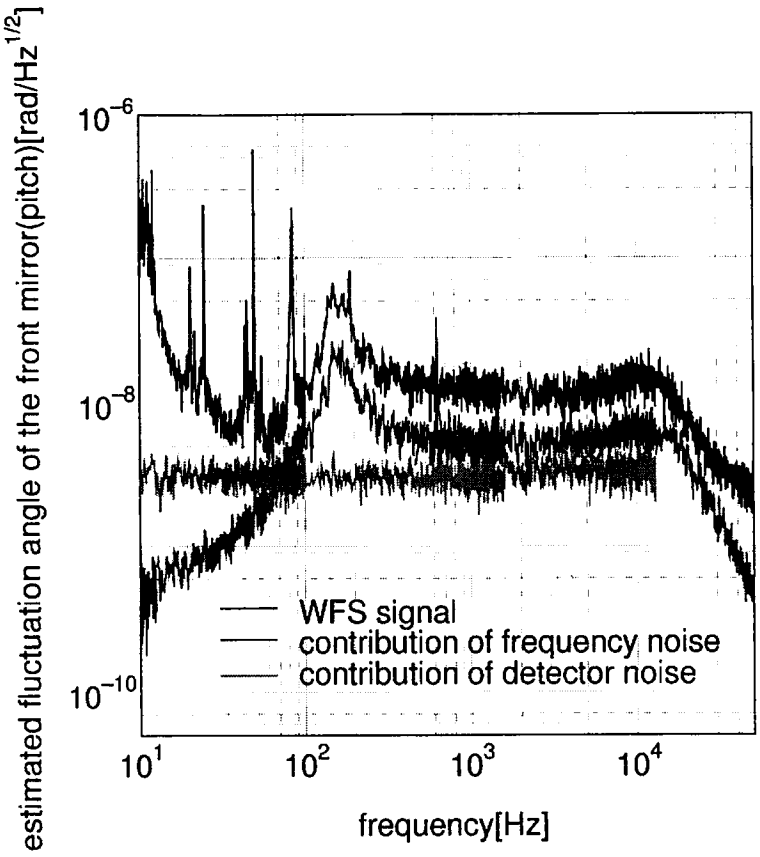

Figure 5.33: Effect of the frequency noise and detector noise

- 50Hz $\sim$: the laser frequency noise

Though we can't conclude the cause clearly in the frequency region 20Hz $\sim$ 50Hz, It is thought that the effects of the vibration generated by the rotary pump, air conditioner and so on are significant. Fig.5.34 is shown the state of affairs. Three power spectrums of the error signal detected with Wave Front Sensing (for pitch motion of front mirror) are shown in this figure. They are a spectrum measured in the situation that every machine is working, in the situation that the rotary pump around the input optics is turned off and in the situation that the rotary pumps and the air conditioners in the center room is turned off. We can see that the rotations of the pumps, air conditioners and so on affect the spectrum. Probably, the input beam axis is fluctuated directly and acoustically by the vibration generated by these elements. Though it is hard to remove these effect completely, the quiet vacuum system is necessary.

5.4.5 Influence to Length Control

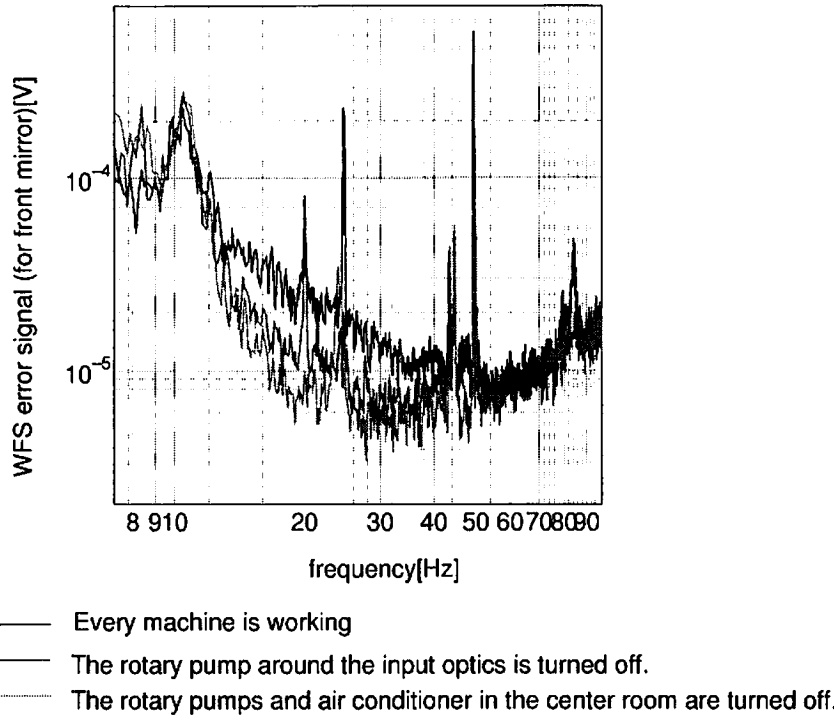

Figure 5.34: Effect of the vibration of the machines in the room

Here, we consider about the effect of the alignment control to the length control. In the observation band of the TAMA project (150Hz~450Hz), the error signal detected with the Wave Front Sensing is dominated by the laser frequency noise. Therefore the alignment control loop servo fluctuate the mirror in this frequency band. Coupling with the miscentering of the input beam to the mirror, this fluctuation influence the length control. The influence ΔL is approximated as

$$\Delta L \sim \Delta X_c \alpha, \tag{5.17}$$

where ΔX_c is the miscentering and α is the tilt of the mirror. Then, we estimated this influence from the feedback signal of the alignment control. we assumed $\Delta X_c = 1$mm. The result is shown in Fig.5.36. We can see that the estimated influence is $4 \times 10^{-15}[\mathrm{m}/\sqrt{\mathrm{Hz}}]$ at 300 Hz. While the target sensitivity of the TAMA is $5 \times 10^{-20}[\mathrm{m}/\sqrt{\mathrm{Hz}}]$ at 300 Hz. Therefore we need to suppress this influence by a factor of 10^5. This suppression will be realized by

- the improvement of the laser frequency stabilization

- the increase in the modulation index
- the increase in the light power
- the improvement of the electrical filter for alignment control servo

First, we note about the laser frequency stabilization. Since the purpose of this experiment is the development the control servo for 300-m long Fabry-Perot cavity, there is room for the improvement of the laser frequency stabilization. This improvement is realized by improvement the electrical filter for the laser frequency control and increase the control band using EOM for the actuator of frequency stabilization. At present, we are developing the frequency stabilized light source utilizing 10m Mode Cleaner cavity[33]. As mentioned in previous section, however, the detector noise is significant when the laser frequency is stabilized. In this case, the increase of the signal of Wave Front Sensing is nesessary.

As the Wave Front Sensing signal is the product of the carrier and sideband, it is proportional to $J_0(m)J_1(m)$. In the case that $m \ll 1$, the signal is proportional to m approximately. The measured modulation index is $m = 0.065$ in this experiment. It depends the EOM and the experimental setup. In TAMA project. we will set $m \sim 0.64$[34]. The signal level will increase about 10 times compared to this experiment with this setup.

We utilize the 700mW MISER as light source in this experiment and the light power introduced to the quadrant photo detector is about 1mW. In TAMA project, 10W MISER is utilized and 10mW light power is plan to be picked up for alignment control. Since the signal level is proportional to the light power, it will be increase about 10 times compared to this experiment.

Finally, the signal level increased about 100 times. Therefore signal to noise ratio is improved and the estimated noise level is shown in Fig.5.36 with dashed line. The target sensitivity in phase I of the TAMA project (without recycling) is also shown in this figure. As the noise level is above the target sensitivity, the improvement of the electrical filter for alignment control servo is necessary. Though the frequency band of alignment control is set with satisfaction at the requirement of misalignment. the noise must be suppressed by a factor of about 10^2. We will design the filter with these consideration.

5.4.6 Signal Separation

Optical Design

As mentioned in the previous chapter, the reflected light from the cavity includes the angular information of the front mirror and end mirror. In order to separate them, we adjust the Guoy phase propagation from the cavity to the quadrant photodetector. Actually, we select the focal length of lenses in the output optics chains and adjust the their position.

The arrangement of the output optics chain in this experiment is shown in Fig.5.37. The reflected light from the cavity is picked up with optical circulator after the telescope. Then it is divided to two optical path. One is introduced to the single photodetector and the signal for length control is detected with Pound-Drever method. The other is divided again, through the adequate lens sets and they are introduced to the quadrant photodetectors. Then the signal for the alignment control is detected with Wave Front Sensing method. The propagation is expressed as

$$\eta(z) = \arctan\left(\frac{\lambda z}{\pi w_0^2}\right). \tag{5.18}$$

It depends the beam waist radius w_0 and the distance from the waist z. The transition of the distance between the lenses L_{f1}, L_{f2}(shown in Fing5.37) change the radius of the beam waist and the distance to the waist in front and behind the lens. Therefore the propagation of the Guoy phase is adjusted by the adjustment of L_{f1}, L_{f2}.

Signal Separation

From the Eq. 4.48, the WFS signal corresponds to the front mirror tilt is

$$\propto \left(\frac{R-d}{w_0}\sin\eta_l - \frac{1}{\alpha_0}\cos\eta_l\right)\alpha_F. \tag{5.19}$$

The end mirror tilt α_E causes the lateral shift $R\alpha_E/w_0$. therefore the WFS signal is

$$\propto \left(\frac{R}{w_0}\sin\eta_l\right)\alpha_E. \tag{5.20}$$

Considering the case that $\alpha_F = \alpha_E = \alpha$, the separation ratio is expressed as

$$\frac{\text{Signal of End Mirror tilt}}{\text{Signal of Front Mirror tilt}} \propto \left(1 - \frac{d}{R} - \frac{w_0}{R\alpha_0\tan\eta}\right)^{-1}. \tag{5.21}$$

Measuring the response of the error signal to the feedback signal of the alignment control servo, we measured this separation ratio. The result is shown in Fig.5.38. The horizontal axis shows the estimated Guoy phase from the arrange of lens sets and the mode of cavity. The character of circle shows the measurement with the transition of L_{f1}. The character of square shows the measurement with the transition of L_{f2}. The solid line represents the calculation of the separation ratio. Since the estimation of the Guoy phase propagation includes the error, the whole shape of the measured values shifts from the calculation slightly. However we find the property of the result of the measurement tends to obey the calculation. Therefore we can separate the signal into the front mirror tilt and the end mirror tilt sufficiently with adjustment of the lens positions.

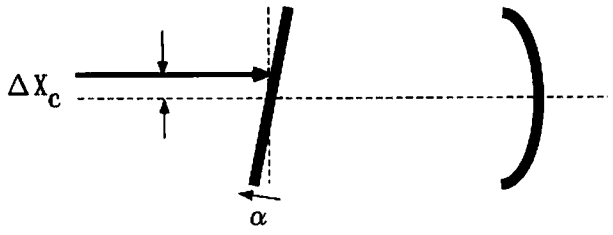

Figure 5.35: miscentering of the input beam to the misaligned cavity

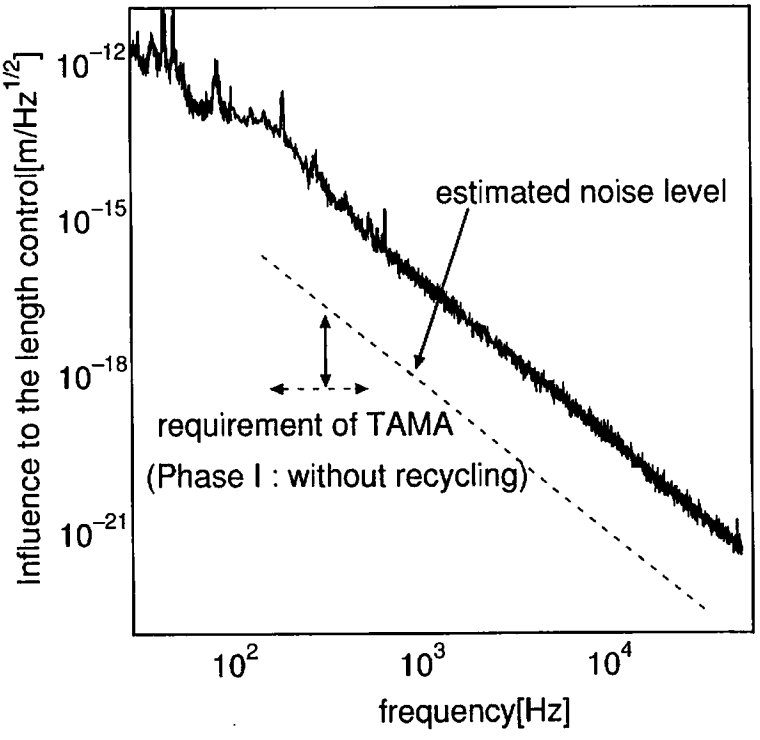

Figure 5.36: Influence of the alignment control to the length control

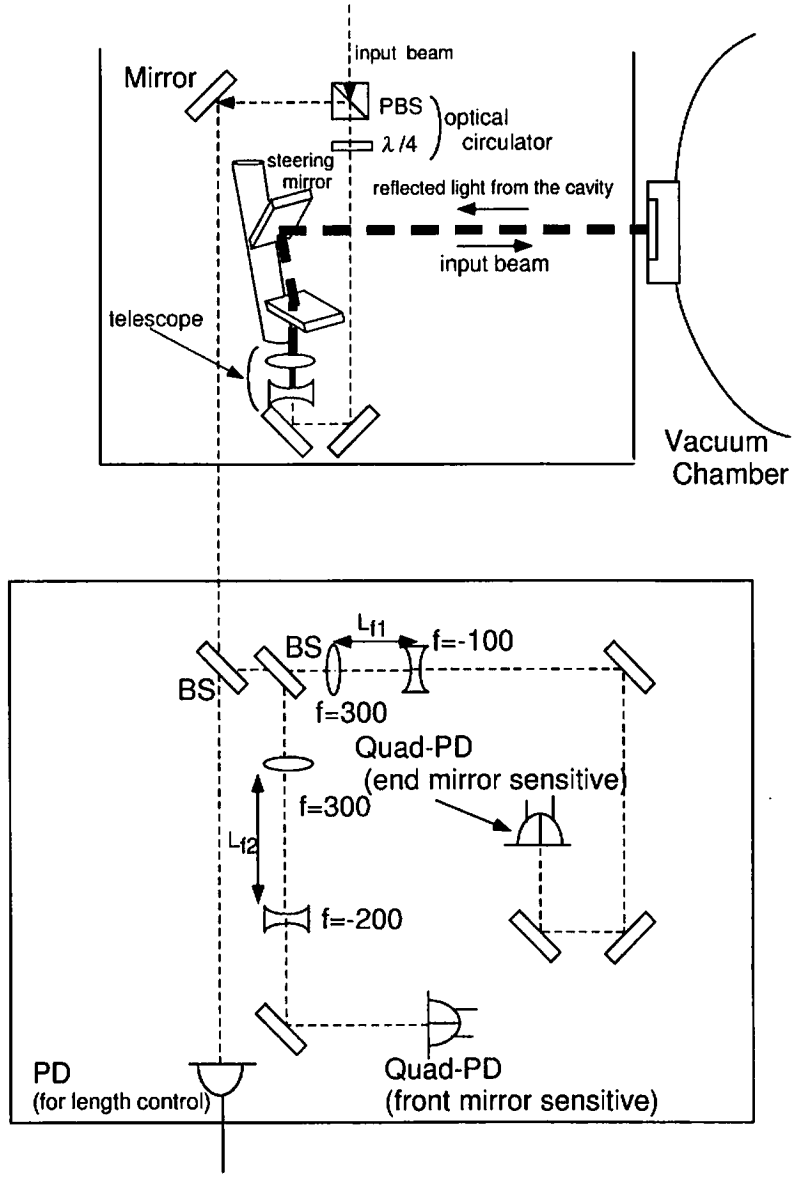

Figure 5.37: Output optics chain in this experiment

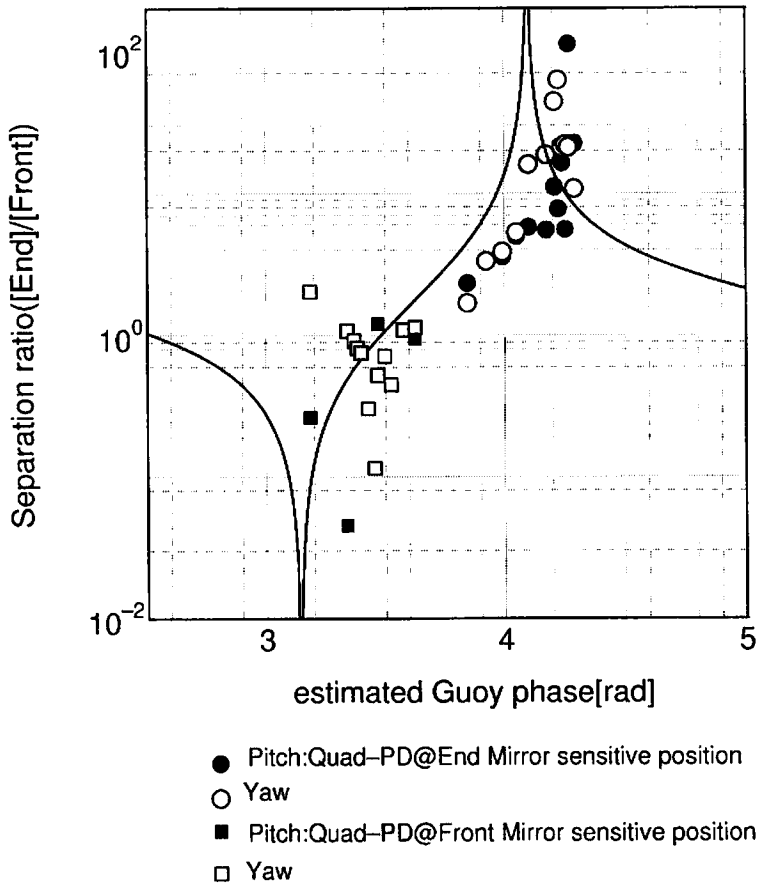

Figure 5.38: The separation ratio of signal detected with Wave Front Sensing technique

Chapter 6

Characterization of the 300-m Fabry-Perot Cavity

6.1 Measurement of Transmittance and Reflectivity

As mentioned in previous chapter, employing the alignment control with Wave Front Sensing, the stable operation of the 300m Fabry-Perot cavity is realized. This means that the behaviors of the transmitted and reflected light become stable. Accordingly, we measured the transmittance and the reflectivity of the cavity.

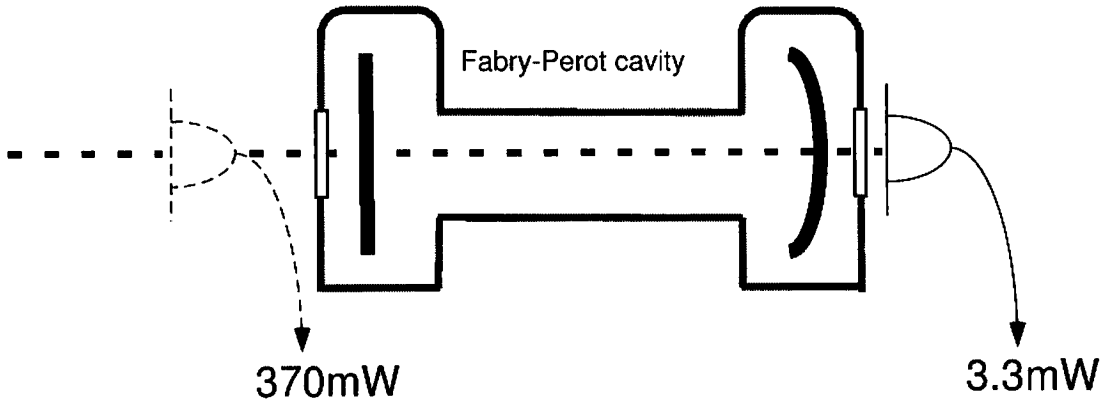

Figure 6.1: The measurement of the transmittance of the 300m Fabry-Perot cavity

Fig.6.1 shows the result of this measurement. With the transmittance of the optical windows of the vacuum chamber, which are 97% (front side) and 96% (end side) from measurement, in mind, we obtained that the transmittance of the cavity is 0.96%.

The reflectivity of the cavity is measured from the DC output of the photodetector for the length control. we compared the output on resonance with that apart from resonance.

The former is 853mV and the latter is 993mV. From this result, the reflectivity of the cavity is 86%. If the mirrors are lossless and have designed reflectivity and transmittance, the cavity reflectivity and transmittance are calculated as 96.7% and 3.26%. This difference is thought to be caused by the losses but it is not clear. We will discuss about this in next section.

6.2 Measurement of Finesse

6.2.1 Setup

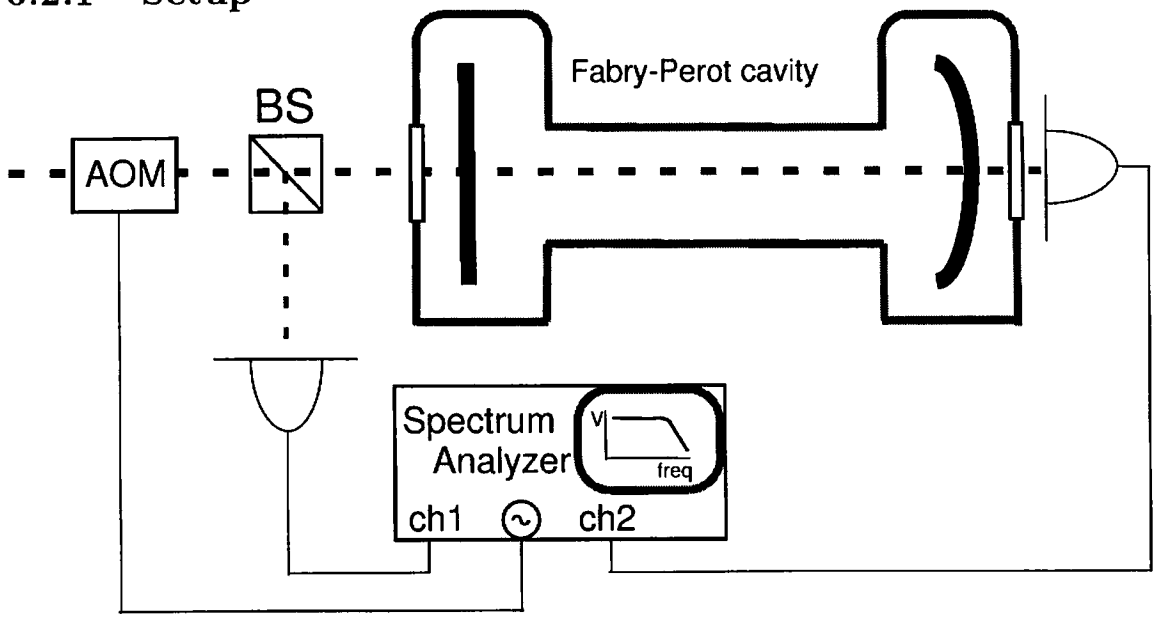

Figure 6.2: The setup for the measurement of the finesse of the 300m Fabry-Perot cavity

There are some methods to measure finesse of Fabry-Perot cavity. In this experiment, we measured the cavity response with modulated light in amplitude. The setup is shown in Fig.6.2. The light is modulated in amplitude with AOM and illuminated the Fabry-Perot cavity. Then it is detected with photodetector in front and behind the cavity and the ratio between the modulation frequency components is measured. Sweeping the modulation frequency, we obtain the response of the cavity.

6.2.2 Result

On the occasion of transference of the transmitted light, the signal gain and phase are influenced by the electrical circuits. Therefore we need to correct the influence. The corrected result is shown in Fig.6.3. The fitting function is

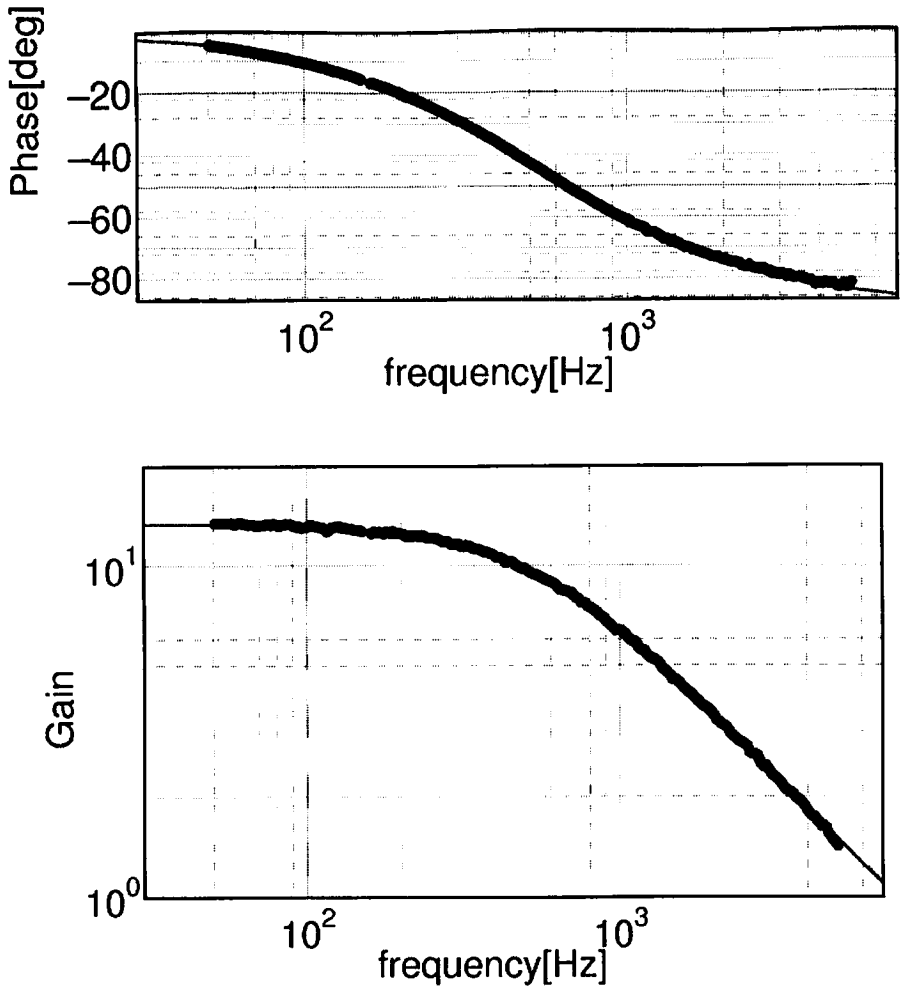

Figure 6.3: The result of the 300m Fabry-Perot cavity response

$$\text{Phase}: \quad \propto \quad \arctan\left(\frac{f}{f_c}\right) \tag{6.1}$$

$$\text{Gain}: \quad \propto \quad \left\{1+\left(\frac{f}{f_c}\right)^2\right\}^{-\frac{1}{2}}, \tag{6.2}$$

where f_c is the cut off frequency. We can see that it shapes one-pole filter. From fittings of the phase of some data, the cut off frequency is 546 ± 10Hz. The relation between the cut off frequency f_c and finesse $\mathcal{F}$ is

$$\mathcal{F} = \frac{c}{4lf_c}, \tag{6.3}$$

where l is the length of the cavity. Therefore the finesse of the cavity is 459 ± 19.

6.2.3 Discussion

As shown in the previous chapter, we measured the transmittance of the mirror itself and its value is $t_f = 1.41\%$ and $t_e = 0.0118\%$. Applying the measured value and assuming the lossless mirror, the finesse is

$$\mathcal{F} = \frac{\pi\sqrt{r_f r_e}}{1 - r_f r_e} = \frac{\pi\{(1-t_f^2)(1-t_e^2)\}^{\frac{1}{4}}}{1 - \{(1-t_f^2)(1-t_e^2)\}^{\frac{1}{2}}} \simeq 439. \tag{6.4}$$

This is near from the measured value. However the lossless mirror is unrealistic assumption. Under the assumption, for example, the transmittance and reflectivity of the cavity is

$$T_{cav} = \left(\frac{t_f t_e}{1 - r_f r_e}\right)^2 \simeq 3.27\% \tag{6.5}$$

$$R_{cav} = \left(\frac{r_f - r_e}{1 - r_f r_e}\right)^2 \simeq 96.7\%. \tag{6.6}$$

These value is different from the measured value $T_{cav-meas} \simeq 0.96\%$, $R_{cav-meas} \simeq 86\%$. Actually, when the cavity is on resonance, there are many glitter points caused by the dusts and mirror coating defects on the surface of the mirror. These are thought to be loss. Then we take account of loss and we assume the transmittance of the mirror to be measured value. In this case, corresponding to $T_{cav} = 0.96\%$, we need 5000ppm for loss. This is also unrealistic value from the finesse of the cavity. The origins of this contradiction are thought to be mismatching of the modes, inhomogeneous of the transmittance, reflectivity and loss, and so on. The studies about the character of the high quality optics in the large scale cavity are in progress[36][37]. Though the contradiction is not clear, we can say that the mirrors are low loss and have almost designed quality.

6.3 Longterm Operation and Absolute Length Measurement

In TAMA project, we plan the longterm observation with 300m recycled Fabry-Perot-Michelson interferometer. At that time, the influence of the drift which has longterm period (> 1hour) thought to be severe. Therefore an amount of the drift is need to be measured. Since the longterm operation of the 300m Fabry-Perot cavity is available with the alignment control, we demonstrated the absolute length measurement of this cavity with a new method using additional modulation in phase[25][35] and succeed to measure the amount of the drift for several days. This method requires the phase modulation

sidebands which are resonant in the cavity when the carrier is resonant and is based on determination of a free spectral range (FSR) of the cavity from the frequency difference between a carrier and sidebands. In this section, we will mention the principle of this sideband locking method, the experimental setup and the result.

6.3.1 Principle of the Sideband Locking Method

The cavity is locked on resonance with length control. In other words, the carrier frequency is adjusted to the n-th order resonance of the cavity (n:integer number). Then we consider the additional modulation in phase. As shown in Eq.4.35, the modulated electrical field is expressed as

$$\begin{aligned} & E_0 \exp j(\omega_0 t + m' \sin \omega_{m'} t) \\ = \; & E_0 \sum_{n=-\infty}^{\infty} J_n(m') \exp j(\omega + \omega_{m'})t \\ \simeq \; & E_0 \left[J_0(m') \exp j\omega t + J_1(m') \left\{ \exp j(\omega + \omega_{m'})t - \exp j(\omega - \omega_{m'})t \right\} \right], \end{aligned} \tag{6.7}$$

where additional modulation index is m' and its angular frequency is $\omega_{m'}$. The two dominant sideband components are adjusted to the (n+m')-th and (n-m')-th order resonances (m':integer number also). In this case, the modulation frequency ($\omega_{m'}/2\pi$) corresponds to m' times the FSR of the cavity. When the cavity reflected light signal is demodulated at the frequency of this modulation, the resulting signal has the form (its derivation is shown in Appendix B):

$$16E_0^2 J_0(m')J_1(m') \frac{r_e^2 t_f^4}{(1 - r_1 r_2)^4} \left(\frac{L}{c}\right)^2 \Delta\omega\Delta\omega_{m'} \simeq 8E_0^2 m' \frac{t_f^4}{(1 - r_f r_e)^2} \mathcal{F}^2 \frac{\Delta\nu\Delta\nu_m}{\nu_{FSR}^2}. \tag{6.8}$$

The demodulated signal depends on both the difference of the carrier frequency from the n-th resonance ($\Delta\nu$) and the difference of the sideband frequency from $m\times$FSR ($\Delta\nu_m$). Under the condition that the carrier frequency ν is precisely locked at the center of the cavity resonance ($\Delta\nu = 0$), the reflected light contains no signals for locking the sideband frequency. In order to obtain the sideband locking signal, we intentionally apply a deviation by modulating the carrier frequency around the resonance center by a small amount:

$$\Delta\nu = \Delta\nu_n \sin \omega_n t \quad \left(\Delta\nu_n \ll \frac{\nu_{\mathrm{FSR}}}{\mathcal{F}} \right). \tag{6.9}$$

The demodulated signal is then demodulated with ω_n to obtain a signal which is proportional to $\Delta\nu_m$ and can be used for the sideband locking.

6.3.2 Setup

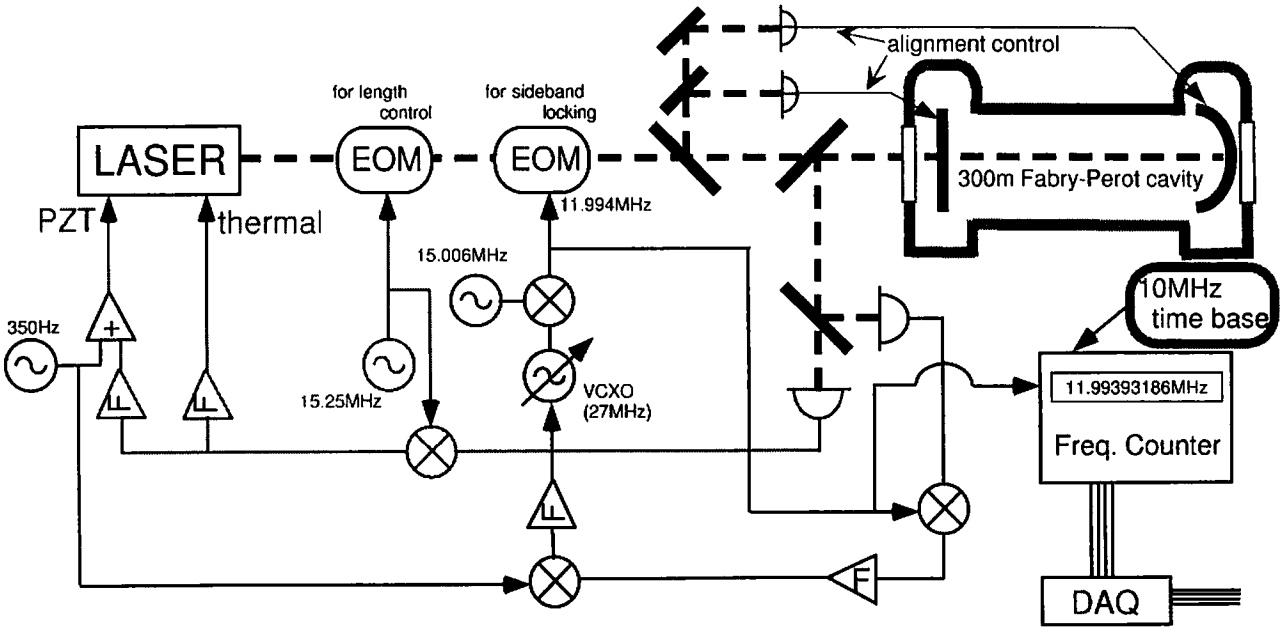

Figure 6.4: The setup for the absolute length measurement

The setup for the absolute length measurement is shown in Fig.6.4. The laser light is modulated double in phase and introduced to the cavity. The modulation frequencies of the first EOM is 15.25MHz. This is utilized for the length control and the alignment control. However the signal of the length control is fed back to the thermal actuator of the laser in the low frequency region. Therefore the signal is not fed back to the cavity length itself in this experiment.

The sideband locking is implemented with simultaneous phase modulation by the second EOM at about 12MHz($= \nu_{m'}$) and with frequency modulation of the laser at 350Hz($= \nu_n$). The signal, which was doubly demodulated with the modulation frequencies ($\nu_{m'}$ and ν_n), was fed back to the modulation frequency, $\nu_{m'}$, to lock the sideband frequencies, $\nu \pm \nu_{m'}$, at the center of the cavity resonance. A voltage-controlled crystal oscillator (VCXO) was used for this purpose.

When both the carrier (ν) and the sidebands ($\nu \pm \nu_{m'}$) are locked to the cavity resonances, the FSR of the cavity can be obtained from the sideband modulation frequency ($\nu_{m'}$). The oscillation frequency of the VCXO was therefore measured by a frequency counter which was synchronized with a stable timebase to realize accurate frequency counting. We adopted a commercially available GPS-locked oscillator (HP58503, Hewlett-Packard Co.), with a

frequency accuracy of better than 10^{-11} for $\geq$0.1s, as the accurate timebase. The counted frequency, with a gate time of 25s, was recorded every 30 seconds through a network. Using a sideband modulation frequency of about 11.994MHz and for a cavity length which is known to be (299.940$\pm$0.005)m from a survey, we get $m=\nu_{m'}/\nu_{FSR}=23.9998\pm0.0004$. Since m should be an integer, we conclude $m=24$. The conversion from $\nu_{m'}$ to the cavity length (L) is expressed as,

$$L = 24\frac{c}{2\nu_{m'}}. \tag{6.10}$$

Other signals of the system (laser intensity, alignment signals, and feedback signals to the laser) as well as environment signals (temperature, barometric pressure, humidity, and weather) were monitored through a network and by other methods.

6.3.3 Result

- **Longterm Operation**

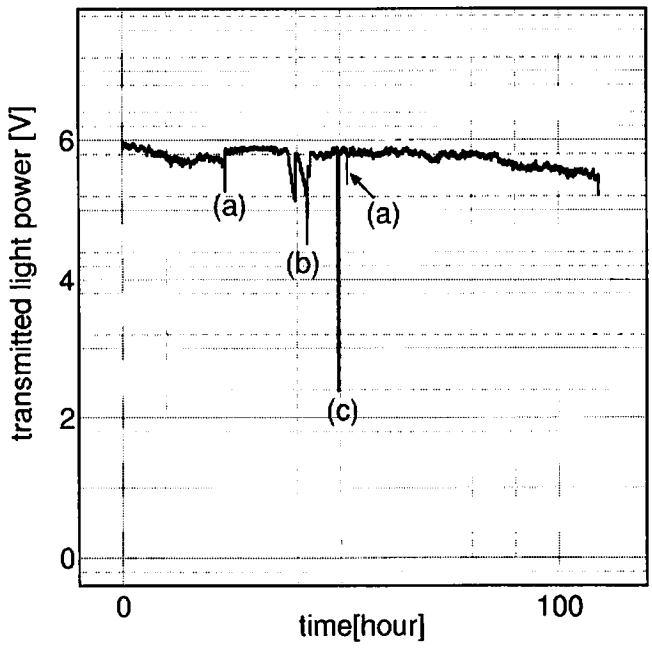

Figure 6.5: Transmitted light in longterm operation of 300m Fabry-Perot cavity

We observed the absolute length of the 300-m Fabry-Perot cavity continuously for 4.5 days from 18 March 1998 to 23 March 1998. The FP cavity lock was very stable with this alignment control in this observation and was held the resonant condition

for these days. The behavior of the power of the transmitted light in this longterm operation is shown in Fig.6.5. Several peaks are shown in this figure. They are classified into three categories: (a)Without the manual adjustments for a long time, the drift of the input beam axis was observed. These peaks correspond to the case when we adjusted the drift manually. (b)In the center room where the front mirror chamber and our operation system are placed, the other chamber are also placed and they were in preparation at that time. In the interval of this peak, the work preparing the suspension for the beam splitter was done close to our chamber. It caused the drift of the beam axis and the drift was adjusted manually. (c)At this time the FP cavity was locked on TEM_{10} mode accidentally.

Except for these peaks, the transmitted power was stable. Generally, the resonance of the FP cavity was not disrupted except that the servo is switch off. Such a long term operation of the long baseline FP cavity had never been done and we succeeded in the operation for the first time.

- **Observation of the Absolute Length of the 300m cavity**

  Figures 6.6(a) to (c) show the data obtained in this observation. Figure 6.6(a) is the frequency change of the VCXO, with an offset frequency (11.993900MHz) subtracted. The corresponding absolute length of the cavity from Eq.6.10 is shown on the right axis; the sideband modulation frequency of 11.993940MHz corresponds to 299.943930m in absolute length and a 1-Hz change in frequency is equivalent to about 25-μm change in length. Figure 6.6(b) is the feedback signal to the laser in terms of frequency. Since the relation between the change of the laser frequency and that of cavity length can be expressed as,

$$\frac{\delta\nu}{\nu} = \frac{\delta L}{L}, \tag{6.11}$$

  the corresponding length change is indicated on the right axis (offset frequency or length is arbitrary). Figure 6.6(c) shows the temperatures monitored on an optical table near the laser, and at the input and end chambers of the cavity vacuum envelope.

  From the absolute length data shown in Fig.6.6(a), two striking characteristics are apparent: spiky changes which occurred 12$\sim$14 times a day with about 20-μm changes in length; and a slow variation over several days which bottomed around 20 March. We concluded that the spiky changes originated from real changes in cavity length. Since the frequency of the laser is locked to the 300-m cavity, the feedback signal shown in Fig.6.6(b) is affected both by changes in the cavity length and by drift of the laser frequency itself. The spiky changes that appear in Fig.6.6(a) and 6.6(b) with the same displacement but are not seen in Fig.6.6(c) are thus considered to be

real changes in cavity length. The diurnal changes seen both in Fig.6.6(b) and 6.6(c) ('optical table') apparently originated from the drift of the laser frequency due to room temperature.

We also concluded that the spiky changes originated from regional ground strain changes rather than from local displacement of the mirrors. This is because we found no spiky feature in the tilt of the mirror suspension system, judging from the alignment signals, and a strong correlation between the spikes and the pumping of groundwater near the NAO campus (the pumping well is located about 200m from the instrument) [1]. Figure 6.7(a) is the magnified view of Fig. 6.6(a). The shape of the spikes shows a rapid rise (shrink in length) within 30 minutes and a relaxation (expansion in length) with a time constant of 1 to 2 hours. Figure 6.7(b) shows the correlation between these spikes and the pumping status; the ground shrinks when the pump is on and it relaxes back after the pump is turned off. This is intuitively consistent with the response of the earth to the pumping of groundwater. It should be also noted that the amount of strain caused by the pumping of groundwater was at a reasonable level according to the reference [38]. Location of the 300-m Fabry-Perot cavity and the pumping well is shown in Fig.5.2.

As for the slow variation of the absolute length in Fig. 6.6(a), we believe it is dominated by local displacement of the mirrors due to tilt and horizontal drift of the isolation stacks caused by ambient temperature fluctuations. After performing the absolute length experiment, we measured the response of tilt/horizontal drift of the isolation stacks to the ambient temperature; it was found that typical temperature variations (3 degrees peak-peak) in the chambers could produce a mirror displacement of 50μm peak-peak, the level observed in the absolute length measurement. Moreover, the recorded temperature variations in the chambers during the absolute length measurement (Fig.6.6(c)) showed a similar trend (a peak on the 20th and a rather steep slope afterward) to the slow variation of the absolute length. It should be noted that this slow variation completely dominates tidal or semi-diurnal/diurnal variations, which we had expected would be dominant and were interested in prior to the experiment.

[1] Groundwater is utilized by a hospital located in the vicinity of NAO. The groundwater pump is activated automatically when the water reservoir becomes near empty; typically 11 to 14 times in the daytime. The depth of the well is about 90m, and about 15m^3 of water is pumped up from 60-m depth for every pumping cycle.

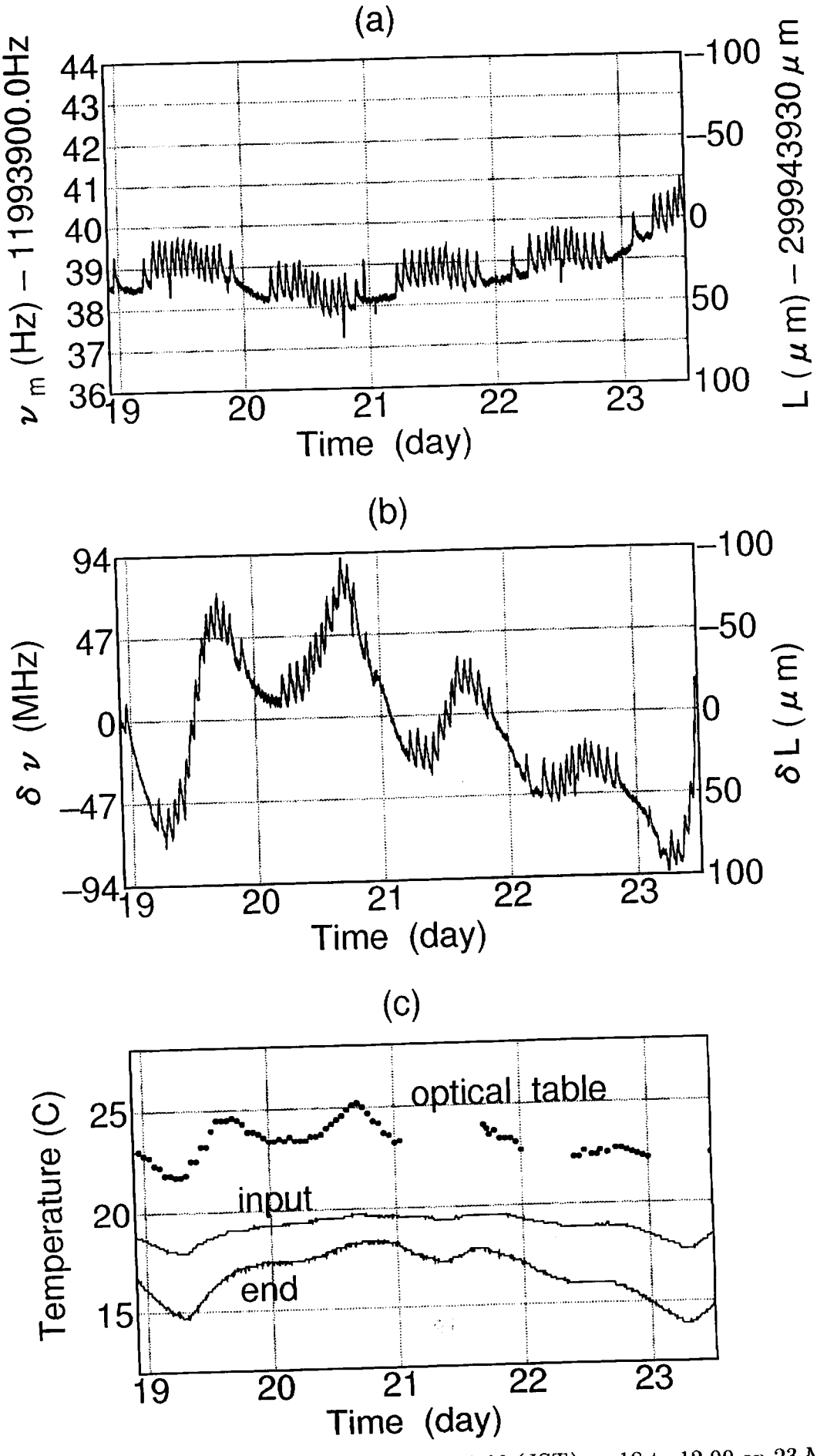

Figure 6.6: Observed data in the period from 22:00 (JST) on 18 to 12:00 on 23 March 1998

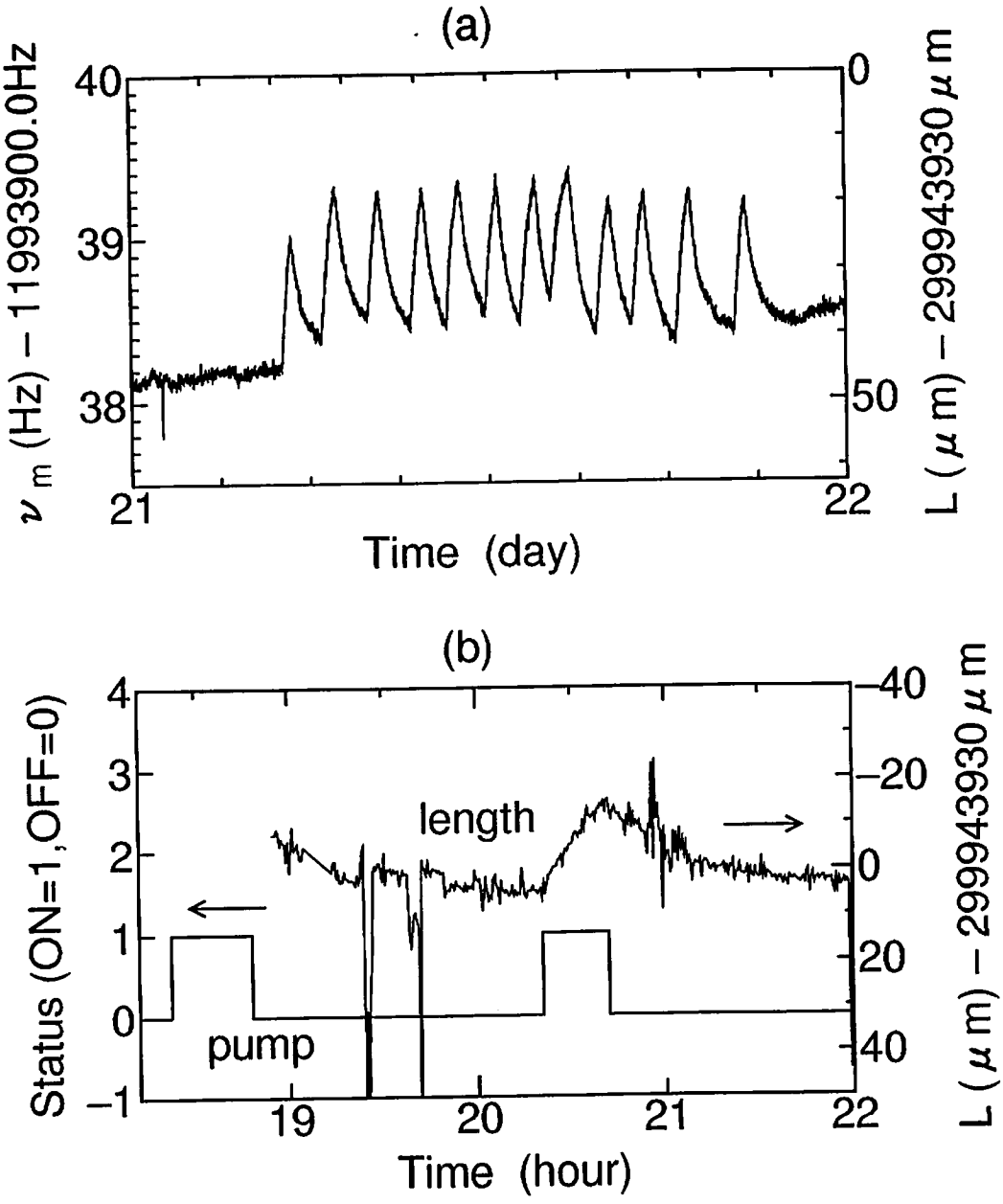

Figure 6.7: Magnified view of spiky changes in Fig.6.6(a) and Synchronous observation of absolute length (length) and pumping status (pump)

Chapter 7

Conclusion

We have demonstrated the control of the alignment and the length of the 300-m Fabry-Perot cavity by using one of the TAMA300 arm cavities. With an automatic alignment control system, the cavity was kept locked to its resonance very stably over 5 days. Angular fluctuations of the mirrors, which were on the order of micro radians, were reduced below several hundred nano radians by the control loop. The dependence of the alignment error signal on the Guoy phase was measured to be good agreement with the theory. We have measured the noise performance of the alignment sensing system. In this experiment, the low-power laser with the poor frequency stabilization made the signal-to-noise ratio worse than required. Also, the feedback filter was not optimally designed to minimize the contamination of the length fluctuation by the alignment servo. However, we believe that we will be able to satisfy the requirements for TAMA300 detector with the proper design of the servo filter and the 10W high power laser with the frequency stabilization.

7.1 Length Control

As the mirrors which compose the cavity is suspended by wires, they are fluctuated more than wavelength of the light at the resonance frequency of the pendulum. From the behavior of the reflected light without length control (*e.g.* the number of the passage of the resonance within the certain interval, the effect of the Doppler shift caused by the mirror motion and so on), we estimated the amplitude of the fluctuation to be a few μm. Therefore the cavity can't be held resonant condition without length control. In this experiment, we detected the deviation from the resonance of the cavity with Pound-Drever method. The signal was fed back to the coil-magnet actuator attached to the mirror and the PZT actuator of the LASER and we controlled the cavity length and laser frequency. Consequently, the cavity was held resonant condition. From the calibrated power spectrum of the error signal, we can see that it is limited by

- $\sim$ 10Hz:the influence of the ground vibration.
- 10Hz $\sim$:the noise of the laser frequency

and the servo works as its design.

The transmitted light was fluctuated at the resonance frequency of pitch and yaw motion of the suspended mirrors. The amplitude of the fluctuation was tens percent of maximum transmitted power. This means the angular fluctuation of the mirror (a few $\mu\text{rad}_{\text{rms}}$) affects the resonance condition of the cavity. Though the reduction of this influence with the passive vibration isolation system is desired, such systems are hard to develop. Therefore the reduction with automatic alignment control system is required.

7.2 Alignment Control

Under some conditions, the requirement for the misalignment is estimated as 5×10^{-7}rad in TAMA project. In order to satisfy this requirement, the automatic alignment control system was demonstrated in this experiment. The signal of misalignment was detected with Wave Front Sensing system and it was fed back to the coil-magnet actuator. Consequently, the requirement was satisfied and the behavior of the transmitted light became stable. The rms fluctuation of pitch motion of the front mirror (0.1Hz$\sim$30Hz), for example, was reduced below 3.7×10^{-7}rad.

With the setup in this experiment, the signal detected with Wave Front Sensing technique was limited by

- $\sim$20Hz:the fluctuation of the mirror
- 20Hz$\sim$50Hz:the influence of the vibration of the pumps, air conditioners and so on
- 50Hz$\sim$:the laser frequency noise or the detector noise

Especially, in the observation band of TAMA project, the influence of these noise to the cavity length is feared. In the case of TAMA interferometer, however, the signal to noise ratio of Wave Front Sensing is improved by the increase of the light power and modulation index, the employment of the high frequency stabilized light source, the preparation of the quiet environment, and the adequate improvement of the alignment control filter. Then this influence is thought to be reduced.

In order to confirm the behavior of Wave Front Sensing, we measured the separation ratio of the signal between the front mirror tilt and the end mirror tilt. Consequently, the separation ratio changed with the Guoy phase propagation from the cavity to the quadrant detector. From this result, we can see that it is possible to obtain the separation ratio of 10:1 with adjustment of the lenses position in the output optics chains.

7.3 Properties of the 300-m Fabry-Perot cavity

The mirrors for the large scale interferometer have some features in design. They are large and monolithic optics which have high reflectivity and low loss. Though these features have been measured with mirror itself (for example, measurement of transmittance with amplitude modulated light), the measurements with the cavity have never been done. The stable operation of the cavity makes them possible. We measured finesse of the 300-m Fabry-Perot cavity from the response of the cavity. As a result, we obtained the value of 459 ± 19. It is near the designed value 516 and this shows that the reflectivities and losses of the mirrors are also near their design. Though the measured reflectivity and transmittance of the cavity and these results are in some contradiction, some unconfirmed value of the cavity still remain and there is room for study. We expect the progress of the study about the high quality optics for the large scale interferometer.

We observed the absolute length of the 300-m Fabry-Perot cavity in longterm period with novel method of FSR measurement utilizing sideband locking. In this observation, we realized longterm operation of the cavity. Operation time reached for several days and the cavity was held resonant condition stably. Such a longterm operation have never been done and this is the first case in the world. From the result of absolute length observation, we found that spiky changes which occurred $12 \sim 14$ times a day within 20μm changes in length. We conclude that they originate from the regional ground strain change which are caused by the pumping of the groundwater near the NAO campus. These results are significant for the discussion about the dynamicrange of the actuator.

7.4 Prospects in the future

The one-arm experiment is already finished and the experiment of Fabry-Perot-Michelson interferometer have progressed. The operation of Fabry-Perot-Michelson interferometer was succeeded[39]. Now the light source is going to be exchanged for 10W Laser developed by the SONY Co. This light is illuminated to the 10m Mode Cleaner cavity and the transmitted light is introduced to the interferometer. This exchange of the light source produce three advantage for the increase the signal to noise ratio of Wave Front Sensing. These are increase of the light power and modulation index and high frequency stabilized light. Therefore we will able to estimate the angular fluctuation of the mirrors in the observation band and discuss the influence of the alignment control to the cavity length realistically. Besides, the mode cleaned light make the estimation of the quality of the optics possible.

Hereafter, the development of the signal extraction scheme of Wave Front Sensing for complicated optical system (*e.g.* Recycled Fabry-Perot-Michelson interferometer) is significant [40].

Appendix A

Doppler Effect of Reflected Light from the Cavity

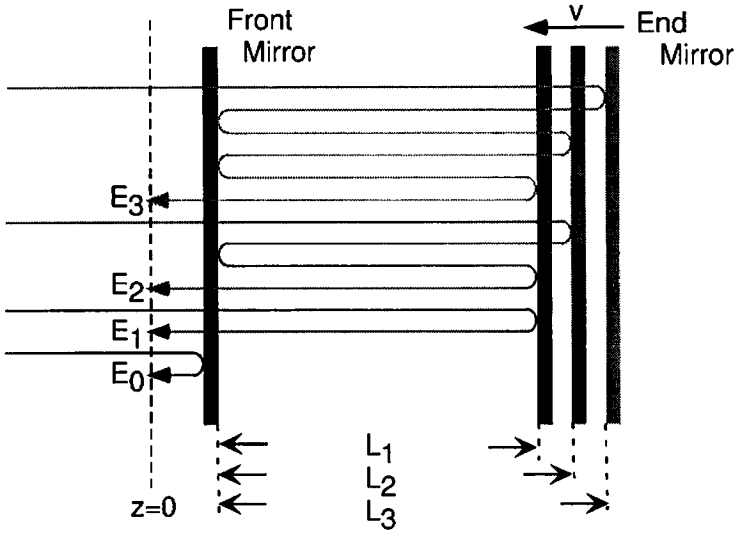

Figure A.1: frequency shifted field by Doppler effect in the simple case

Though the mirrors are isolated from the ground vibration with the stack, the pendulum and so on, they are not still completely. When the light reflects a moving mirror, its frequency is shifted by Doppler effect. Now we consider the Doppler effect to the reflected field. For simplicity, the front mirror is assumed to be fixed and only the end mirror to be moving with the velocity v(Fig.A.1). First, we consider the multi refection in this case and obtain the expression of the field at $z = 0$. The direct reflection at the front mirror is $r_f E_0$ where E_0 is amplitude of the input field. The field which leak out of the cavity after one time reflection at the end mirror E_1 is expressed as

$$E_1 = -t_f^2 r_e E_0 e^{-j(\omega_0 t_1 + \omega_1 t_1)},$$

where t_1 is the time interval L_1/c and ω_1 is the Doppler shifted frequency of the light. ω_1 is expressed as

$$\omega_1 = \frac{c+v}{c-v}\omega_0.$$

Therefore the field $E_1$is

$$E_1 = -t_f^2 r_e E_0 e^{j\frac{2L_1}{c-v}\omega_0}. \tag{A.1}$$

Next, we consider the field which leak out of the cavity after two time reflection at the end mirror E_2. It is

$$E_2 = -t_f^2 r_e (r_f r_e) E_0 e^{-j(\omega_0 t_2 + \omega_1 t_2 + \omega_1 t_1 + \omega_2 t_1)},$$

where t_2 is the time interval L_2/c and ω_2 is expressed as

$$\omega_2 = \frac{c+v}{c-v}\omega_1 = \frac{(c+v)^2}{(c-v)^2}\omega_0.$$

Since $L_2 = L_1 + v(t_1 + t_2)$, L_2 is

$$L_2 = \frac{c+v}{c-v}L_1.$$

From these expression, we can obtain

$$E_2 = -t_f^2 r_e (r_f r_e) E_0 \exp\left\{-j\left(4\frac{c+v}{(c-v)^2}L_1\omega_0\right)\right\}. \tag{A.2}$$

Similarly, E_n can be expressed as

$$E_n = -t_f^2 r_e (r_f r_e)^n E_0 \exp\left\{-j\left(2(n+1)\frac{(c+v)^n}{(c-v)^{n+1}}L_1\omega_0\right)\right\}. \tag{A.3}$$

Consequently, the field of the reflected light E_{ref} is

$$E_{ref} = \left[r_f - t_f^2 r_e^2 \sum_{n=0}^{\infty}(r_f r_e)^n \exp\left\{-j\left(2(n+1)\frac{(c+v)^n}{(c-v)^{n+1}}L_1\omega_0\right)\right\}\right] E_0. \tag{A.4}$$

For simplicity, we regard the double pendulum as a single one at the resonant frequency(Fig.A.2). In this case, the maximum velocity of the suspended object v_{max} is $v_{max} = \sqrt{2gh}$. We put that the amplitude of fluctuation is Δx. Then h is $h \sim \Delta x^2/l_p$. Therefore we assume that the velocity of the mirror is roughly

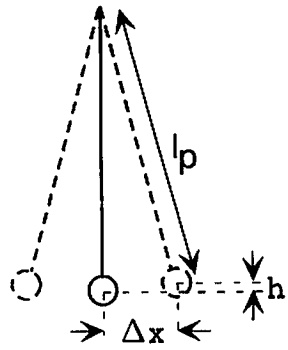

Figure A.2: the swaying single pendulum

$$v = \sqrt{\frac{2g}{l_p}}\Delta x.$$

From this and Eq.A.4, the reflectivity of the cavity is simulated and the result is shown in Fig.A.3. we use the parameter of the 300-m cavity.

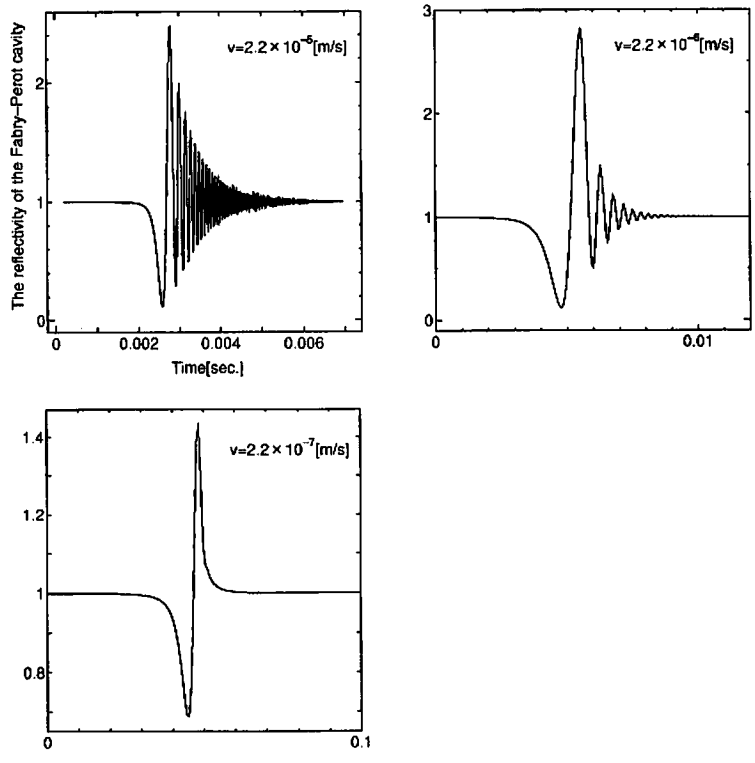

Figure A.3: the simulated reflectivity of the 300-m Fabry-Perot cavity

Comparing this result with Fig.5.16, we can estimate the amplitude of fluctuation $\Delta x \sim$ a few μm roughly.

Appendix B

Derivation of the Signal Expression of Sideband Locking

Here, we consider the derivation of the Eq.6.8. The field of input beam E_{in} is expressed as

$$E_{in} \simeq E_0 \left[J_0(m') e^{j\omega_0 t} + J_1(m') \left\{ e^{j(\omega_0+\omega_{m'})t} - e^{j(\omega_0-\omega_{m'})t} \right\} \right].$$

The reflected light is

$$E_{ref} = E_0 \left[r_c(\delta) J_0(m') e^{j\omega_0 t} + J_1(m') \left\{ r_c(\delta_+) e^{j(\omega_0+\omega_{m'})t} - r_c(\delta_-) e^{j(\omega_0-\omega_{m'})t} \right\} \right], \qquad \text{(B.1)}$$

where $r_c(\delta)$ is the cavity reflectivity when the cavity is not on resonance exactly by the deviation δ. As shown in chapter 4, the δ is

$$\delta = \frac{\Delta\omega L + \Delta L \omega_0}{c},$$

where L is the cavity length and ω_0 is the laser frequency. We assume $\delta L \sim 0$. Then $\delta \simeq \Delta\omega L/c$. While the $\delta_\pm$ is

$$\delta_\pm \simeq \frac{(\Delta\omega \pm \Delta\omega_m)L}{c}.$$

The reflectivity of the cavity $r_c(\delta)$ is

$$r_c(\delta) = \frac{r_f - r_e(1-P_f)e^{-2j\delta}}{1 - r_f r_e e^{-2j\delta}} \simeq \frac{r_f - r_e(1-P_f)}{1 - r_f r_e} + 2j \frac{r_e t_f^2}{(1 - r_f r_e)^2} \frac{L}{c} \Delta\omega \equiv r_{c0} + j a_\delta \Delta\omega. \qquad \text{(B.2)}$$

Therefore Eq.B.1 is

$$E_{ref} = E_0 e^{j\omega_0 t}\Big[J_0(m')(r_{c0} + ja_\delta\Delta\omega + J_1(m')\left\{(r_{c0} + ja_\delta\Delta(\omega+\omega_m))\, e^{j\omega_m t} - (r_{c0} + ja_\delta\Delta(\omega-\omega_m))\, e^{-j\omega_m t}\right\}\Big] \quad \text{(B.3)}$$

From EqB.3, we can obtain the expression of the Intensity of this field.

$$\left|E_{ref}\right|^2 = E_0^2\Big[\Big(J_0 r_{c0} - 2J_1 a_\delta\Delta\omega\sin\omega_m t\Big)^2 + \Big\{J_0 a_\delta\Delta\omega + J_1(2rc0)\sin\omega_m t + 2\delta\Delta\omega_m\cos\omega_m t\Big\}^2\Big]. \quad \text{(B.4)}$$

After the demodulation, the remaining term is

$$4J_0J_1a_\delta^2\Delta\omega\Delta\omega_m = 16J_0J_1\frac{r_e^2t_f^4}{(1-r_fr_e)^4}\left(\frac{L}{c}\right)^2\Delta\omega\Delta\omega_m. \quad \text{(B.5)}$$

Bibliography

[1] A.Einstein:Sitzber.Deut.Akad.Wiss.Berlin,kl.Math.Physik u.Tech(1916)

[2] J.H.Taylor and J.M.Wenberg, Astrophys.J.345 (1989) 434

[3] A.Abramovici, W.E.Althouse, R.W.P.Drever, Y.Güsel, S.Kawamura, F.J.Raab, D.Showmaker, L.Siever, R.E.Spero, K.S.Thorne, R.E.Vogt, R.Weiss, S.E.Whitcomb and M.E.Zucker ,Science 256 (1992) 325.

[4] A.Brillet et al., VIRGO Final conceptual design (1992).

[5] K.Danzmann, H.Lück, A.Rüdiger, R.Schilling, M.Schrempel, W.Winkler, J.Hough, G.P.Newton, N.A.Robertson, H.Ward, A.M.Campbell, J.E.Logan, D.I.Robertson, K.A.Strain, J.R.J.Bennett, V.Kose, M.Kühne, B.F.Schutz, D.Nicholson, J.Shuttleworth, H.Welling, P.Aufmuth, R.Rinkleff, A.Tünnermann and B.Willke, Proposal for a 600m Laser-Interferometric Gravitational Wave Antenna, Max-Planck-Institut für Quantenoptik Report 190, Garching(Germany)(1994)

[6] K.Tsubono, 300-m Laser Interferometer Gravitational Wave Detector(TAMA300) in Japan, in:*Gravitational Wave Experiments* p.112-114,:eds:E.Coccia, G.Pizzella and F Ronga, World Scientific(1995)

[7] R.W.P.Drever, J.L.Hall, F.V.Kowalski, J.Hough, G.M.Ford, A.J.Muneley and H.Ward, Appl.Phys.B 32 (1983) 97

[8] B.J.Meers and K.A.Strain, Phys. Rev. D 43 (1991) 3117

[9] K.Tochikubo, A.Sasaki, K.Kawabe and K.Tsubono, "*Automatic alignment control for the TAMA interferometer*" in *Proceedings of the TAMA International Workshop on Gravitational Wave Detection* (Unversal Academy Press, Tokyo, 1997), pp. 365-367

[10] D.Z.Anderson, Appl. Opt. 23 (1984) 2944

[11] N.M.Sampas and D.Z.Anderson, Appl. Opt. 29 (1990) 394

[12] K.Kawabe, N.Mio and K. Tsubono Appl. Opt. 33 (1994) 5498

[13] E.Morrison, B.J.Meers, D.I.Robertson and H.Ward Appl.Opt.33 (1994) 5041

[14] E.Morrison, B.J.Meers, D.I.Robertson and H.Ward Appl.Opt.33 (1994) 5037

[15] B.F.Schutz, *A first course in general relativity,* (Cambridge University Press, 1985)

[16] C.W.Misner, K.S. Thorne, and J.A.Wheeler, *Gravitation*(Freeman, 1973)

[17] H.Kogelnik and T.Li Proc of The IEEE.54 (1966) 1312

[18] R.W.P.Drever, J.L.Hall, F.V.Kowalski, J.Hough, G.M.Ford, A.J.Muneley and H.Ward, Appl.Opt.23 (1983) 2944

[19] J.Weber, Physical Review 117 (1960) 306

[20] K.Tochikubo: Master Thesis (1996) *in Japanese*

[21] K.Kawabe: Doctor Thesis (1999)

[22] S.T.Yang, Y.Imai, M.Oka, N.Eguchi, and S.Kubota, Opt.Let. 21 (1996) 1676

[23] S.Nagano, M.Musha, L.Ying, N.Mio, and K.Ueda, Laser Physics 8 (1998) 686

[24] A.Araya: Doctor Thesis (1994)

[25] S.Telada: Doctor Thesis (1997)

[26] M.Ohashi: Doctor Thesis (1994) *in Japanese*

[27] M.Ando: Doctor Thesis (1999)

[28] S.Sato: Doctor Thesis (1999)

[29] K.Arai: Master Thesis (1997) *in Japanese*

[30] A.Takamori: Master Thesis (1998) *in Japanese*

[31] R.Takahashi, F.Kuwahara and K.Kuroda, " *VIBRATION ISOLATION STACK FOR TAMA300"* in *Proceedings of the TAMA International Workshop on Gravitational Wave Detection* (Unversal Academy Press, Tokyo, 1997), pp. 95-102

[32] F.Kuwahara: Master Thesis (1998) *in Japanese*

[33] S.Nagano:*to be published*

[34] M.Ando:*private comminucation*

[35] A. Araya, S. Telada, K. Tochikubo, S. Taniguchi, R. Takahashi, K.Kawabe, D. Tatsumi, T. Yamazaki, S. Kawamura, S. Miyoki, S. Moriwaki, M. Musha, S. Nagano, M.-K. Fujimoto, K. Horikoshi, N. Mio, Y. Naito, A. Takamori, and K. Yamamoto, Appl. Opt. 38 (13), 2848-2856 (1999)

[36] A.Ueda, N.Uehara, K.Uchisawa, K.Ueda, H.Sekiguchi, T.Mitake, K.Nakamura, N.Kitajima, and I.Kataoka, Opt.Rev.5,369-372(1996)

[37] S.Sato, S.Miyoki, M.Ohashi, M.-K.Fujimoto, T.Yamazaki, M.Fukushima, A.Ueda, K.Ueda, K.Watanabe, K.Nakamura, K.Etoh, N.Kitajima, K.Ito, and I.Kataoka, Appl.Opt.38,2880-2885(1999)

[38] S.Takemoto, H.Doi, and K.Hirahara J. Geod. Soc. Japan 31, 295-304 (1985).

[39] S.Taniguchi: Master Thesis (1999) *in Japanese*

[40] N.Mavalvala: Doctor Thesis (1997)